



NTNU – Trondheim
Norwegian University of
Science and Technology

Simulation of flow around a Viking ship rudder.

Thomas Heggem

Marine Technology

Submission date: June 2015

Supervisor: Håvard Holm, IMT

Norwegian University of Science and Technology
Department of Marine Technology



NTNU
Norwegian University of Science and Technology
Department of Marine Technology

MASTER THESIS IN MARINE HYDRODYNAMICS

SPRING 2015

FOR

Stud.techn. Thomas Heggem

SIMULERING AV STRØMNING OMKRING ET VIKINGSKIPSROR (Simulation of flow around a Viking ship rudder.)

The candidate shall perform simplified simulations of the fluid flow past a ship rudder.

The background for this assignment is vibrations experienced by a replica of the Oseberg Viking ship. It's unknown as to what is causing these vibrations and it is of interest if CFD can determine this.

OpenFOAM should be used in the numerical simulations. This implies that the candidate has to understand the program's functionality, possibilities and limitations. The decisions performed shall be documented. In the preliminary studies simple geometries shall be used to document the skill of the candidate and usage of the software.

In the thesis the candidate shall present his personal contribution to the resolution of the problem within the scope of the thesis work. Theories and conclusions should be based on mathematical derivation and logic reasoning identifying the various steps in the deduction. The original contribution of the candidate and material taken from other sources shall be clearly defined. Work from other sources shall be properly referenced. The candidate should utilize the existing possibilities for obtaining relevant literature.

The thesis should be organized in a rational manner to give a clear exposition of results, assessments and conclusions. The text should be brief and to the point, with a clear language.

The thesis shall contain the following elements: A text defining the scope, preface, list of contents, summary, main body of thesis, conclusions with recommendations for further work, list of symbols and acronyms, references and appendices. All figures, tables and equations shall be numerated.

It is supposed that Department of Marine Technology, NTNU, can use the results freely in its research work by referring to the student's thesis.

The thesis shall be submitted July 20, 2015, in two copies.

Håvard Holm
Associate professor/supervisor

Mobilis in Mobile

JULES VERNE

Preface

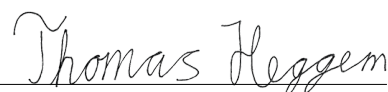
This master thesis mark the end of my five-year Master of echnology study in Marine Technology at the Norwegian University of Science and Technology (NTNU) in Trondheim.

I would like to thank several people who helped me during. I want to thank my advisor Associate Professor Håvard Holm for his valuable assistance and conversations throughout the semester.

I would like to thank NOTUR to providing NTNU, in in turn me, for their support and maintenance on the supercomputer Vilje. Without this resource at my disposal, this thesis would not be completed at this date.

Further thanks are addressed to Per Werenskiold and Jon Bojer Godal for providing me with this interesting topic, and Håkon Strandenes and Dr. Muk Chen Ong for conversations regarding OpenFOAM.

And lastly, and certainly not least, would I like to thank my friends and family, whose support during times of crisis and conversations when everything went smoothly proved invaluable to me.



Thomas Heggem
Trondheim, June 20, 2015

Abstract

Computational fluid dynamics (CFD) is a numerical method of solving the Navier-Stokes equations for all points in a grid, or mesh. By performing this operation over multiple time steps, the resulting velocity and pressure field can be found. This method has been used to simulate the flow past a Viking ship rudder at different flow regimes.

During sailing with a replica of the Oseberg ship, loss of steering power were experienced when the ship turned to starboard. The reason for this was determined to be the rudder shape. A thicker and longer rudder was made, with the intention to customise the rudder by gradually removing the extra thickness. The rudder had better steering, but not as good as when it turned to port. Moreover, it vibrated at certain angles of attack.

Several CFD analysis has been performed to examine what's causing the loss of lift and vibrations experienced by the rudder. A mesh of the fluid surrounding the rudder was generated using an in-house mesh generator developed at NTNU. The rudder was analysed from angles of attack $\alpha=-10$ to $\alpha=10$ degrees, with a 5 degree increase between simulations. A validation study of NACA0012 airfoil was performed as a part of the project thesis, and mesh convergence test were performed on the Oseberg rudder mesh. The angles were tested at rudder rake angles of 20,25 and 30 degrees, at Reynolds number 250, 1000 and 2.4×10^6 . The latter corresponds to a fully developed turbulent flow, as such the k- ϵ turbulence model was used. For the results the mean drag and lift coefficient, standard deviation and the resulting moments on the free surface was determined. The flow field was then examined through vorticity, characteristics of flow separation and pressure distribution on the surface of the rudder.

At $Re=1000/Re=2.4 \times 10^6$ and $\alpha=-10$ there was discovered a continuous vortex shedding on the port side of the rudder. These shed vortices gave rise to a oscillating lift force, and consequently vibrations on the rudder. It was discovered that increasing the rudder rake angle proved advantageous to avoid rapid oscillations of lift, stabilising the lift coefficient as β increased. The mean lift coefficient was higher at $\alpha=-10$ than at $\alpha=10$ degrees, indicating that the loss of lift is not caused by vortex shedding and flow separation.

A simplified model of ventilation were calculated to check the risk of air travelling along the rudder from the free surface due to suction pressure. At $\alpha=-10$ the lowest point where ventilation can occur increase nearly linearly with β , whereas for positive α it is fairly constant. This indicates that the lift for negative angles are generated more by suction pressure than for positive angles. This could cause the lift loss under real conditions.

To avoid vibrations, the rudder need to be more streamlined. Smoothing the leading edge will cause less flow separation, and increase stability. The rudder is slightly curved inwards at the port side. Making this side straight or with a slight outward curve will also make the rudder more stable against flow separation.

Sammendrag

Beregningsorientert fluidmekanikk (CFD) er en numerisk metode for å løse Navier-Stokes ligninger for alle punkter i et rutenett, eller mesh. Ved å utføre denne operasjon over flere tidssteg, kan den resulterende hastighets- og trykkfeltet bestemmes. Denne fremgangsmåten har blitt brukt for å simulere strømming forbi en vikingskipsror ved forskjellige strømningsregimer.

Under seiling med en kopi av Osebergskipet ble det registrert tap av løft når skipet la over til styrbord. Grunnen til dette ble bestemt til å være utformingen av roret. Et tykkere og lengre rør ble gjort, med den hensikt å tilpasse roret ved å gradvis fjerne den ekstra tykkelsen. Roret hadde bedre styring til styrbord, men ikke så bra som når det la over til babord. Dessuten vibrerte det på visse angrepsvinkler.

Flere CFD analyser har blitt utført for å undersøke hva som forårsaker tap av løft og at roret vibrerer. Et mesh av fluiden som omgir roret ble generert ved hjelp av en mesh generator utviklet ved NTNU. Roret ble analysert fra angrepsvinkelen $\alpha=-10$ til $\alpha=10$ grader, med en 5 graders økning mellom simuleringer. En valideringsstudie av NACA0012 airfoil ble utført som en del av foroppgaven, og en konvergens-test av meshet rundt Osebergroret ble utført. Vinklene ble testet ved 20,25 og 30 grader helning på roret, ved Reynolds tall 250, 1 000 og 2.4×10^6 . Sistnevnte svarer til en fullt utviklet turbulent strømming, dermed ble turbulensmodellen $k-\epsilon$ brukt. Dette ga resultater for gjennomsnittlig drag- og løftkoeffisient, standardavvik og de resulterende momenter på fri overflate. Strømningsfeltet ble deretter undersøkt med en studie av virvling, karakteristikker ved strømningsseparasjon og trykkfordeling på overflaten av roret.

Ved $Re=1000/Re=2.4 \times 10^6$ og $\alpha=-10$ ble det oppdaget en kontinuerlig virvelavløsning på babord side av roret. Disse ble periodisk avløst ut i væsken, noe som ga oscillerende løftekraft, og dermed vibrasjoner, på roret. Resultatene indikerte at ved å øke helningsvinkelen på roret, så ble virvelavløsningsfrekvensen lavere, som hentyder at løftkoeffisienten blir mer stabil når β øker. Gjennomsnittlig løftkoeffisient er høyere ved $\alpha=-10$ enn ved $\alpha=10$ grader, noe som indikerer at tapet av løft ved negative vinkler ikke er på grunn av virvelavløsning eller separasjon av strømming om roret.

En forenklet modell av ventilasjon ble beregnet til å antyde risikoen for at luft beveger seg ned langs roret fra fri overflaten på grunn av sugetrykk. Ved $\alpha=-10$ øker det laveste punktet hvor ventilasjonen kan oppstå nesten lineært med β , mens for positiv α det er mer konstant. Dette indikerer at løftet for negative vinkler genereres mer av sugetrykk enn for positive vinkler. Dette kan være grunnen til tapet av løft som ble erfart i praksis.

For å unngå vibrasjoner, må roret gjøres mer strømlinjeformet. Utjevning av ledende kant vil føre til mindre strømningsseparasjon, og øke stabiliteten til løftet. Roret er kurvet litt innover på babord side. Å gjøre dette siden rett, eller med en liten kurvatur utover vil også gjøre roret mer resistant mot separasjon.

Contents

1	Introduction	1
1.1	Motivation and objective	2
1.2	Outline of the thesis	3
2	Theory	7
2.1	Foil terminology	7
2.2	Navier-Stokes equations	8
2.2.1	Conservation of mass	8
2.2.2	Conservation of momentum	8
2.2.3	Conservation of energy	8
2.2.4	Incompressible, isothermal flow	9
2.3	Scaling of results	9
2.4	Vortex shedding	10
2.4.1	Strouhal number	11
2.5	Forces and moments	11
2.5.1	Forces acting on a body in a fluid	11
2.5.2	Force coefficients	12
2.5.3	Moments	12
2.5.4	Moment coefficients	13
2.6	Vorticity	13
2.7	Free surface	13
2.7.1	Ventilation	14
3	CFD	15
3.1	Turbulence simulation	15
3.1.1	DNS	16
3.1.2	LES	16
3.1.3	RANS	17
3.1.4	DES	18
3.2	k- ϵ turbulence model	18
3.2.1	Law of the wall	19
3.3	Courant number	21
3.4	OpenFOAM	22
3.5	Mesh	24
3.6	Vilje	25

4	Model	27
4.1	NACA0012 airfoil	27
4.2	Oseberg-rudder	30
4.2.1	k- ϵ boundary conditions	34
5	Results	37
5.1	NACA0012 airfoil	37
5.2	Oseberg rudder	39
5.2.1	Pressure forces	42
5.2.2	Viscous forces	44
5.2.3	Total forces experienced by the rudder	45
5.2.4	Total moments experienced by the rudder	47
5.2.5	Turbulent results	49
6	Discussion	51
6.1	Validation of the NACA0012 airfoil results	51
6.2	Effect of unsymmetrical rudder design	53
6.3	Vorticity	54
6.4	Vortex shedding	56
6.5	Pressure distribution	64
6.6	Ventilation	67
6.7	Suggested improvements	68
6.8	Limitations of the model	69
6.8.1	Issues encountered during this thesis	70
7	Conclusion	75
8	Recommendations for further work	77
	Bibliography	79
	Appendix 1: Oseberg rudder pressure contours	I
	Appendix 2: Oseberg rudder velocity fields	XI
	Appendix 3: Oseberg rudder turbulent time series	XXIII
	Appendix 4: Vorticity for $Re=1000$ and $Re=Re=2.4 \times 10^6$	XXV
	Appendix 5: OpenFOAM control files	XXVII

List of Figures

1.1	Different Viking ships	1
1.2	Keel carvings on the Oseberg ship	2
1.3	Draving of the modified Oseberg rudder	5
2.1	Definitions of foil terminology	7
2.2	The shear layer and vorticity generated by flow separation	10
2.3	Criterion for flow separation.	10
3.1	Turbulence methods and accuracy	16
3.2	Spalding’s inner law expression compared with expermental data of a smooth pipe [White and Corfield, 1991].	20
3.3	Velocity distribution for smooth smooth pipe near pipe wall [Schlichting, 1979].	21
3.4	Structure of OpenFOAM	22
3.5	Structured single-block, multi-block and unstructured mesh.	25
4.1	NACA0012 airfoil mesh boundary condition and set-up.	28
4.2	Overview of the NACA0012 mesh	28
4.3	Cells near the leading edge of the NACA0012 foil.	28
4.4	Definition of forces and moments.	30
4.5	Oseberg rudder orientation and angle definitions.	30
4.6	Domain configuration of the Oseberg rudder	31
4.7	The blocks surrounding a foil section of the Oseberg rudder	32
4.8	Oseberg mesh overview	32
4.9	Detailed view of the Oseberg mesh.	33
4.10	Inflow with an angle of attack	34
5.1	Convergence of instantaneous lift and drag coefficient	40
5.2	Mesh convergence of drag and lift coefficient for $\alpha=0, \beta=25$	40
5.3	Mesh convergence of drag and lift coefficient for $\alpha=0, \beta=25$	41
5.4	Pressure forces for Re= 250	43
5.5	Pressure forces for Re= 250	43
5.6	Pressure forces for Re= 1000	44
5.7	Viscous forces for Re= 250	44
5.8	Viscous forces for Re= 1000	45
5.9	Total forces in x-direction	46
5.10	Total forces in y-direction	46
5.11	Total forces in z-direction	47

5.12	Roll moment	47
5.13	Pitch moment	48
5.14	Yaw moment	49
6.1	Vorticity at leading and trailing edge at $\beta=20$, $Re=1000$ and $ z/d =0.6$. .	55
6.2	Vorticity around the rudder and into the wake	56
6.3	Streamlines at $Re= 1000$, $\beta= 25$ degrees and angle of attack $\alpha= -10$ degrees.	58
6.4	Velocity field for $\alpha=\pm 10$ at $Re=2.4\times 10^6$, $\beta=20$	59
6.5	Cross-sections at $ z/H = 0.8$ for the three rake angles.	60
6.6	Figure is continued on next page.	61
6.7	Streamlines at $Re=1000$, $\alpha= -10$ deg., $\beta= 20$ and 30 degr.	62
6.8	Q-criterion for $Re=1000$, $\alpha=-10$	63
6.9	Q-criterion for $Re=1000$, $\alpha=10$	63
6.10	Q-criterion for $Re=2.4\times 10^6$, $\alpha=-10$	63
6.11	Q-criterion for $Re=2.4\times 10^6$, $\alpha=10$	63
6.12	Pressure contours on rudder surface for $Re=1000$, $\beta= 20$	65
6.13	Pressure contours on rudder surface for $Re=1000$, $\beta= 25$	65
6.14	Pressure contours on rudder surface for $Re=1000$, $\beta= 30$	66
6.15	Pressure contours on rudder surface for $Re=2.4\times 10^6$, $\alpha= 10$	67
6.16	Pressure contours on rudder surface for $Re=2.4\times 10^6$, $\alpha= -10$	67
6.17	Risk of ventilation at $Re=2.4\times 10^6$	68
6.18	Plot over residuals until critical instability	71
6.19	NACA0012 airfoil with different solution schemes	72
6.20	Cross-sections and thickness of the rudder	74

List of Tables

4.1	Boundary and initial conditions in OpemFOAM for NACA0012 airfoil . .	28
4.2	Test conditionsfor the NACA0012 airfoil	29
4.3	Values for rudder rake and angle of attack	30
4.4	Boundary and initial conditions for the Oseberg rudder	33
4.5	Fluid properties for the Oseberg rudder	34
4.6	Initial and boundary conditions for the k- ϵ turbulence model.	36
5.1	NACA0012 results at different Reynolds numbers	38
5.2	Mesh convergence of hydrodynamic lift and drag coefficient for the Oseberg rudder	39
5.3	Mesh convergence of hydrodynamic lift and drag for the Oseberg rudder	41
5.4	Pressure and viscous force coefficients at $Re=2.4 \times 10^6$	49
5.5	Total force and moment coefficients at $Re=2.4 \times 10^6$	50
6.1	Comparison of results for the NACA0012 airfoil.	51
6.2	Mean drag coefficient at different Reynolds numbers.	53
6.3	Mean lift coefficient at different Reynolds numbers.	54
6.4	Strouhal number and standard deviations for the Oseberg rudder	59

Acronyms

2D	Two dimensional
3D	Three dimensional
CFD	Computational fluid dynamics
DES	Detached eddy simulation
DNS	Direct numerical simulation
LES	Large eddy simulation
PISO	Pressure implicit with splitting of operators
RANS	Reynolds-averaged Navier-Stokes
RAS	Reynolds-averaged simulation
SD	Standard deviation
STL	StereoLitography, a file format
URANS	Unsteady Reynolds-averaged Navier-Stokes

Nomenclature

α	Rudder angle of attack
Asp	Aspect ratio
β	Rudder rake angle
d	Rudder draft
Δt	Change in time/timestep
Δx_i	Cell length
δ	Boundary layer thickness
δ_{ij}	Kronecker delta
ϵ	Rate of turbulent kinetic energy dissipation
κ	von Karmans constant
μ	Dynamic viscosity of fluid
ν	Kinematic viscosity of fluid
ν_t	Turbulent viscosity of fluid
ω	Instantaneous vorticity
ρ	Fluid density
σ_k	Turbulent Prandtl number for kinetic energy
σ_ϵ	Turbulent Prandtl number for dissipation
τ_{ij}	Stress tensor
τ_w	Wall shear stress
c	cord length
C_1	Constant in the ϵ model equation
C_2	Constant in the ϵ model equation
C_D	Mean drag coefficient
C_{DP}	Mean pressure drag coefficient
C_{DSD}	Standard deviation for the drag coefficient
C_{DV}	Mean viscous drag coefficient
C_L	Mean lift coefficient
C_{LP}	Mean pressure lift coefficient
C_{LSD}	Standard deviation for the lift coefficient
C_{LV}	Mean viscous lift coefficient

Co	Courant number
Co_{Max}	Maximum Courant number
C_{M_x}	Roll moment coefficient
C_{M_y}	Pitch moment coefficient
C_{M_z}	Yaw moment coefficient
C_μ	Turbulent viscosity constant in the k- ϵ turbulence model
C_P	Average pressure coefficient
E	Log-law constant
L/D	Turbulent scale factor
F_D	Instantaneous drag force
\overline{F}_D	Mean drag force
F_L	Instantaneous lift force
\overline{F}_L	Mean lift force
f_v	Vortex shedding frequency
g	gravitational constant
h_p	Normal distance between the wall and first cell
I_u	Turbulence intensity
k	Turbulent kinetic energy
p	Total pressure
P	Mean pressure
p'	Fluctuating pressure
P_0	Hydrostatic pressure
P_a	Atmospheric pressure
Re	Reynolds number
S	Wetted surface area
s	Rudder span
St	Strouhal number
t	time
u_i	Cartesian component of the velocity vector
U_i	Cartesian component of the mean velocity vector
u'_i	Cartesian component of the fluctuating velocity vector
U_∞	Incident velocity
u^+	Dimensionless velocity
u_τ	Friction velocity
$\overline{u'_i u'_j}$	Reynold stress component
x_i	Cartesian coordinates
y^+	Dimesnionless distance from the wall

Chapter 1

Introduction

Norway has always had a strong cultural background in the maritime environment. The sea has been the backbone of this regions economy and survival, from fishing for food to exporting timber overseas. The country is also divided by fjords and mountains, resulting in strong boat- and ship-building traditions. This trait became apparent during the late eight century to the eleventh century, when the Vikings were a dominant force in Northern Europe. Central for all the Scandinavian nations were the Viking ships, whether it was a longship built for raiding, a knarr for commerce and transportation or a pleasure craft for travelling in the fjords.

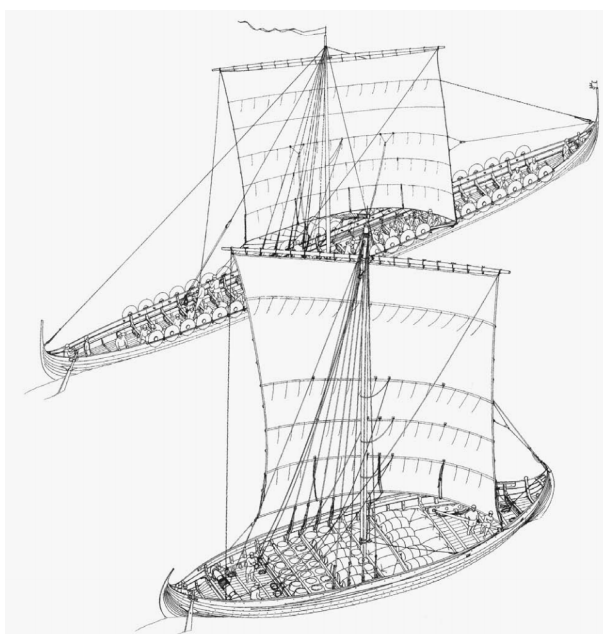


Figure 1.1: Hedeby 1 and Hedeby 3 are examples of a Viking longship and knarr, respectively [Bogucki and Crabtree, 2004].

1.1 Motivation and objective

The Oseberg ship has traditionally been placed in the latter category, or even as a vessel build purely for burial. The remains of two women were found in the centre of ship at the excavation site, suggesting that these were high-ranking individuals [Kulturhistorisk museum, 2015]. The ship was fairly wide, with a length to beam ratio of 4.3. When compared to the Gokstad ship, it is also less robustly built and has a shallower draft, suggesting that it was meant for primary fjord and coastal use. The ship itself was beautifully carved along the keel and other central areas.



Figure 1.2: Keel carvings found on the Oseberg ship. Note the remains of the rudder are still attached to the vessel. From Oseberg ship excavation site, photographer unknown.

The discussion regarding the seaworthiness of the Oseberg ship has been ongoing since 1987, when a replica of the ship, *Dronningen*, capsized and sank on her maiden voyage [Teknisk Ukeblad, 2011]. A theory is that the ship was used purely for burial, but signs of wear on the rowlocks indicate otherwise. The original reconstruction of the vessel was therefore studied further, to see if it were accurately assembled. The study of the ship started in April 2005. In this process a 3D drawing of the ship were generated, and some possible errors due to the reconstruction process was corrected in the digital drawings. As a consequence of this discovery, a model of the original Oseberg ship and the modified one were tested at MARINTEK in 2008. The towing tank test performed revealed generally

favourable result for the modified hull shape [Price et al, 2008].

The building of the replica started in July, 2010. Traditional building methods and tools were being used for the entire process, as far as it were practically possible. The keel was laid down in January 2011, and the ship were launched on 20. of June, 2012 [Gåten Oseberg, 2015].

During sailing the original rudder was deemed unusable. This could be due to several reasons, such as inaccurate reconstruction, the current rudder were unsuitable for the sailing conditions or the rudder itself were originally unstable. The latter is unlikely, but might be true nevertheless. Regardless of the cause, a new rudder were made and attached to the Viking ship. This rudder were principally similar to the original, but thicker as this could be trimmed away later on. The rudder proved more usable, steering slightly better to port than starboard. Steering to starboard while under sail proved difficult [Godal, 2014]. The most likely cause of this was determined to be a turbulent flow from the keel or bow of the vessel. A solution was therefore to extend the rudder draft by 25 cm. This made it easier to turn to starboard, but not as effective as when the rudder were turned to port. Due to the larger thickness of the profiles, it was experienced that the rudder had large resistance in the water. Furthermore, the rudder vibrated during sailing. Figure 1.3 is an illustration of the initial rudder design. This is the design that have been used in this thesis to examine the flow field around the rudder.

1.2 Outline of the thesis

Chapter 2 gives a relatively brief description of foil terminology, mathematical equations used in CFD, forces and moments affecting a body in a fluid and physical phenomena that might occur with a fluid flow past an object.

Chapter 3 outlines the different simulations used in CFD, how turbulence are modelled in this thesis, defining characteristics of creating and running a simulation in OpenFOAM, mesh generation and the computational resources used for the simulation.

Chapter 4 defines the fluid domain, the mesh configuration, boundary conditions and initial conditions defined for the model.

Chapter 5 presents and briefly discuss the forces acting on a NACA0012 airfoil and

the Oseberg rudder under the different flow regimes. For the rudder the total mean lift and drag are presented, as well as the drag and lift coefficient due to viscous and pressure forces are portrayed. The resulting moments about a point on the rudder at the free surface have been presented and discussed.

Chapter 6 discuss the effect generated by the rudder in the fluid. An validation study of NACA0012 in a laminar flow are presented. Vorticity comparisons, flow separation and vortex shedding are discussed for the Oseberg rudder. The pressure distribution and the risk of ventilation on the rudder surface have been presented and explained. An recommendation regarding general rudder design are given, and problems encountered in this thesis are presented.

Chapter 7 gives a final conclusion regarding the work performed in this thesis.

Chapter 8 outlines recommendations for further work.

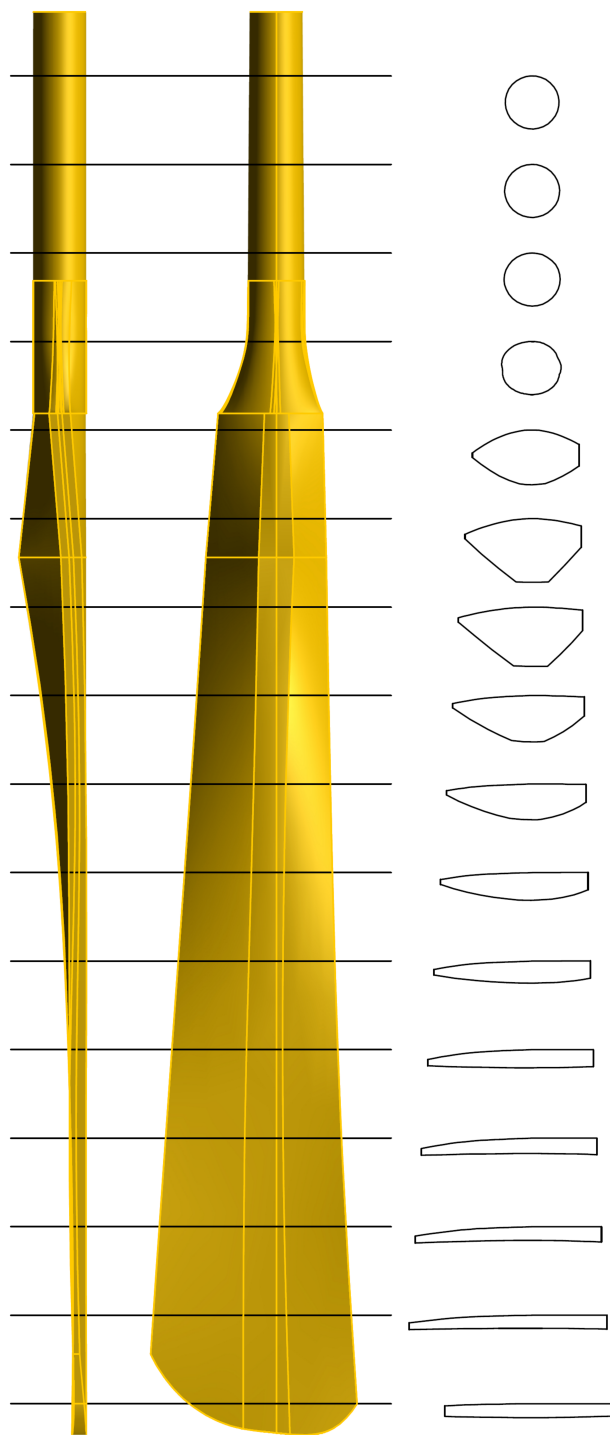


Figure 1.3: The modified Oseberg rudder, with cross-sections.

Chapter 2

Theory

This section describes foil terminology, the governing equations used when performing a computational fluid dynamics (CFD) simulation, and forces exerted on a body in a fluid. The equations are well established within the field of hydrodynamics, and are presented here to explain the physics underlying a CFD simulation.

2.1 Foil terminology

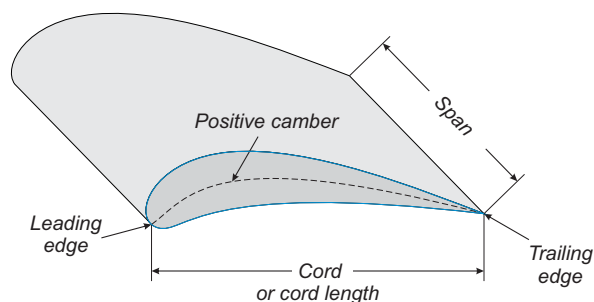


Figure 2.1: Definitions of foil terminology

There are certain terms and definitions used when describing foils. Figure 2.1 illustrates the most essential ones. The cord length is the distance from the leading edge to the trailing edge, without taking curvature into account. When the foil has a mean thickness line that is not the cord line, the foil has camber. In the illustration the camber is positive. The foil would have a negative camber if it was curved downwards instead. An additional term associated with foils is the aspect ratio Asp . For a rectangular foil, e.g the span is constant, the aspect ratio is defined as $Asp = \frac{s}{c}$.

2.2 Navier-Stokes equations

The equations themselves are quite complex and some can only be solved through numerical calculation. The standardised equations are the conservation of mass, momentum and energy for a fluid element.

2.2.1 Conservation of mass

The equation is derived from the physical condition that the change of fluid element mass has to be equal to the net outflow of the element surface. By re-arranging this requirement on the left-hand side the equation of mass conservation is obtained:

$$\frac{\partial \rho}{\partial t} + \nabla(\rho u_i) = 0 \quad (2.2.1)$$

For a three-dimensional case, $i=1,2,3$.

2.2.2 Conservation of momentum

The equations is derived from Newton's 2nd law of motion. The mass acceleration has to be equal to the surface force and the body force.

$$\rho \frac{Du_i}{Dt} = -\frac{\partial p}{\partial x_i} + \frac{\partial}{\partial x_i} \left[\mu \left(\frac{\partial u_i}{\partial x_j} + \frac{\partial u_j}{\partial x_i} - \frac{2}{3} \delta_{ij} \frac{\partial u_k}{\partial x_k} \right) + \mu_B \delta_{ij} \frac{\partial u_k}{\partial x_k} \right] + \rho f_i \quad (2.2.2)$$

where μ_B is the bulk viscosity and δ_{ij} is the Kronecker delta.

2.2.3 Conservation of energy

The total change in energy has to be equal to the change of heat supply and change in work excited by forces on the fluid element. This condition is represented in the following equation:

$$\rho \frac{De_i}{Dt} + \frac{Dp}{Dt} = \frac{\partial}{\partial x_i} \left[\mu \left(\frac{\partial u_i}{\partial x_j} + \frac{\partial u_j}{\partial x_i} - \frac{2}{3} \delta_{ij} \frac{\partial u_k}{\partial x_k} \right) + \mu_B \delta_{ij} \frac{\partial u_k}{\partial x_k} \right] \frac{\partial u_i}{\partial x_j} - \frac{\partial q_j}{\partial x_j} \quad (2.2.3)$$

2.2.4 Incompressible, isothermal flow

For an incompressible, isothermal (no variations in temperature) flow all the variables in equation 2.2.1 to 2.2.3 is not included. For an incompressible flow the variations in density and bulk viscosity(μ_B is coupled to density variations) is zero.

By neglecting external forces, such as gravity, and setting the system to be an isothermal process, equation 2.2.1 and 2.2.2 reduces to:

$$\frac{\partial u_i}{\partial x_i} = 0 \quad (2.2.4)$$

$$\rho \frac{Du_i}{Dt} = -\frac{\partial p}{\partial x_i} + \mu \frac{\partial^2 u_i}{\partial x_i \partial x_j} \quad (2.2.5)$$

Equation 2.2.3 will disappear entirely, due to no heat exchange.

2.3 Scaling of results

It is important to present results so that they can be compared to other sources, or be scaled from model scale to full-scale. There are two common to do this, by similarity in viscous effects or similarity in gravitational effects. In this thesis flow regime has been scaled using similarity in viscous effects. Consequently, the results have to be presented in a non-dimensional form.

Reynolds number defines the flow characteristics non-dimensionally by describing the ratio of inertia forces to viscous forces. A low Reynolds number indicates laminar flow, whereas a large Reynolds number mean turbulent flow. Between these two regimes we will have a transitional phase. Most flows in the natural world and practical applications are turbulent. At these Reynolds number the flow behave in a disorderly fashion and the effects generated by the flow will not be stationary in most cases. As such, it is hard to predict the effects caused by turbulence, and in most cases the average effects will be monitored instead.

$$Re = \frac{U_\infty L}{\nu} \quad (2.3.1)$$

where ν is the dynamic viscosity, U is the inflow velocity and L is the characteristic length of the geometry studied. In this thesis the cord length will be used for the NACA0012

airfoi, and the mean cord length for the Oseberg rudder.

Another dimensionless number for flow regimes is the Froude number. It is the ratio of inertia flow to gravitational field. It's main application in naval hydrodynamics is to compare the wave resistance and wave pattern generated by a body moving through a fluid.

$$Fn = \frac{U_\infty}{\sqrt{gL}} \quad (2.3.2)$$

where l is a characteristic length.

Since the free surface is not modelled in this thesis, this number is not applicable. As both the rudder and airfoil are slender through the fluid surface, resistance due to wave generation will be minimal. Neglecting these effects will not affect the solution significantly.

2.4 Vortex shedding

Flow separation occurs when the adverse pressure gradient, $\partial p/\partial x$, is positive. This happens due to conditions imposed on the fluid by the presence of a body. When the flow separates, there will be a backflow due to the no-slip condition on the body. The resulting interaction between the backflow and incoming flow creates a shear layer. In this layer there will be vorticity, causing the shear layer to roll up into a vortex. For a cylinder there will be a vortex formation on both sides of the geometry. The pair of vortices will be shed periodically, as one vortex will be pulled across the wake and cut off the other. This cause another vortex to grow and eventually be shed on the opposite side, and cut off the other vortex. As a result of this process there will be forces acting periodically on the cylinder.

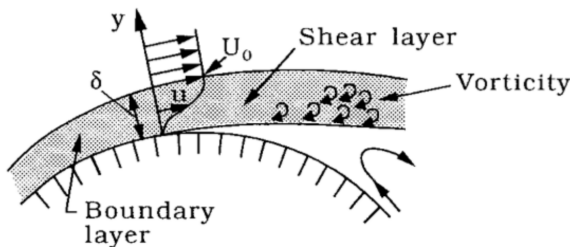


Figure 2.2: The shear layer and vorticity generated by flow separation [Sumer and Fredsoe, 2006].

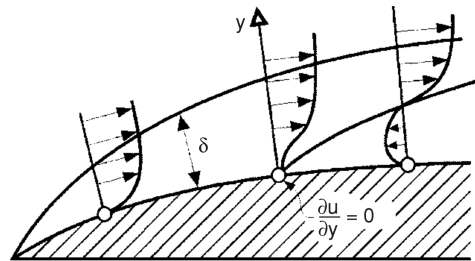


Figure 2.3: Criterion for flow separation downstream from a point [Walderhaug, 1972].

If there exist a point P where $\partial u/\partial y=0$ and there is a backflow downstream from the point, then the flow will separate at point P. If $\partial u/\partial y$ downstream from P continues to be zero, the flow will not separate [Walderhaug, 1972]. It follows from this criterion that flow separation can be prevented by designing surface curvatures correctly.

2.4.1 Strouhal number

The vortex shedding frequency is often presented as the Strouhal number. It is defined as

$$St = \frac{f_v L}{U_\infty} \quad (2.4.1)$$

where f_v is the vortex shedding frequency in Hz and L is a characteristic length. For the Oseberg rudder the mean cord length c is being used.

2.5 Forces and moments

2.5.1 Forces acting on a body in a fluid

Whenever an object is placed in a fluid, the fluid will exert forces on the surface of said object. The two main contributors to this force is friction and pressure. The pressure force is found by integrating the resulting pressure over the surface of the body. The viscous force are the force acting on the body due to shear stress. These stresses appear due to the variation in fluid velocity on the surface of the body and outside in the boundary layer. The mathematical expressions for the shear stress are $\tau_v = \frac{\partial u}{\partial y}$. The viscous force are then the shear stress multiplied with the area.

For an axi-symmetrical body the sum of these forces is the drag force; acting in the streamwise direction. If the object of interest is not symmetric or has a varying or antisymmetric pressure distribution, it will generate a lift force. This force is acting in the crosstream direction. For many objects the flow will induce a varying force on the cylinder, for instance due to vortex shedding. An usual procedure is to present the forces as mean viscous force and pressure force, represented by \overline{F}_v and \overline{F}_p respectively.

The total in-line force acting on the airfoil or rudder will be the sum of the mean pressure force and viscous force, and are the total drag force.

$$\overline{F}_D = \overline{F}_v + \overline{F}_p \quad (2.5.1)$$

The same applies to the mean cross-flow force or lift force.

$$\overline{F}_L = \overline{F}_v + \overline{F}_p \quad (2.5.2)$$

For stream-lined bodies the lift and drag force will stabilise on a fixed value instead of fluctuating.

If the body of interest experiences vortex shedding, the forces will fluctuate about an mean value. The mean magnitude of these oscillations are found by taking the standard deviation of the forces.

$$SD = \sqrt{\frac{1}{N} \sum_{i=1}^N (x_i - \bar{x})^2} \quad (2.5.3)$$

For the standard deviation of the lift and drag coefficients, x_i is the instantaneous value, whereas \bar{x} is the mean value. N is the total number of data points where the lift and drag have stabilised.

2.5.2 Force coefficients

Force coefficients are used to present data dimensionless for comparison and scaling purposes.

$$C_D = \frac{\overline{F}_D}{\frac{1}{2}\rho U_\infty^2 A} \quad (2.5.4)$$

$$C_L = \frac{\overline{F}_L}{\frac{1}{2}\rho U_\infty^2 A} \quad (2.5.5)$$

where A is the area the flow "sees" when encountering the body of interest. For a foil A is the cord length times the span, per definition. For the Oseberg rudder the wetted surface are being used, due to the highly varying cord line.

2.5.3 Moments

The moments can be calculated from the forces by the standard definition:

$$\vec{M} = \vec{F} \times \vec{r} \quad (2.5.6)$$

where r is the distance from the resultant force acting on the body and the moment point

of origin. Equation 2.5.6 can be expressed on component form:

$$M_x = F_z * r_y - F_y * r_z \quad (2.5.7)$$

$$M_y = -F_z * r_x + F_x * r_z \quad (2.5.8)$$

$$M_z = F_y * r_x - F_x * r_y \quad (2.5.9)$$

The resulting matrix from equation 2.5.6 is singular, meaning that there exist an infinite number of solutions for \vec{r} as long as no outer constraint are applicable.

2.5.4 Moment coefficients

The moments can be expressed as coefficients, for comparison or scaling purposes. A characteristic length has been used to obtain a dimensionless variable. For a foil or rudder the span s is used for the moment about the x- and z-axis, and the cord length c for the moment about the y-axis.

$$C_{M_x} = \frac{\overline{M}_x}{\frac{1}{2}\rho U_\infty^2 A s} \quad (2.5.10)$$

$$C_{M_y} = \frac{\overline{M}_y}{\frac{1}{2}\rho U_\infty^2 A c} \quad (2.5.11)$$

$$C_{M_z} = \frac{\overline{M}_z}{\frac{1}{2}\rho U_\infty^2 A s} \quad (2.5.12)$$

2.6 Vorticity

The vorticity is a measurement of how much the fluid particle is spinning at a given position. Vorticity is therefore a good unit of measurement for vortex formations in three dimensions.

$$\omega = \nabla \times u_i \quad (2.6.1)$$

2.7 Free surface

A body moving in a fluid close to, or through the free surface, will experience several effects. The most distinct one are the generation of surface waves. If there is a relative

speed between the body of interest and the fluid, then the body will displace the fluid elements it encounters. The fluid in front of the element will de-accelerate, giving rise to a positive pressure. This pressure will result in an elevated surface in front of the body. For non-streamlined shapes, there will be a negative pressure behind the body, and consequently a surface depression. The pressure and surface deformation will in turn transfer to gravity waves. A slender body will generate less waves and therefore experience less wave-making resistance than a bluff body.

In real-life conditions there will also exist incident surface waves. The result of the wave-body interaction will be a dynamic pressure due to surface wave elevation.

Another consequence of the free surface are ventilation.

2.7.1 Ventilation

If the dynamic pressure and the static pressure on the surface of the foil is lower than the atmospheric pressure, a body immersed in a fluid will risk ventilation. This is a phenomenon where air from the free surface can find its way down along the geometry to an area with low enough pressure. As a consequence, lift generated by the body will decrease. The basic criteria for avoiding ventilation is that the total pressure on the surface of the body is larger than the atmospheric pressure.

$$P_0 + \rho gh > P_a \quad (2.7.1)$$

The pressure coefficient is defined as

$$C_P = \frac{\overline{P_0} - P_a}{\frac{1}{2}\rho U_\infty^2} \quad (2.7.2)$$

Subtracting the atmospheric pressure from equation 2.7.1 and inserting the pressure coefficient gives a modified criteria for ventilation. Dividing with common terms leads to equation 2.7.3.

$$\frac{1}{2}U_\infty^2 C_P + \rho g > 0 \quad (2.7.3)$$

By using the pressure coefficient the results from a CFD analysis can be used to check the risk of ventilation in a real scenario. U_∞ will then be the velocity of the full-scale vessel or object.

Chapter 3

CFD

Computational fluid dynamics is a numerical method of solving the Navier-Stokes equations by solving it for every fluid particle in the domain. The object of interest is surrounded by a mesh that are divided into small volumes, cells. For each of these cells the discretized versions of equations 2.2.1 2.2.2 and 2.2.3 are being solved for each time step, based on initial conditions. If all the terms in the above mentioned equations were to be moved to the left hand side, the solution should ideally be zero. For a numerical method this value will not be zero, but will be gradually decrease. As these residuals approach zero, the solution will start to converge. This can take several thousands of iterations or time steps.

3.1 Turbulence simulation

Mostly all flows that occur in nature and practical applications are turbulent. The main characteristic of a turbulent flow is that it varies randomly both in position and time, in all three dimensions. This makes turbulent flow a distinctly three dimensional phenomenon, and has to be modelled accordingly. Another aspect of turbulent flow is that the fluid will appear more viscous. Fluid mixing and transportation will also increase due to a higher degree of vorticity in turbulent flow compared to laminar flow.

To simulate turbulent flow in a laboratory will in many cases require a high Reynolds number that is difficult to achieve. CFD can therefore be a great asset in performing these experiments numerically. There are several methods and formulations as to predict turbulent flow, all with different degree of accuracy and usability. A brief overview of the different methods will be given, from high to descending degree of accuracy.

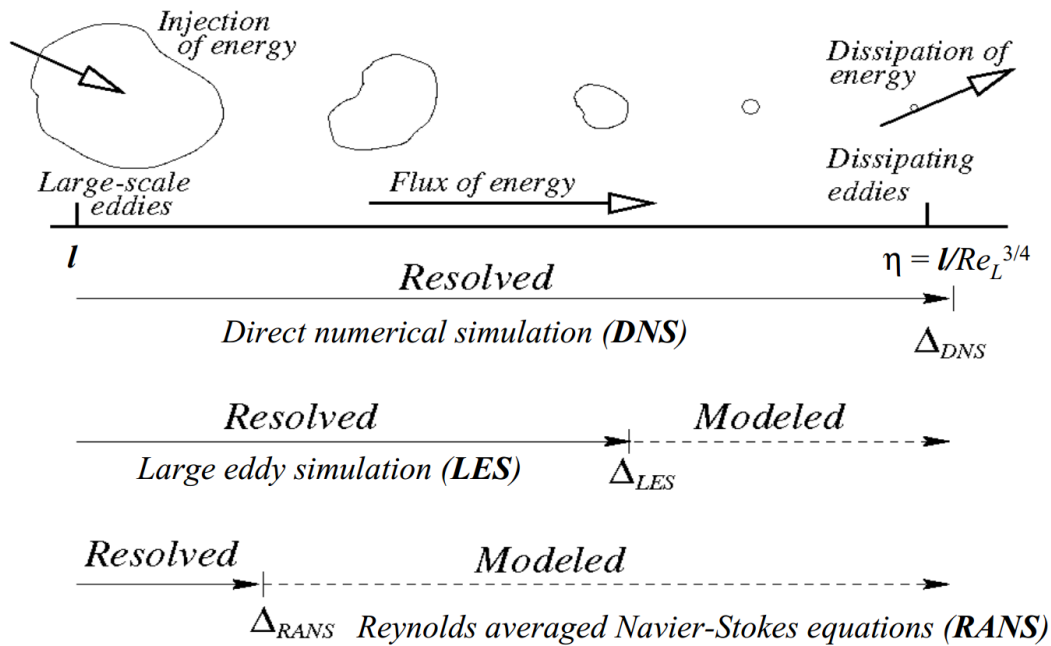


Figure 3.1: Overview of the simulation accuracy in relation to motion scales. From [Bakker, 2006], with permission.

3.1.1 DNS

Direct numerical simulation (DNS) solves the unsteady Navier-Stokes equation without any simplifications or approximations. The equations listed under section 2.2 will be solved for every fluid element for all time steps. As indicated in figure 3.1, this method will correctly model all eddy sizes, to the smallest eddies that dissipates into the fluid. It will therefore accurately describe the flow field, but at a high computational cost. Even at low Reynolds numbers it will be computational intensive, due to solving the Navier-Stokes equations exactly.

3.1.2 LES

Large eddy simulation (LES) solves the full unsteady Navier-Stokes equations for large eddies. The lower motion scales are approximated by a turbulence model. LES is three-dimensional and time dependent, and therefore computational intensive. It requires less resources than DNS.

3.1.3 RANS

Reynolds-averaged Navier-Stokes equations are the Navier-Stokes equations averaged over time. The fluctuation components will be averaged out, and the solution will be the mean velocity field. The time averaging will introduce new terms based on the turbulent fluctuations. The consequence is that the unknowns will outnumber the equations. Thus, additional equations are required. These are added based on the enhanced stirring caused by the turbulent flow. The computational cost is greatly reduced due to the simplification and time-averaging of the flow field.

The velocity and pressure terms is assumed to consist of a mean term and a fluctuating term:

$$\begin{aligned}u_i &= U_i + u'_i \\ p &= P + p'\end{aligned}$$

where the capital letter denotes the mean value. Inserted into equations from section 2.2.4:

$$\frac{\partial u_i}{\partial x_i} = 0 \quad (3.1.1)$$

$$\rho \frac{DU_i}{Dt} = -\frac{\partial P}{\partial x_i} + \mu \frac{\partial^2 U_i}{\partial x_i \partial x_j} - \frac{\partial \overline{u'_i u'_j}}{\partial x_j} \quad (3.1.2)$$

$\overline{u'_i u'_j}$ is the the Reynolds stress component. It can be expressed as

$$-\partial \overline{u'_i u'_j} = \nu_T \left(\frac{\partial U_i}{\partial x_j} + \frac{\partial U_j}{\partial x_i} \right) - \frac{2}{3} k \delta_{ij} \quad (3.1.3)$$

where k is the turbulent kinematic energy and ν_T is the turbulent kinematic eddy viscosity.

Unsteady Reynolds-averaged Navier-Stokes (URANS) is a method where the average velocity field is chosen as unsteady, e.g. not constant in time.

3.1.4 DES

Detached eddy simulation is a hybrid method combining characteristics from both RANS and LES. It has the characteristics of RANS near solid boundaries, and LES after drastic flow separation. As a consequence this method will use a turbulence model near walls, avoiding high grid resolution in these areas. LES in the flow separation zones will ensure that the smaller eddies will be correctly modelled. This method will be less computational intensive than LES as a result.

3.2 k- ϵ turbulence model

There are several turbulence models that approximate the fluid flow behaviour in turbulence, such as k- ϵ , k- ω and Spalart-Allmaras. They offer additional equations to solve the Reynolds stresses and additional components, depending on the turbulence model. The advantage of these models are that the fluid-wall interactions will be treated well without the need for a very high grid resolution close to the wall. They have different characteristics to predict a certain kind of fluid flow. It is therefore important to chose a model that corresponds to the physical case in the simulation, as the models have disadvantages as well.

The k- ϵ model is the most widely used turbulent model. The limitations and advantages is therefore well documented. The most critical limitation of this model is that it poorly predicts areas where massive flow separation occurs.

k- ϵ is a two equation model, solving two equations to find k and ϵ . k is the turbulent kinematic energy associated with eddies in the flow, whereas ϵ is the rate of turbulent kinetic energy dissipation. These two variables are used to find the Reynolds stresses, and as such determine the eddy viscosity.

The equations for k and ϵ is presented below, respectively:

$$\frac{\partial k}{\partial t} + \frac{\partial k U_j}{\partial x_j} = \frac{\partial}{\partial x_j} \left(\frac{\nu_T}{\sigma_k} \frac{\partial k}{\partial x_j} \right) + \nu_T \frac{\partial U_i}{\partial x_j} \left(\frac{\partial U_i}{\partial x_j} + \frac{\partial U_j}{\partial x_i} \right) - \epsilon \quad (3.2.1)$$

$$\frac{\partial \epsilon}{\partial t} + \frac{\partial \epsilon U_j}{\partial x_j} = \frac{\partial}{\partial x_j} \left(\frac{\nu_T}{\sigma_\epsilon} \frac{\partial \epsilon}{\partial x_j} \right) + C_1 \nu_T \frac{\epsilon}{k} \frac{\partial U_i}{\partial x_j} \left(\frac{\partial U_i}{\partial x_j} + \frac{\partial U_j}{\partial x_i} \right) - C_2 \frac{\epsilon^2}{k} \quad (3.2.2)$$

where σ_k and σ_ϵ are Prandtl numbers which relate the eddy diffusion to the momentum

eddy viscosity of k and ϵ , respectively. In mathematical terms, $\sigma_k = \frac{\nu_T}{\nu_k}$ and $\sigma_\epsilon = \frac{\nu_T}{\nu_\epsilon}$.

ν_T can be calculated from k and ϵ by the following relation:

$$\nu_T = C_\mu \frac{k^2}{\epsilon} \quad (3.2.3)$$

There are five constants present in the k - ϵ equations. These have been assigned an empirical value with the condition that the physical problem is related to attached boundary-layer calculation. The recommended values for this case are presented below [White and Corfield, 1991].

$$C_\mu = 0.09 \quad C_1 = 1.44 \quad C_2 = 1.92 \quad \sigma_k = 1.0 \quad \sigma_\epsilon = 1.3$$

3.2.1 Law of the wall

The presence of a body in the fluid will influence the characteristics of the fluid flow. Far from the body inertial forces will dominate, whereas close to surface of the body viscous forces are more important. This in turn leads to that the free stream parameters do not influence the viscous effects close to the wall. The flow field around the object or wall is then only dependent on the distance from the wall, y , fluid density, dynamic viscosity of the fluid and wall shear stress. The law of the wall is composed of these parameters:

$$u^+ = \frac{U}{u_\tau} = f\left(\frac{\rho u_\tau y}{\mu}\right) = f(y^+) \quad (3.2.4)$$

where u^+ is the dimensionless velocity, y^+ is the dimensionless distance from the wall, μ is the dynamic viscosity, τ_w is the wall shear stress and $u_\tau = \sqrt{\frac{\tau_w}{\rho}}$ is the friction velocity.

The no slip condition ensures that the fluid on the surface is stationary. In a very thin layer over the surface, the relationship between the distance from the wall and velocity is linear. This layer is the viscous sub-layer and the linear relationships is only valid within this layer, for $y^+ < 5$. Due to the linear nature of this layer, the law of the wall will be linear, $u^+ = y^+$. Viscous stresses are dominant in this region.

For $5 \leq y^+ \leq 30$ the law of the wall is neither linear nor logarithmic, making the relationship in this region hard to predict. This buffer layer has its stress contributions from both viscous and turbulent stresses. Spalding formulated an expression for the entire wall region in 1961 [Spalding, 1961]. This was later validated by fitting the data calculated from the formula to the mean velocity of a smooth pipe in distilled water.

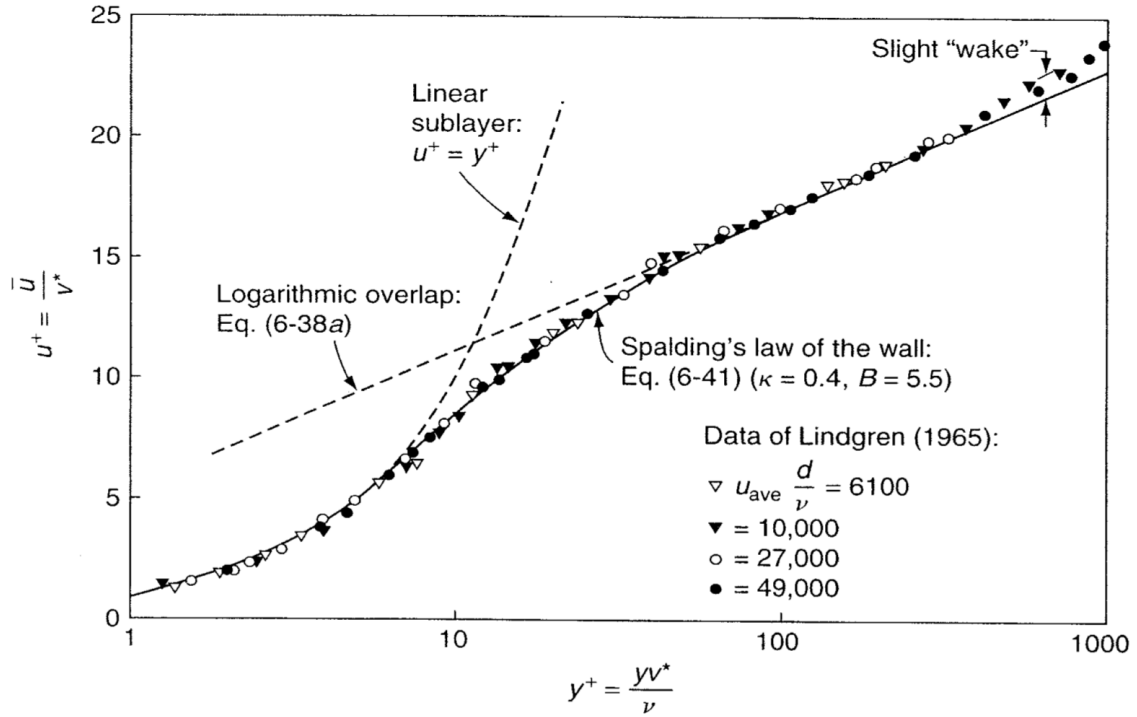


Figure 3.2: Spalding’s inner law expression compared with experimental data of a smooth pipe [White and Corfield, 1991].

The log-law is defined in the interval $30 \leq y^+ \leq 100$. This range is well outside the viscous sub-layer, and the mean velocity vary with the logarithmic y^+ . The Reynolds stresses inside this region is mostly constant. Furthermore, the local shear stress is assumed to be equal to the wall shear stress [Rodi, 1993]. Reynold stresses dominates in this region. The resulting equation is the log-law of the wall.

$$u^+ = \frac{1}{\kappa} \ln(Ey^+) \quad (3.2.5)$$

where κ is von Kármán’s constant and E is a roughness parameter. For flow past a hydraulically smooth wall κ is 0.41 and E is 9.8 [Versteeg and Malalasekera, 2007].

Log-law of the wall has been verified by comparing theoretical results against experimental data for a wide range of Reynolds numbers. The result of this comparison are illustrated in figure 3.3.

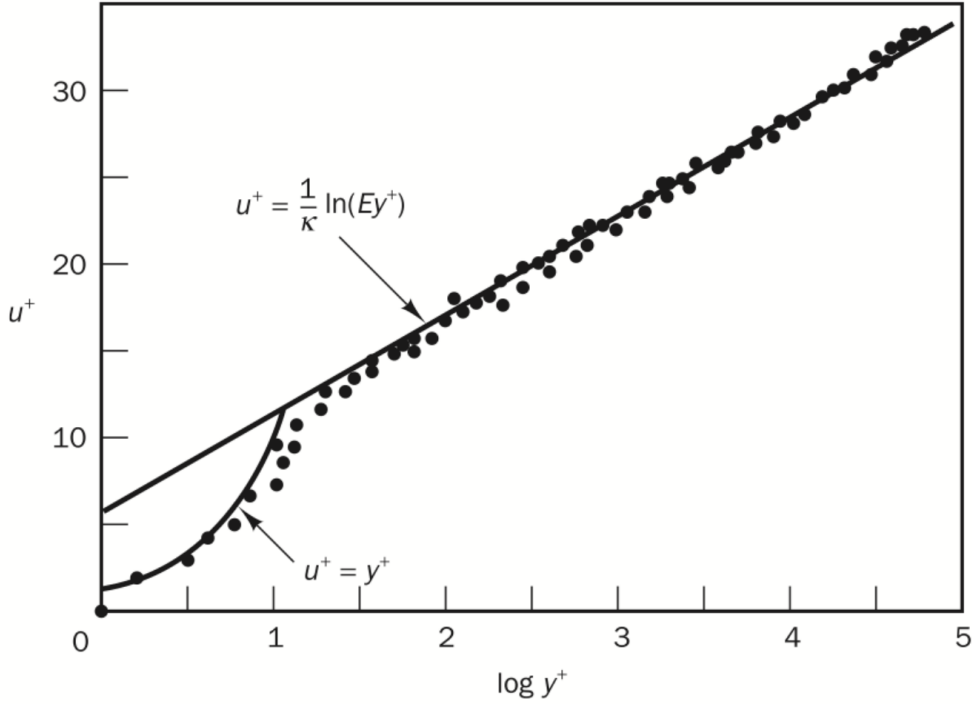


Figure 3.3: Velocity distribution for smooth pipe near pipe wall [Schlichting, 1979].

For a more thorough review regarding turbulence simulations and turbulence models, the reader is referred to Pope (2000), Schlichting (1979) and White (1991).

3.3 Courant number

The Courant number describes the number of cells a fluid particle will pass through from one time step to the next. As the flow field develops and encounter a body, the fluid particle velocity will increase when it is forced to circumvent said body. The distance travelled by the particle is $s = u\Delta t$ If this distance relative to the cell element length Δx is too large, the solver will have difficulties to maintain stability at the next timestep, since the fluid particle has passed through multiple steps. The Courant number describes this relation.

$$Co = \Delta t \sum_{i=1}^n \frac{u_{x_i}}{\Delta x_i} \leq C_{max} \quad (3.3.1)$$

where Co is the Courant number, Δt is the timestep, u_{x_i} is the velocity of the fluid particle and Δx_i is the characteristic length of the cell in the given direction.

When the maximum Courant number is less or equal to one, a fluid element will only pass through one cell to the next. This implies that not a single cell will be skipped. In

2D this requirement is expressed as

$$Co_{max} = \frac{u_x \Delta t}{\Delta x} + \frac{u_y \Delta t}{\Delta y} \leq 1 \quad (3.3.2)$$

To maintain stability a value lower than one is often necessary, due to local velocity increase.

3.4 OpenFOAM

OpenFOAM (Open Source Field Operation and Manipulation) is an open, C++ library of utilities. It is an open source code, granting the user the possibility to modify and add functionality or executables as needed. Included in this library are multiple solvers for different flow conditions, meshing utilities and visualisation software. Figure 3.4 illustrates the general structure of the library.

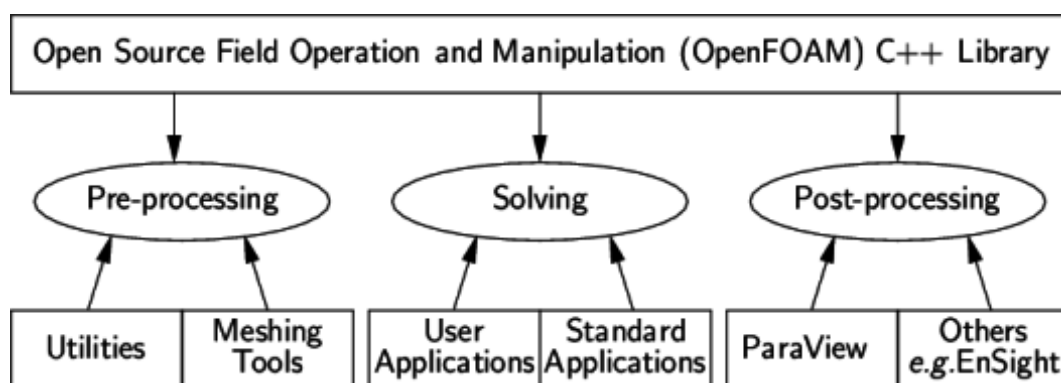


Figure 3.4: Structure of OpenFOAM[OpenFOAM, 2014]

Since OpenFOAM is object oriented, it's easy to translate physical and mathematical conditions into programming language. This is a clear strength of OpenFOAM in terms of functionality. The general procedure of implementing a model into OpenFOAM is as follows:

1. **Implementing a mesh:** This can be done either with external software or within OpenFOAM itself. The object of interest is modelled with the correct geometry and surrounded with the fluid domain. This domain is divided into cells. If the mesh is generated in an external program, it need to be converted into a format OpenFOAM can read.
2. **Selecting a solver:** The solver is essential in terms of getting the correct solution. As specified in section 2.2 the mathematical model will vary depending on the fluid

properties and what parameters shall be determined. Using a correct solver will reflect these considerations. The choice of solver might impact what boundary conditions that need to be specified.

3. **Selecting boundary conditions:** Physical boundary conditions on the boundaries of the fluid domain and object geometry have to be specified. These count as initial conditions and physical approximations due to the subject of interest is not surrounded with an infinite fluid.
4. **Specifying time domain and output:** Simulation time and data output has to be specified. It is important to set a correct time step, as a too large interval will cause instability and incorrect solution, whereas too small will lengthen the simulation time.
5. **Running the analysis:** The simulation can be run on a single core or multiple, according to the number of cells in the mesh. The user has to specify how the domain should be distributed between the cores.
6. **Simulate and evaluate the results.**

OpenFOAM requires a distinct file-structure to begin simulations. The mesh with accompanying boundaries. fluid properties and solver properties has to be specified in a *constant* directory. These parameters are the framework for every time step. The *0* directory contains the boundary conditions specified on the boundaries of the domain and on the body of interest. It also contains initial conditions. The *system* directory has the solver settings and control settings for time interval, solver used, residual control, output interval and quantities, etc. These directories need to be present and correctly set up before performing a simulation.

OpenFOAM has a wide selection of solvers. In this thesis the *pisoFOAM* are used for all simulations, with a modification that allows setting a maximum Courant number. *pisoFOAM* is a transient solver for incompressible fluids. It uses the PISO (Pressure Implicit with Splitting of Operators) scheme. For the laminar simulations the solver was set to run a laminar model. For the turbulent simulation the *kEpsilon* model was used. This model requires the flow to be fully turbulent. Wall treatment are satisfied by using wall functions. These are *kqRWallFunction* for k and *epsilonWallFunction* for ϵ . The functions satisfy the log-law equations described in section 3.2.1.

OpenFOAM supplements several schemes solve the Navier-Stokes equations. For time integration the second order backward scheme is being used. The gradient, Laplacian

and divergent are represented by the Gauss linear, Gauss limited linear and Gauss linear limited, respectively. These are all second order schemes. $k-\epsilon$ are the only exception, where an upwind, first order scheme is used for the divergent due to stability concerns. The schemes are specified in the *fvSchemes* file in the *system* directory. Additional details regarding the schemes can be found in the OpenFOAM User guide, section 4.4 [OpenFOAM, 2015].

For every solver in OpenFOAM, there are some corresponding subdictionaries. These are solver settings for different flow variables. For the pressure p a geometric-algebraic multigrid (GAMG) solver is used. The solver estimates an solution on a coarse mesh, and then mapping the resulting solution on a finer mesh. For u , k , ϵ and $\overline{u'_i u'_j}$ a diagonal incomplete lower-upper preconditioner is used for the preconditioned conjugate gradient (PBiCG) solver. These are the preconditioners used in this thesis and were specified in *fvSolution* in *system* directory [OpenFOAM, 2015].

To save time the mesh were decomposed into sub-domains between multiple processors and run in parallel. The *scotch* decomposition method was used. This method distributes the mesh between the processors on the principle of minimising processor boundaries.

The output control, scheme and solution dictionary used in the simulations are attached in Appendix 5.

3.5 Mesh

The initial step of performing an CFD analysis, is to create a mesh. The Navier-Stokes equations can't be solved analytically. Instead it is solved by discretize the equations and solved for each cell. It is therefore important to create a high-quality mesh.

There are three main categories of grid used in meshing, structured single-block, structured multi-block and unstructured grids. From these three multiple transitional methods have derived. Figure 3.5 illustrates the difference between the grids for a simple element.

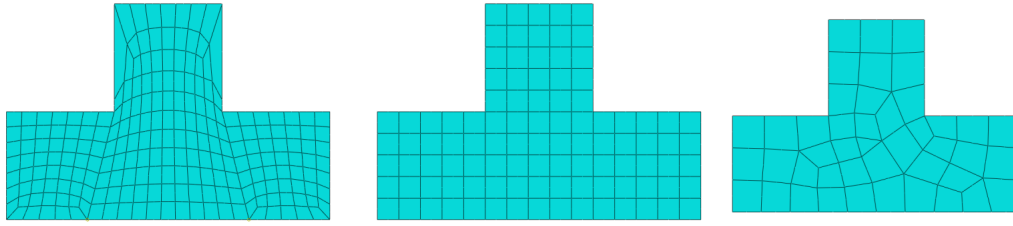


Figure 3.5: The main grids in meshing. From left to right: Structured single-block, multi-block and unstructured mesh.

The structured, single-block grid is the simplest mesh solution. It can be directly mapped from the physical to the computational domain by three indices. The lack of flexibility and customisation are the obvious drawback of this structured mesh. A multi-block grid divides the physical domain into several blocks, whom each can customise mesh grading separately from the rest. The main advantage is more customisation, but at the cost of being more time-consuming. Every block has it's own indices, and has to be connected with a corresponding block on each face. Unstructured grid are the most customisable but requires additional computer resources to track each element, as there are no indices to do so.

A good mesh is indicated by three mesh parameters: smoothness, skewness and aspect ratio. A good smoothness means that there are no large jumps in cell area from the one face to the next. Skewness is how close the cell is to the original shape, for instance an hexahedron should appear as one, and not a parallelepiped. Aspect ratio are the relation between characteristic length and height. Having a good agreement between these three criteria result in a good quality mesh. A poor mesh will produce erroneous result and increase computational time.

Another consideration are total mesh cells. Too many, and the increase in computational time does not correspond to significant increase in accuracy. Too few, and the solution will be inaccurate. To keep the number of cells at a minimum, areas of importance can be assigned more cells than areas that don't affect the solution at all. Having a gradually finer mesh in the boundary layer are crucial to obtain correct results.

3.6 Vilje

For many practical applications of CFD the need for more computational resources than what is possible with a personal computer is necessary.

The simulations were performed on Vilje, a SGI Altix ICE X system. It is acquired by

NTNU together with met.no and UNINETT Sigma. It runs SUSE Linux and are used for research by students at NTNU, other Norwegian universities and research institutes. It is used by met.no to perform numerical weather prediction for weather forecasts. Details about Vilje are presented below

- Number of nodes: 1404
- Processors per node: Two eight-core processors
- Processor speed: 2.6 GHz
- Memory: 32 GB per node

Chapter 4

Model

The task of this thesis is to investigate the flow around the Oseberg rudder using CFD. The objective is to check if the problems encountered during sailing of the Viking ship could be explained with a numerical simulation. To be able to perform such an analysis, the mesh, initial and boundary conditions have to be specified. This section will present the necessary input.

4.1 NACA0012 airfoil

The test set-up and corresponding results were performed as a part of an project thesis. It is included as study in the degree of accuracy that can be obtained with CFD. [Heggem, 2014].

The NACA0012 airfoil is interesting for several reasons. Firstly, it has no camber and therefore do not provide any lift at zero angle of attack. This is crucial for a rudder. Secondly, there exist a great deal of experimental and numerical data regarding the performance of this airfoil. It is therefore a good benchmark to check the validity of the simulated results.

Any CFD simulation requires a mesh. In this process MEGA is used, an in-house developed mesh generator at NTNU. The strength of MEGA is that it is able to input a surface as coordinates or as a 3D surface. This can then be used to model surface lines correctly between two nodes. The boundary condition and domain are specified in Figure 4.1

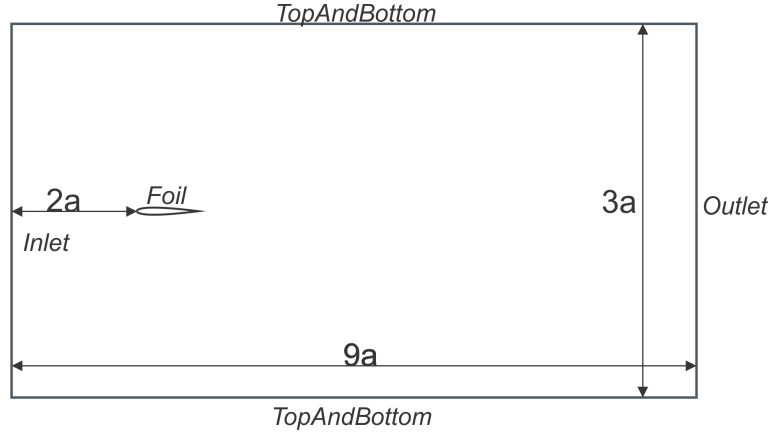


Figure 4.1: NACA0012 airfoil mesh boundary condition and set-up.

The mesh has to be finer in the regions close to the foil than in the fluid field downstream. This is reflected in the mesh used in the study.

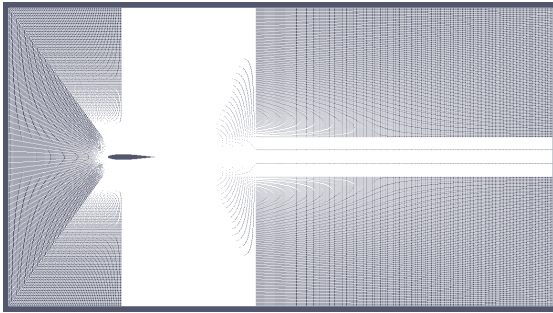


Figure 4.2: Overview of the NACA0012 mesh

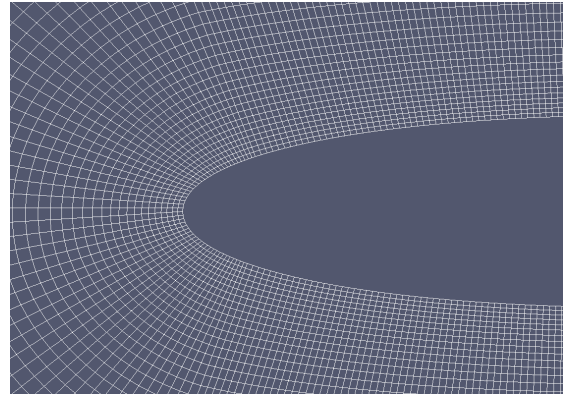


Figure 4.3: Cells near the leading edge of the NACA0012 foil.

At the boundaries the boundary and initial conditions need to be specified after the mesh has been implemented into OpenFOAM. Table 4.1 show the variables and restrictions used:

Name	U[x y z] [m/s]	Pressure P/ρ [m^2/s^2]
Geometry surface	[0 0 0]	zeroGradient
Inlet	\vec{U}	zeroGradient
Outlet	zeroGradient	0
Top & bottom	zeroGradient	zeroGradient
Out of plane	empty	empty

Table 4.1: Boundary and initial conditions in OpemFOAM for NACA0012 airfoil

The condition *zeroGradient* means that the gradient to a quantity should be zero in the direction normal to the boundary. The *empty* condition enforces that no solution is necessary in the out of plane direction, in this case z-dir. All the simulations are run as a two dimensional case, so 3D effects are not included, hence the *empty* condition. The no-slip condition is modelled by forcing the fluid velocity to be zero on the object's surface. At the outlet, far from the object of interest, the pressure is forced to become zero. This is a good approximation as long as the outlet is far from the fluid disturbance due to the presence of a body.

The simulations were performed with the NACA0012 airfoil with an cord length of 1 m and a thickness of 0.001 m. The foil were tested under the following flow parameters:

Reynolds number	Angle of attack [degrees]
500	0
500	10
2000	0

Table 4.2: Test conditionsfor the NACA0012 airfoil

For the cases where the inflow velocity induced an angle of attack on the foil, the mesh is configured so the finer mesh downstream from the foil would follow the wake. Furthermore, the boundary conditions was modified as to reflect the new case. The sides are changed from being identical symmetrical into an inlet and an outlet, depending on the direction of the flow.

For this configuration a simulation with a 3D foil is also performed. The NACA0012 is given a span s of 2 m, and the domain is elongated in the z-direction to prevent bottom effects. The aspect ratio is $Asp=2$ for this case, and the depth from the tip of the foil were 4 metres. The bottom were modelled as a side and the top were given the *symmetry* boundary condition.

4.2 Oseberg-rudder

The rudder is tested with several angles of attack, $-\alpha$, and rudder rake angles, $-\beta$. Figure 4.5 illustrates how the angles and coordinate system are defined.

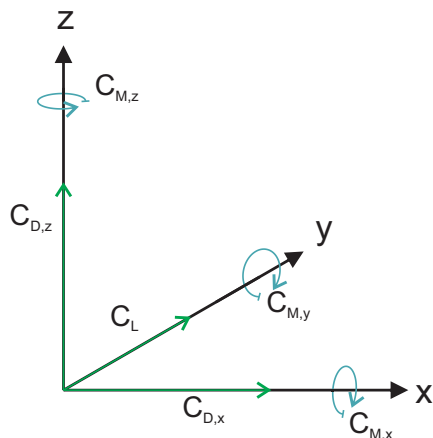


Figure 4.4: Definition of forces and moments.

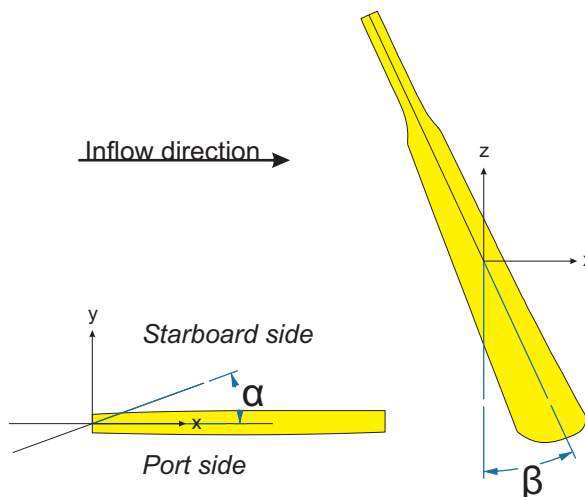


Figure 4.5: Oseberg rudder orientation and angle definitions.

The rudder is analysed at three different flow regimes. The Reynolds number is chosen as 250, 1000 and 2.4×10^6 . The different angles tested are defined in table 4.3.

Rudder rake angle β	Wetted surface S [m ²]	Angle of attack α				
20	1.1134	-10	-5	0	5	10
25	1.1061	-10	-5	0	5	10
30	1.1160	-10	-5	0	5	10

Table 4.3: Values for rudder rake and angle of attack

The three dimensional domain surrounding the modified Oseberg rudder is based upon the experience obtained from modelling the NACA0012 airfoil. A structured, multiblock mesh is used. The block upstream from the leading edge is configured to be a C-mesh, to save computational power. The blocks downstream and at the sides of the rudder are structured as H-meshes, so that proper fineness in the wake and close to the rudder can be modelled. The inlet is curved due to the choice of a c-mesh at the leading edge. The reason for this decision is to minimise the cell deformation caused in the transition from boundary layer zone to outer domain. A straight inlet would stretch the cells approaching the corner of the domain, as they need to cover a larger distance than the cells in the

middle of the domain. A curved inlet will minimise this effect. The final domain is structured as in the following figure:

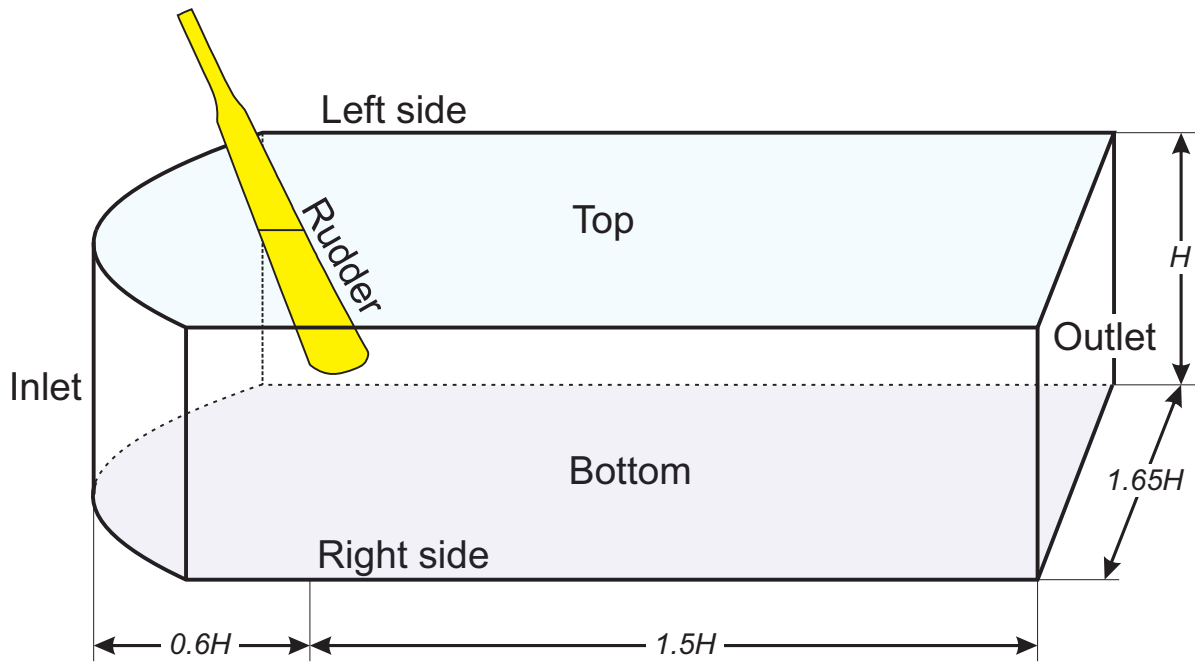


Figure 4.6: Domain configuration of the Oseberg rudder

H is set as 4, to give a sufficient distance from the rudder to the domain boundaries. A larger domain can be used, but this would result in longer computational time due to additional cells.

The domain surrounding the rudder is divided into ten blocks in the xy -plane, each being further divided along the z -axis. This makes it easy to vary the boundary layer thickness and cell incrementation. The blocks surrounding a foil section have been illustrated in the image below. Additional block are defined downstream from the rudder, as to decrease the cell density in this area. This is also done far from the body, e.g. along the boundaries of the fluid domain. The total number of blocks in the entire 3D domain were 102.

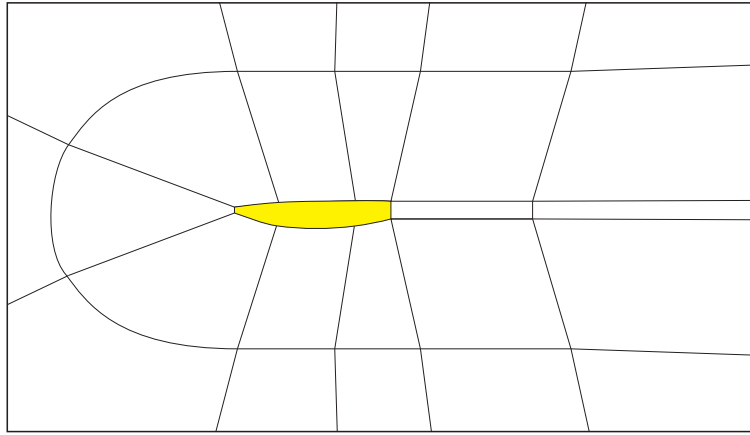


Figure 4.7: The blocks surrounding a foil section of the Oseberg rudder

Figure 4.8 displays the resulting mesh, divided into top, front and side sections.

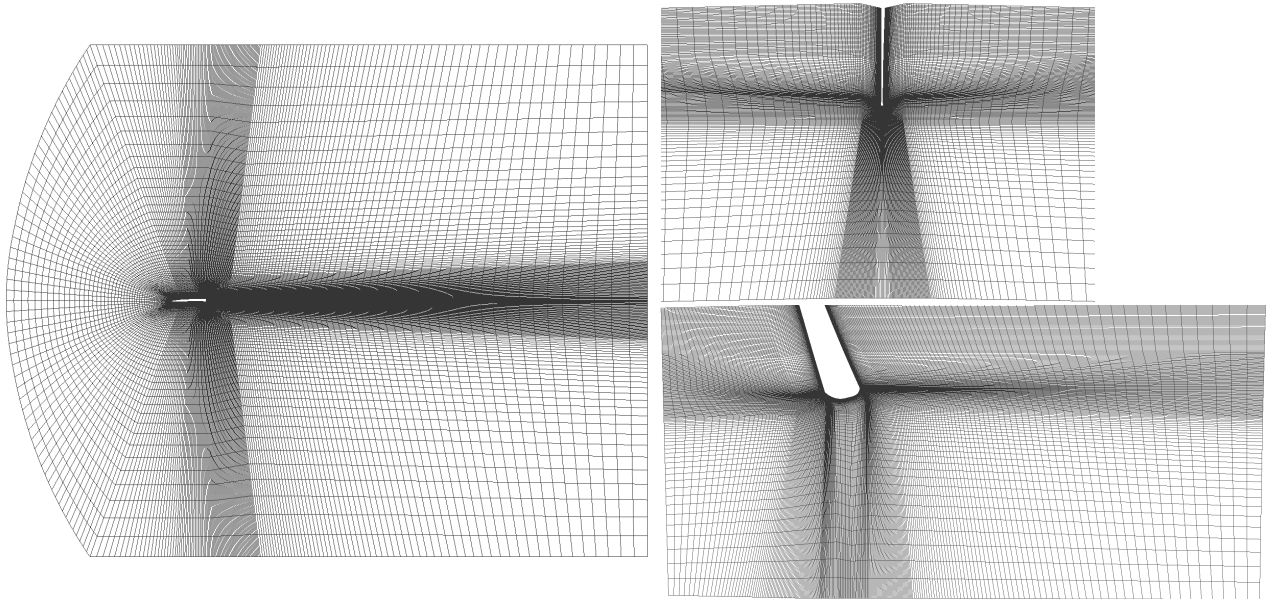


Figure 4.8: The mesh surrounding the Oseberg rudder. From left to right: Top, front and side view of the domain. The top view illustrates the choice of C-mesh at the leading edge.

Creating a mesh for a 3D model is a quite time-consuming and extensive task. The boundary layer must be modelled with correct fineness in all three dimensions. Furthermore, the model of the rudder have sharp edges on all transition zones. These areas will experience high pressure gradients and are crucial in order to obtain correct results. Great care is necessary to resolve these areas adequately.

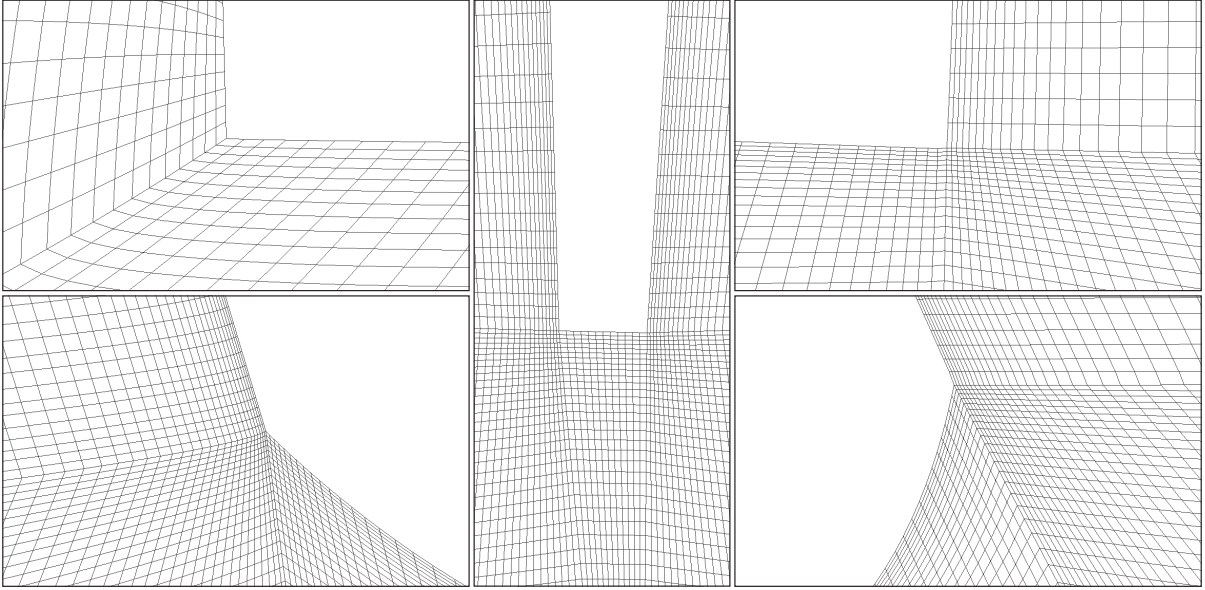


Figure 4.9: Close-up view of the cells surrounding important parts of the rudder. From top and clockwise: The mesh surrounding the leading edge, leading edge tip, trailing edge, rudder front tip and bottom tip.

The boundaries normal to the z-plane have to be specified since this is no longer a 2D-case. The boundary along the free surface were chosen to have the *symmetryPlane* boundary condition. This condition fulfils the requirement to have no flow flux over the rudder or through the surface. No waves will be generated due to the requirement of symmetry over this plane, so surface effects are neglected. The bottom of the domain have identical conditions as the sides, as it also represents unlimited fluid.. The complete boundary conditions are presented in table 4.4.

Name	U[x y z] [m/s]	Pressure [P/ ρ]
Rudder surface	[0 0 0]	zeroGradient
Inlet	\vec{U}	zeroGradient
Outlet	zeroGradient	0
Top	symmetryPlane	symmetryPlane
Bottom	zeroGradient	zeroGradient
Sides	zeroGradient	zeroGradient

Table 4.4: Boundary and initial conditions for the Oseberg rudder

When the flow were simulated with an angle of attack, the wake of the rudder and domain sides were tilted equally to accommodate this. This is done to maintain equal conditions between the simulation, to minimise the risk of numerical error.

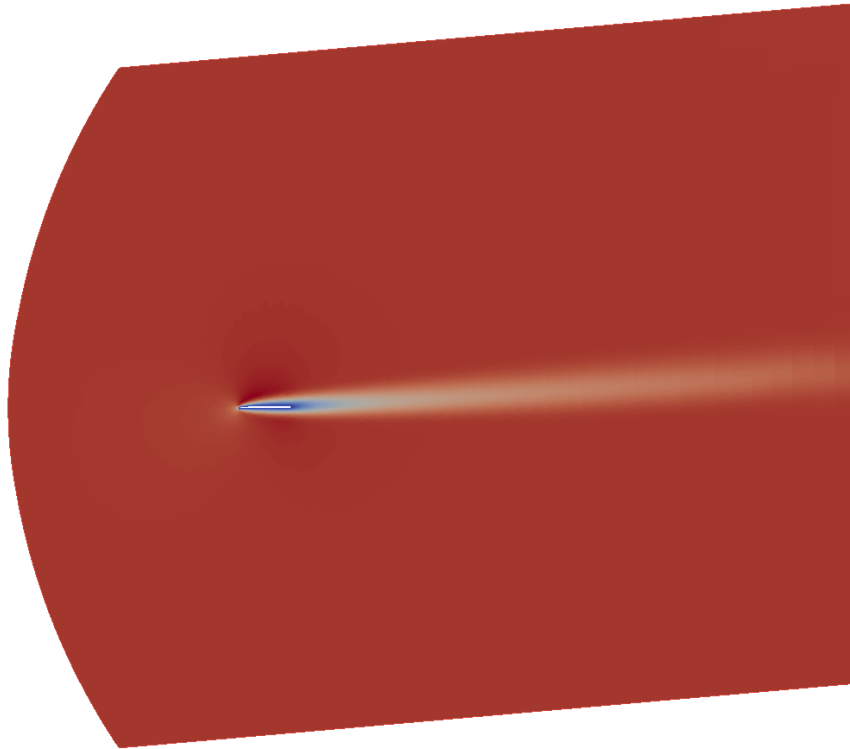


Figure 4.10: The domain configuration for a fluid flow with an angle of attack equal to $\alpha=5$ degrees.

The final mesh

All the different mesh configurations were run in three different flow regimes. The settings used are presented in table 4.5. The flow at Reynolds number 2.4×10^6 corresponds to the Oseberg ship sailing at a speed of 10 knots.

Reynolds number	$U_{magnitude}$ [m/s]	ρ [kg/m ³]	ν [m ² /s]
250	0.25		4.95×10^{-4}
1000	1	1025	4.95×10^{-4}
2.4×10^6	1		2.03×10^{-7}

Table 4.5: Fluid properties for the Oseberg rudder

4.2.1 k- ϵ boundary conditions

In the previous section the standard conditions for running a laminar simulation are defined. For a turbulent simulation additional input is required regarding the choice of turbulence model. For k- ϵ the values of k, ϵ and ν have to be specified on the boundaries and on the rudder. The latter is strictly not necessary, as OpenFOAM calculates it from k and ϵ . However, specifying initial values close to the correct one for all three variables

on the rudder will ensure a faster convergence.

For the inlet boundary condition the values for the free stream are specified. The turbulent kinetic energy k and energy dissipation ϵ are determined from the following relations:

$$k = \frac{3}{2}(I_u U_\infty)^2 \quad (4.2.1)$$

$$\epsilon = \frac{C_\mu k^{3/2}}{0.1L} \quad (4.2.2)$$

For a regular incoming flow the turbulent intensity $I_u = 0.8\%$. Due to the presence of a hull close to the rudder an increased degree of turbulence is assumed. Therefore the turbulence intensity is set to $I_u = 5\%$, to ensure that the incoming flow are turbulent. The turbulent length were based upon the average cord length and the non-dimensional turbulent length scale $\frac{L}{D} = 0.0045$. [Ong, 2012]

The values for k , ϵ and ν_t on the rudder surface are calculated from using the log-law equation and the following relations:

$$k = \frac{u_\tau^2}{\sqrt{C_\mu}} \quad (4.2.3)$$

$$\epsilon = C_\mu^{\frac{3}{4}} \frac{k^{\frac{3}{2}}}{\kappa h_p} \quad (4.2.4)$$

$$\nu_t = C_\mu \frac{k^2}{\epsilon} \quad (4.2.5)$$

where h_p is the distance from the wall to the closest cell. In the chosen mesh for this thesis the value of h_p is 5.3×10^{-4} m. The von Kármán's constant κ is set to 0.41. For $30 \leq y^+ \leq 100$ the log-law equation (ref. equation 3.2.5) is valid and $y^+ = u^+ = h_p \frac{u_\tau}{\nu}$. Table 4.6 displays the boundary condition for the turbulence model used in this thesis.

Boundary name	k	ϵ	ν_t
Rudder surface	0.00123	0.04009	3.3834×10^{-6}
Inlet	0.00375	0.09278	2.1827×10^{-6}
Outlet	zeroGradient	zeroGradient	2.1827×10^{-6}
Top		symmetryPlane	
Sides & bottom		zeroGradient	

Table 4.6: Initial and boundary conditions for the k- ϵ turbulence model.

Chapter 5

Results

In this chapter the results obtained by performing the CFD analysis are being presented and discussed. Section 5.1 displays the results obtained from the project thesis.

5.1 NACA0012 airfoil

Correct modelling of the boundary layer is crucial to obtain correct result. By varying the number of cells close to the body the effect of this upon the solution can be studied. A domain size of “a=2” is chosen to be sufficient. The smallest element in the boundary layer is chosen to be representative for the resolution in the boundary layer. At this Reynolds number the variation of domain size is affecting the result substantially more than the variation in boundary layer. This is important knowledge to take into account when modelling geometries in a fluid . However, as Reynolds number increase the boundary layer thickness will decrease, requiring more cells close to the body to model this correctly [White, 1999]. It is therefore safely assumed that the boundary layer cells will be more and more important as Reynolds number increase.

A 2D airfoil will not experience vortex shedding due to its streamlined shape. If the angle of attack is large enough, the foil will stall and flow separation will occur. Due to the orderly fashion of the flow past the foil the results will converge quickly.

Name	Re	α	$A_{Cell,min}$ [cm ²]	$Nr_{Cells,tot}$	C_D , avg.	C_L , avg.
MN1	500	0	3.68	365700	0.17435	-1.5314e-04
MN2	500	10	4.14	534600	0.1324	0.4675
3DMN2	500	10	0.3196	2659120	0.1452	0.3589
MN3	2000	0	3.68	365700	0.0837	-2.7229e-04

Table 5.1: NACA0012 airfoil lift and drag coefficient at varying Reynolds numbers.

The results were obtained after the flow had stabilised. This happens after approximate $t=0.8 u/c$ for the foil with angle of attack and even faster with zero angle of attack. The flow behaved as expected. It will stagnate at the leading edge. The fluid will be forced to accelerate on both sides of the foil, leading to a negative pressure distribution. It will then re-align itself when it arrives at the following edge, and the pressure over the foil will be zero as the flow velocity returns to the inflow velocity. For a foil with an angle of attack, we will get flow separation earlier on the top surface. The fluid downstream from this separation point will travel with the foil, resulting in stalling vortex streamlines. The separated streamlines will re-attach itself to the separated flow at the following edge.

5.2 Oseberg rudder

The domain size is based on the experience obtained from performing a CFD analysis of a NACA0012 airfoil, as described in the previous section. An H equal to 4 was chosen. Furthermore, a convergence analysis was performed to determine the required amount of cells in the domain. To keep the cases as comparatively as possible, the cell density of each mesh are approximately constant. These mesh are named M0 to M4, from the mesh with the lowest amount of cells to the highest. The Reynolds numbers were set at 250 and 1000, inflow angle $\alpha=0$ and the rudder rake angle $\beta=25$ degrees. The cross-sections of the Oseberg rudder has a varying cord length, as can be seen in figure 1.3. The wetted surface of 1.1061 m² was used to calculate the drag and lift coefficients. The results are presented in table 5.2.

Reynolds number	Name	$A_{Cell,min}$ [mm ²]	$V_{Cell,min}$ [mm ³]	$Nr_{Cells,tot}$	C_D	%	C_L	%
250	M0	1.9180	2.9031	2402136	0.1277		-0.0255	
	M1	1.2132	2.9031	3126552	0.1280	0.23	-0.0261	2.35
	M2	0.7295	2.9031	3385272	0.1283	0.23	-0.0265	1.53
	M3	0.4450	1.458	3770352	0.1284	0.08	-0.0267	0.75
	M3t	0.4450	1.458	3770352	0.1284	0.00	-0.0267	0.00
	M4	0.0513	0.055	5087304	0.1287	0.23	-0.0265	0.75
1000	M0	1.9180	2.9031	2402136	0.0623		-0.0265	
	M1	1.2132	2.9031	3126552	0.0617	0.96	-0.0274	3.40
	M2	0.7295	2.9031	3385272	0.0618	0.16	-0.0277	1.09
	M3	0.4450	1.458	3770352	0.0618	0.00	-0.0280	1.08
	M4	0.0513	0.055	5087304	0.0619	0.16	-0.0284	1.43

Table 5.2: Mesh convergence of hydrodynamic lift and drag coefficient for the Oseberg rudder

To maintain a stable solution and not waste computational resources, the *pisoFoam*-solver is used with adjustable time-steps as to keep the Courant number at a maximum of $Co=0.7$. The mean Courant is approximately 0.014. This ensured good stability during the simulations.

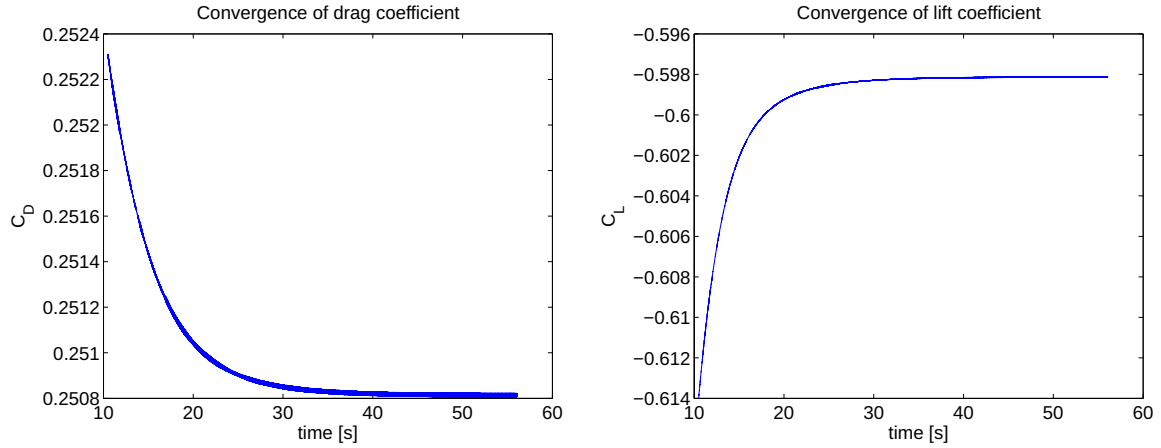


Figure 5.1: Convergence of instantaneous lift and drag coefficient for rudder rake angle $\beta=30$ and angle of attack $\alpha= -10$ at Reynolds number 250

The flow is stationary when it has converged at $Re=250$. This led to a rather quick convergence of forces, around 40 wall-clock seconds, or $20 U_\infty/c$. The simulations were continued until $32 u/c$, as to eliminate any fluctuation of forces. The difference from the chosen mesh to the finest mesh meant an increase in accuracy on average by 0.42%, but at the cost of 35% more cells.

A time study of mesh M3 were performed, named M3t. A Courant number maximum is set at $Co=0.2$, to check the induced errors from having a higher time-step. The resulting drag and lift coefficient from a smaller time-step were virtually non-existent, resulting in an accuracy gain of 0.02 %.

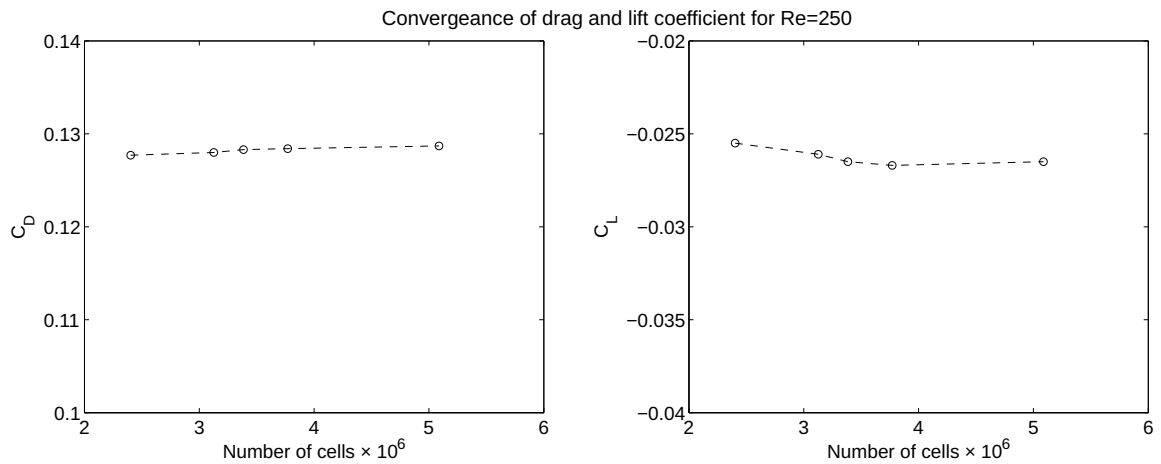


Figure 5.2: Mesh convergence of drag and lift coefficient for $\alpha=0$, $\beta=25$

The solution for $\alpha=0$ at $Re=1000$ was also stationary when the results had converged. This happened at approximately the same $t=u/c$. The lift coefficient increased more in

this case in comparison with $Re=250$, with an increase of 1.43% from M3 to M4. The difference in drag coefficient between the same meshes are lower.

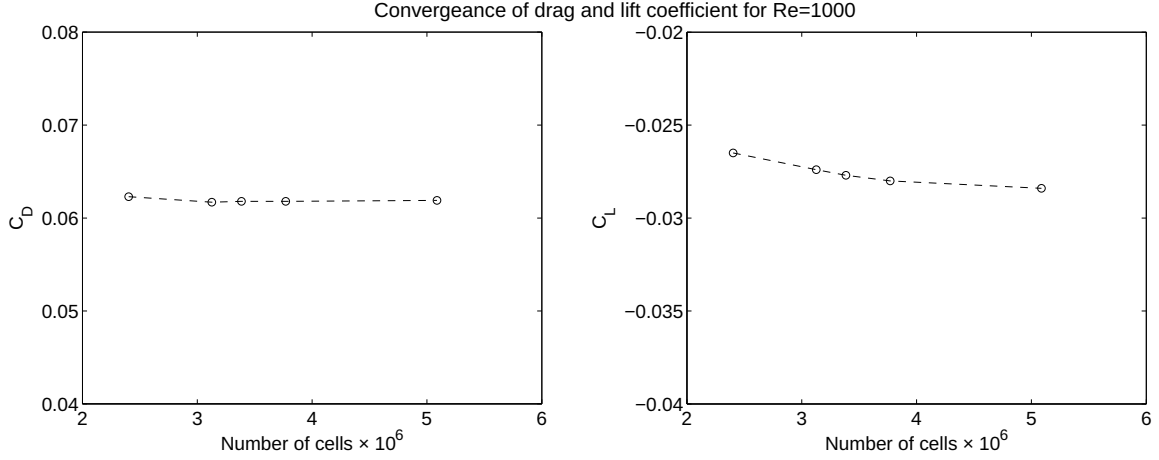


Figure 5.3: Mesh convergence of drag and lift coefficient for $\alpha=0$, $\beta=25$

To further check the mesh convergence, Mesh M4 and M3 were compared with an angle of attack $\alpha=-10$ degrees. At $Re=1000$ the rudder will experience vortex shedding at this Reynolds number. Obtaining accurate results in this condition are therefore important. The results are from a body-fixed coordinate system, hence will differ from the results presented in section 5.2.3.

Name	Re	α	C_D	$C_{D_{SD}}$	C_L	$C_{L_{SD}}$	St
M3	250	-10	0.1085	-	-0.2580	-	
M4	250	-10	0.1086	-	-0.2576	-	
M3	1000	-10	0.0507	9.8×10^{-5}	-0.2120	5.5×10^{-4}	0.5460
M4	1000	-10	0.0516	1.1×10^{-4}	-0.2104	6.2×10^{-4}	0.5420

Table 5.3: Mesh convergence of hydrodynamic lift and drag for the Oseberg rudder

The largest discrepancy are in the values in lift and drag coefficient standard deviation. The main contributor to the larger values in M4 are due to slower convergence of solution due to increased computational time. If the simulation were to be continued further, the standard deviation would decrease. The difference in drag coefficient are 1.74%, whereas for lift coefficient and Strouhal number the difference are 0.75% and 0.73%, respectively.

The small difference between results and the large difference in computational resources meant that the mesh M3 were deemed sufficiently accurate, and is chosen for the rest of the thesis.

It is difficult to check the validity of these results, as nothing comparable has been performed before. However, based on the convergence study and the previous experience with NACA airfoils a certain degree of confidence can be established.

The turbulent simulation are more sensitive to fineness in the boundary layer. Therefore additional cells and slightly finer increment towards the rudder are implemented. As a result, the total number of cells in mesh M3 are increased to 4787712. The result of this increase in cell count lead to a corresponding increase in computational cost. However, the y^+ value were on average 47, well within the interval set by the log-law of the wall. The maximum and minimum value of y^+ were 242 and 8, respectively.

5.2.1 Pressure forces

The Oseberg rudder were tested at Reynolds number 250 and 1000, and at some angles of attack at $Re=2.4 \times 10^6$. The limited number of angles of attack tested in turbulent condition are due to unforeseen technical difficulties, as will be discussed in greater detail in section 6.8.1.

The resulting forces from the fluid flow are divided into two contributions, pressure and viscous forces. Having a stagnation point on the rudder will cause a positive pressure along the leading edge due to de-acceleration of fluid particles. Since the rudder have an abrupt transition from the edge to the side of the rudder, most of the positive pressure will act in the x-direction, resulting in a large resistance experienced by the the rudder. At the edge of the leading edge, the flow will separate. Depending on the inflow angle α this will cause a suction pressure on either side of the rudder, resulting in a lift and drag force.

Since the rudder has a rake angle, the pressure force for will give a force contribution in x- and z-direction. The resulting force coefficient were labelled C_{D_x} and C_{D_z} , respectively. The rudder rake angle will therefore influence the maximum pressure force coefficient. Increasing rudder rake will lead to an increased pressure force coefficient in z-direction, but will reduce it in x-direction. The total pressure resistance in the inflow direction will therefore decrease with increasing rudder rake angle β .

The pressure drag is larger for negative angles of attack than for positive. There is a more pronounced flow separation at $\alpha=-10$ than for positive angles. A suction pressure will be generated as a consequence, and this give additional drag for negative angles. Since the pressure act perpendicular on the area which it is generated, most of the force contributions will be in the x- and y-directions, with minor force contribution along the

z-axis.

Increasing α will force the fluid on one side of the rudder section to move faster than the other. Where the fluid velocity is lower, there will be a positive pressure. Both of these effects generate pressure lift on the rudder. A comparison between the velocity field are presented in figure 5.4. A complete sectional view of the velocity field at $Re=250$ are presented in appendix 4.

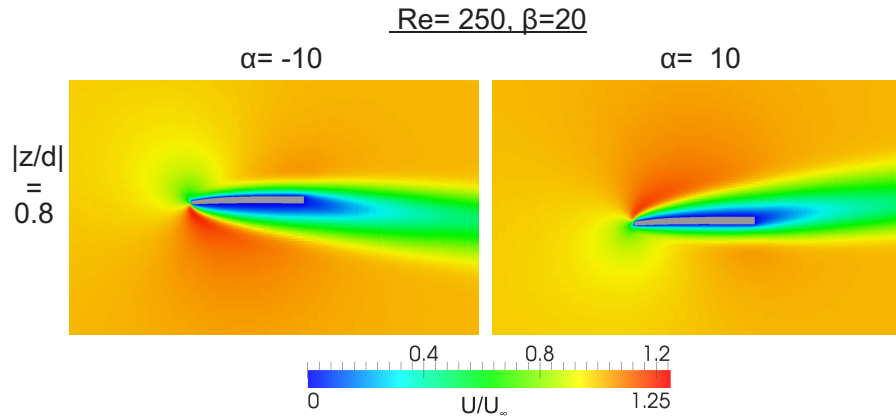


Figure 5.4: Velocity field for $\alpha=\pm 10$ at $Re=250$, $\beta=20$.

Near the free surface where the rudder cross sections rapidly thickens, there will also be a force contribution in the negative z-direction. The resulting pressure force coefficients from pressure distributed along the surface of the rudder is presented in figure 5.5.

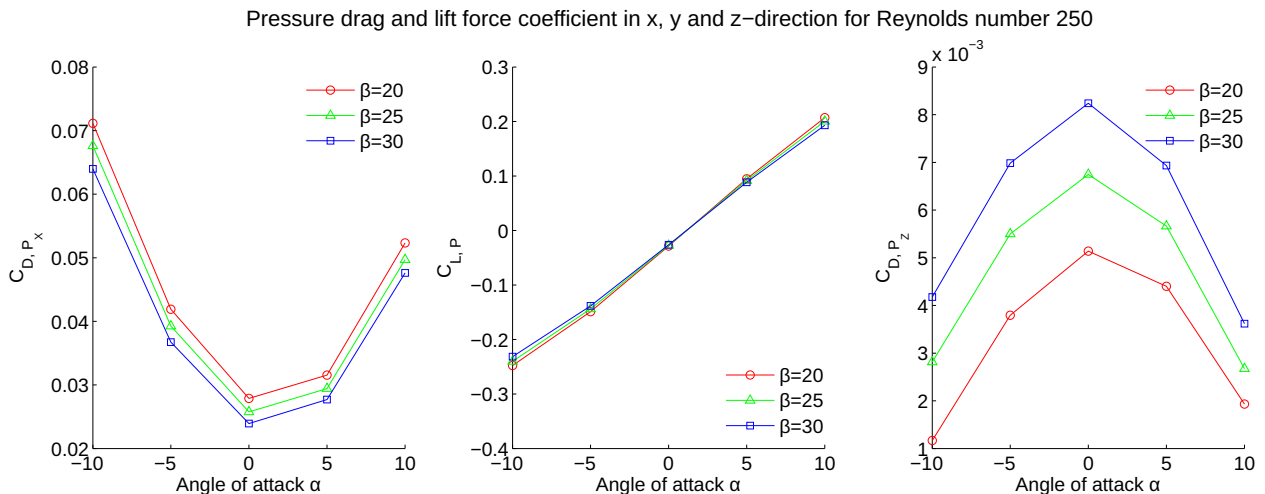


Figure 5.5: Pressure forces for Reynolds number 250.

At Reynolds number 1000 the pressure forces will be very similar as the ones the ruder experienced at $Re=250$, with lower force coefficient in z-direction. The major exception is

at inflow angle of attack $\alpha = -10$ degrees. This is due to larger flow separation and vortex shedding occurring at this configuration, increasing the drag experienced by the rudder.

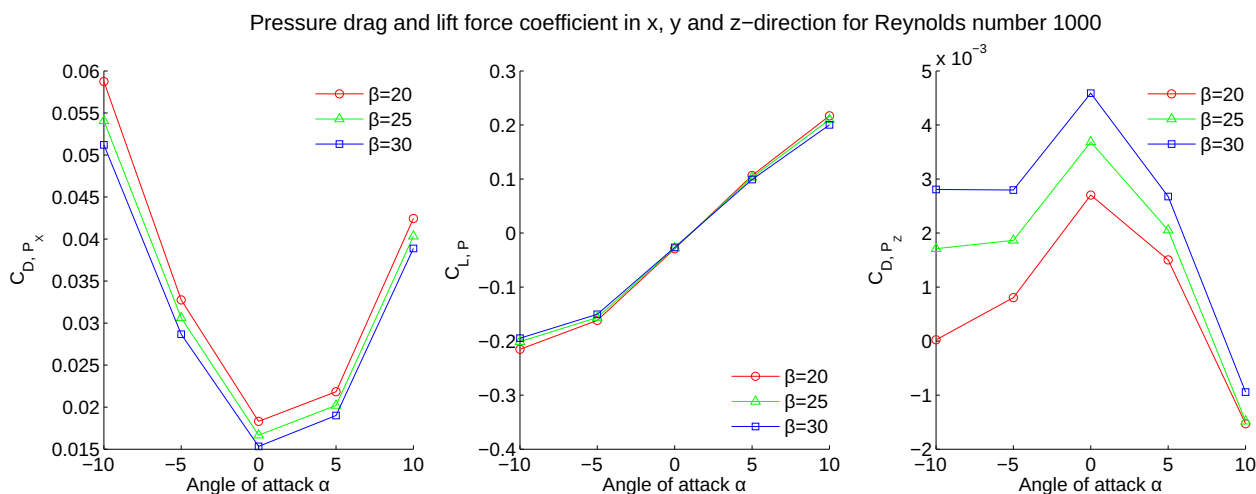


Figure 5.6: Pressure forces for Reynolds number 1000.

5.2.2 Viscous forces

The forces acting in x-direction is dominated by viscous forces at low Reynolds number. This can be seen by comparing the force in x- and z-direction between viscous (figure 5.7) and pressure (figure 5.5) forces. The viscous forces are due to the fluid shear stress resulting from the transition from zero velocity on the rudder surface, to the inflow velocity at the end of the boundary layer.

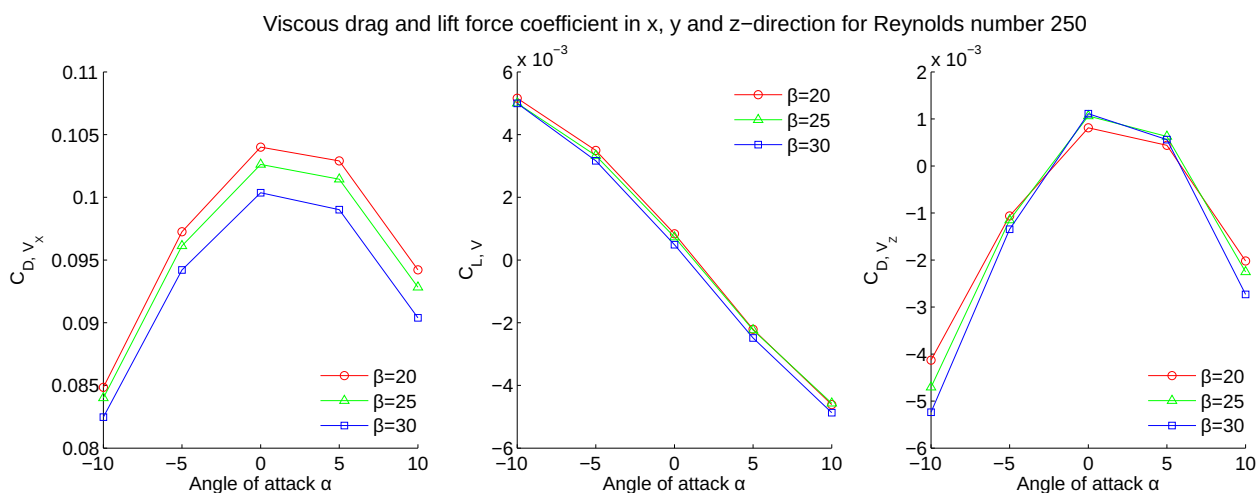


Figure 5.7: Viscous forces for Reynolds number 250.

When pressure lift is generated at $\alpha=10$, it will work in the positive y-direction. At this angle, the rudder is rotated toward port. The resulting viscous force will be decomposed

then act in the negative y-direction. This behaviour act as expected, and are clearly indicated in the viscous lift force coefficient. The same effect are observed in the viscous drag force. When $\alpha \neq 0$, less viscous force will act along the x-direction.

As the fluid velocity increases from Reynolds number 250 to 1000, the viscous force coefficient decreases.

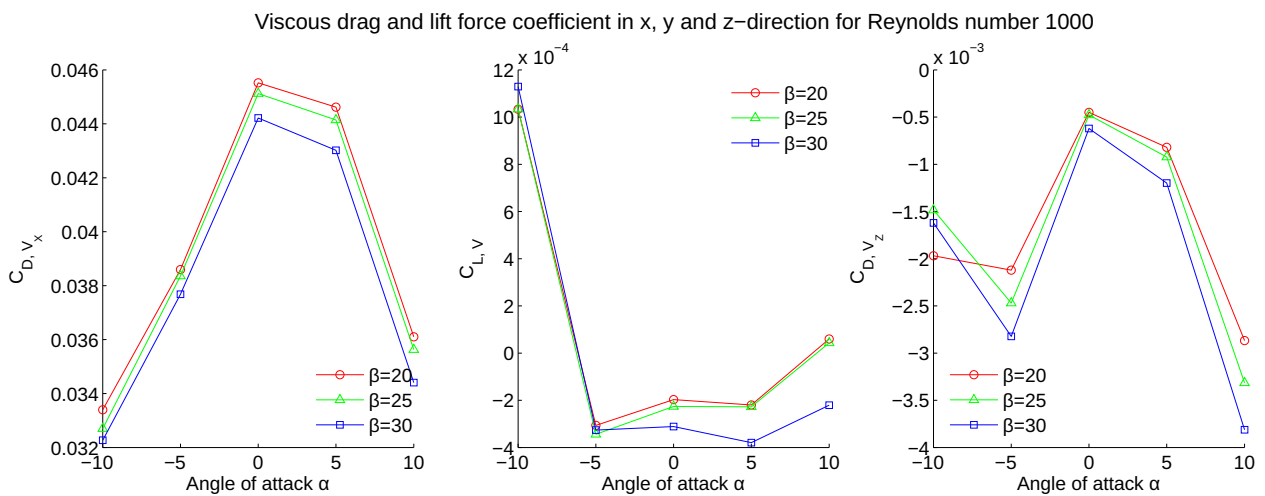


Figure 5.8: Viscous forces for Reynolds number 1000.

5.2.3 Total forces experienced by the rudder

When combining both the contributions from viscous and pressure effects, the total forces acting on the rudder are determined. The total resistance experienced by the rudder is decreasing when the Reynolds number is increased from 250 to 1000. The main reason for this behaviour is the lessened importance of viscous resistance.

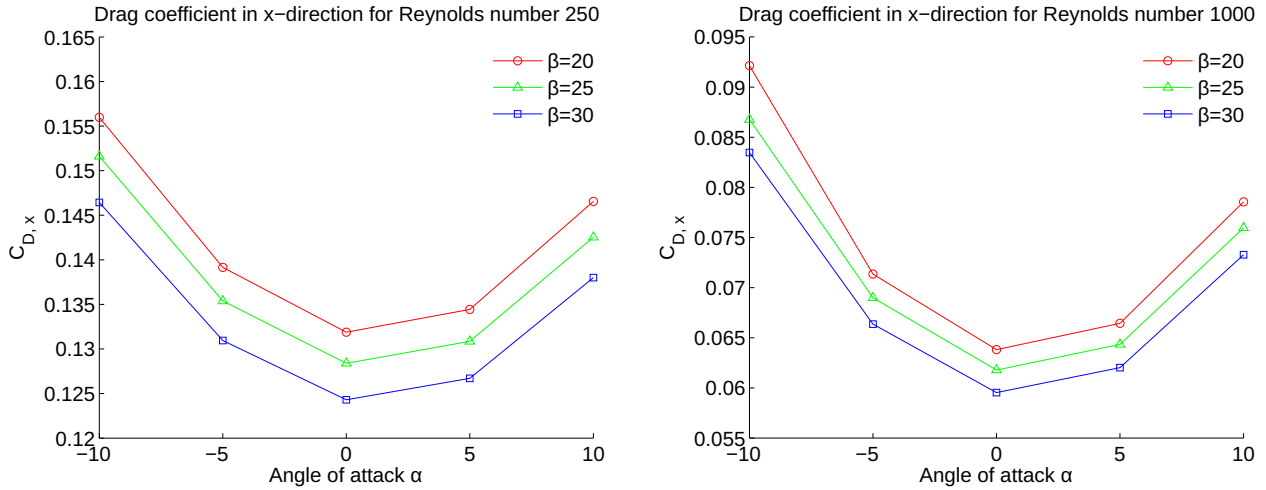


Figure 5.9: Total force in x-direction for Reynolds number 250 and 1000.

Increasing angle of attack will reduce the drag coefficient by the rudder, with the exception at $\alpha = -10$ degrees at $Re=1000$. This is due to vortex shedding, and will be covered in greater detail in section 6.4.

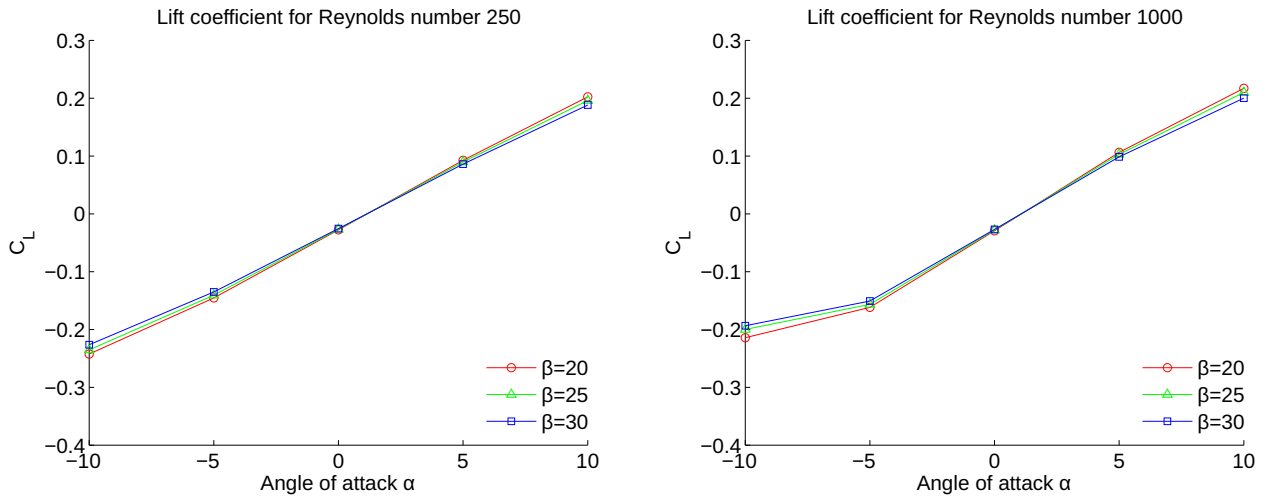


Figure 5.10: Total force in y-direction for Reynolds number 250 and 1000.

The lift coefficient, is roughly constant between the two Reynolds numbers. The main difference is that the forces at $\alpha = \pm 10$ for the different rudder rake angles diverge more than at lower Reynolds number, due to increasing importance of lift generated by pressure.

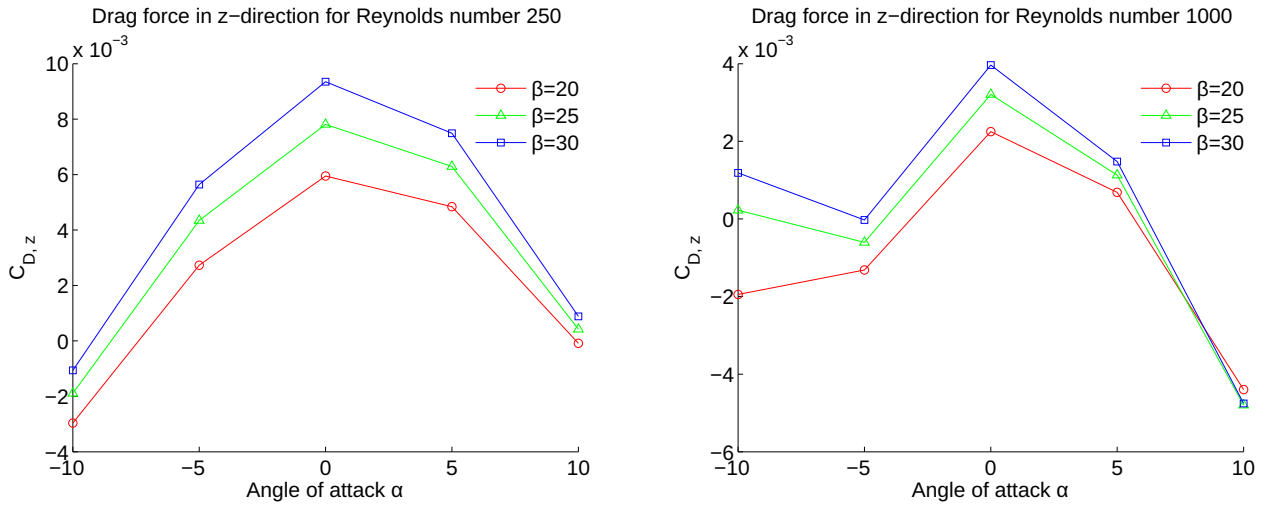


Figure 5.11: Total force in z-direction for Reynolds number 250 and 1000.

The total forces in z-direction are small in comparison with the drag and lift forces. This is advantageous in terms of rudder design, as the rudder will not try to force itself out of the water.

5.2.4 Total moments experienced by the rudder

The resulting moments have been calculated on the free surface. The origin was chosen as to be 1/3 of the cord from the leading edge of the cross section on the free surface, and calculated using a body-fixed coordinate system. This means that the moments will be measured at the same axis independent of the flow direction. The moments follow the same characteristics as the forces, having a reduction in pitch moment from increasing the Reynolds number. The roll and yaw moments are more stable between the two Reynolds numbers, with the same exception at $\alpha = -10$ degrees.

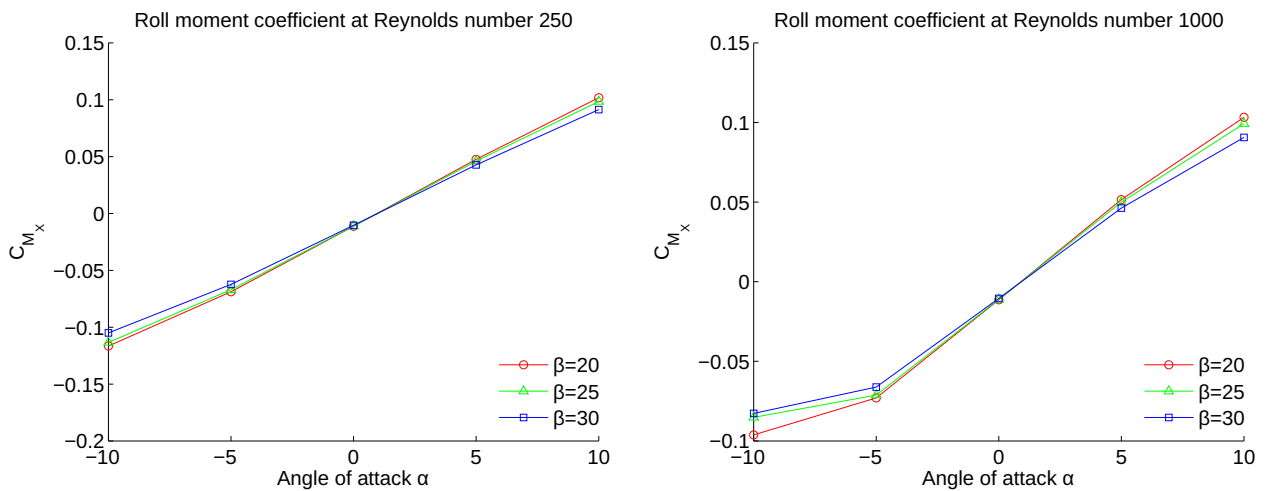


Figure 5.12: Roll moment on the free surface for Reynolds number 250 and 1000.

At both extreme angle of attacks the moments from the different rudder rake angles differ more at higher Reynolds number. This is mainly due to vortex shedding at $\alpha = -10$ degrees, and that the forces are pressure dominated at higher Re. The main contribution to the spread at $\alpha = \pm 10$ degrees are from the larger force variation in z-direction. This can further be explained by the definition of moment around the x-axis, ref. equation 2.5.7.

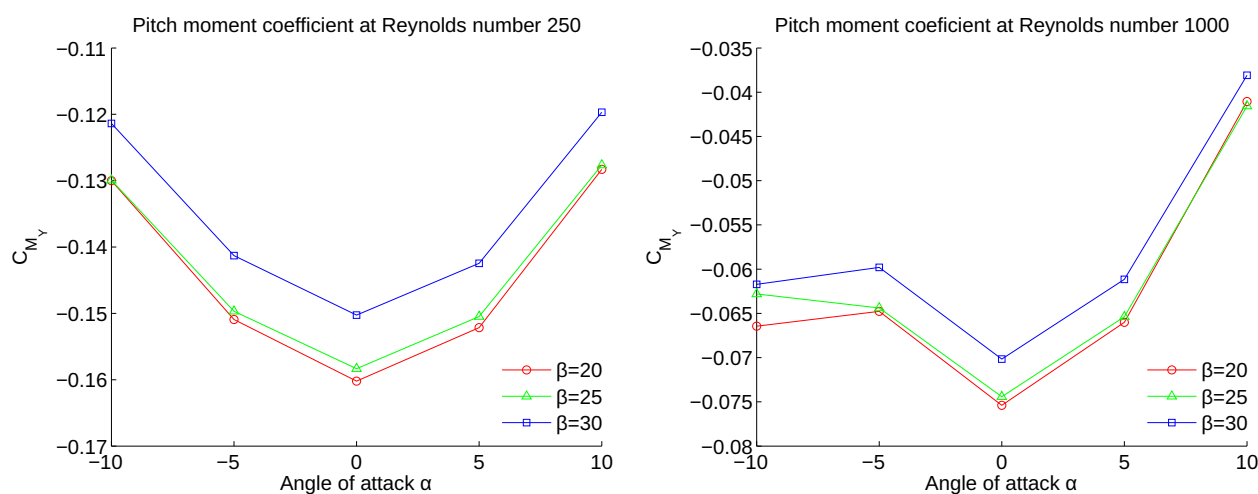


Figure 5.13: Pitch moment on the free surface for Reynolds number 250 and 1000.

The pitch moment is only dependent on forces in x and z-direction, both of which decrease with increasing Re. The result is an uniform reduction in the coefficient, with the major exception at $\alpha = -10$ due to vortex shedding.

The same increase in discrepancy is observed for the yaw moment on the free surface at Re=1000 as well.

The yaw moment is working against the rudder angle of attack, causing a restoring moment towards the neutral position. This is advantageous, as if the rudder were to suddenly be let free it would return to zero angle of attack. The restoring moment is not very large, but an opposite effect could be dangerous if the helmsman on the ship were incapacitated.

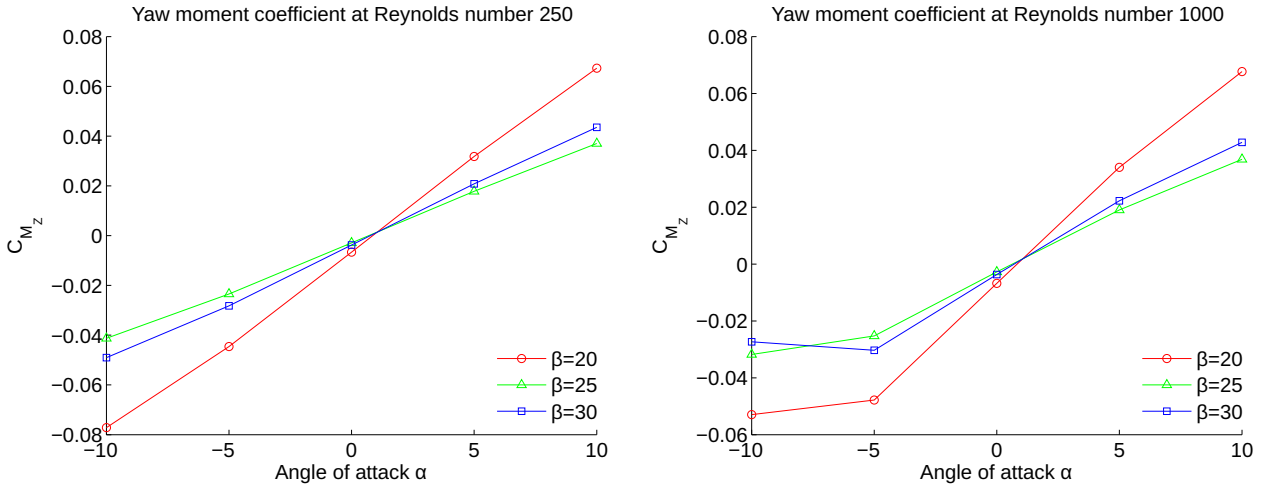


Figure 5.14: Yaw moment on the free surface for Reynolds number 250 and 1000.

5.2.5 Turbulent results

Turbulent simulations were performed for all rudder rake angles at $\alpha = \pm 10$ degrees only, due to limited time available, convergence problems and increased computational cost. Some of these issues are addressed in section 6.8.1.1 in chapter 6.

As the Reynolds number continue to increase, the total drag experienced by the rudder decreases. The relative importance of viscous drag are even lower than at $Re=1000$, as is expected. The pressure coefficient is comparable to the one at $Re=1000$, but in general slightly larger. This indicates that the rudder performs even better at higher velocities.

β	α	C_{D,V_x}	$C_{L,V}$	C_{D,V_z}	C_{D,P_x}	$C_{L,P}$	C_{D,P_z}
20	-10	0.0014	2.9×10^{-4}	3.8×10^{-4}	0.0807	-0.3542	-0.0073
	10	0.0036	-4.5×10^{-4}	-3.2×10^{-4}	0.0670	0.2503	0.0028
25	-10	0.0020	-3.2×10^{-4}	-3.3×10^{-4}	0.0713	-0.2658	6.1×10^{-4}
	10	0.0553	-4.3×10^{-4}	-6.0×10^{-4}	0.0553	0.2574	-0.0012
30	-10	00.0026	-3.8×10^{-4}	-8.0×10^{-4}	0.0755	-0.3323	-0.0014
	10	0.0025	-3.8×10^{-4}	-7.4×10^{-4}	0.0498	0.2535	-0.0015

Table 5.4: Pressure and viscous force coefficients at $Re=2.4 \times 10^6$.

As a consequence of the reduced viscous drag coefficient and the increased pressure coefficient, the total lift coefficient is increasing, whereas the total drag coefficient is decreasing at $\alpha \pm 10$ degrees. The lift coefficient for negative angles of attack are larger than for positive angles, contrary to what was experienced during sailing.

The pitch moment coefficient C_{M_y} is decreasing for the turbulent case, indicating that the rudder will remain more stable in z-direction. As previously mentioned, this indicates that the rudder will remain stable at the given rake angle.

The roll moment have increased, suggesting that it will be more difficult to hold the rudder steady along the y-axis. The yaw moment coefficient is fairly stable, indicating the same behaviour as on lower Re.

β	α	C_{D_x}	C_L	C_{D_z}	C_{M_x}	C_{M_y}	C_{M_z}
20	-10	0.0821	-0.3539	0.0077	-0.1493	-0.0221	-0.1171
	10	0.0705	0.2499	0.0025	0.1181	-0.0333	0.0752
25	-10	0.0733	-0.2655	0.0003	0.0969	-0.0302	-0.0694
	10	0.0586	0.2570	-0.0018	0.1129	-0.0023	0.0652
30	-10	0.0781	-0.3319	-0.0022	-0.1360	-0.0244	-0.0691
	10	0.0523	0.2531	-0.0022	0.1140	0.0005	0.0558

Table 5.5: Total force and moment coefficients at $Re=2.4 \times 10^6$.

Chapter 6

Discussion

In this section the consequences of the data presented in section 5 will be discussed. Additional discussions regarding issues encountered during this master thesis will also be covered.

6.1 Validation of the NACA0012 airfoil results

The 2D results were comparable against reference values, with smaller deviations. The 3D results deviated more, and were investigated as a process during the master thesis. The error were most likely found, but the limited time available meant that the problem could not be revisited.

Solver	Re	α	$C_{D,avg.}$	$C_{L,avg}$
MN1	500	0	0.1744	-1.5314×10^{-4}
CFL3D [Lockard et al., 2002]			0.1741	-5.38×10^{-6}
MN2	500	10	0.1324	0.4675
3DMN2			0.1452	0.3600
Multigrid[Mavriplis and Jameson, 1990]			0.1474	0.4469
pisoFoam	2000	0	0.08373	-2.7229×10^{-4}
RANS solver[Edmund, 2012]			0.08354	-

Table 6.1: Comparison of results for the NACA0012 airfoil.

The largest discrepancy is from the simulation at ten degree angle of attack. This is due to a limitation in Mega. The trailing edge on a foil will be difficult to model since it changes geometry rapidly at the $c/L=1$. Therefore this part had to be modelled by straight lines instead of curves. At zero angle of attack this won't have much influence

on the results, since most of the lift and drag are generated at the leading edge. This is true for when the foil has an angle of attack, but it will also have a uneven pressure distribution over the $c/L=0.5$ to 1. This pressure acting on the foil will add to both the lift and drag coefficient. The difference between the straight line and the real curvature is small, but it will still affect the results.

Another possible explanation is the domain configuration with two inlets and two outlets. On a rectangular domain it might cause some issues where the inlet and outlet boundary conditions coincide. This interaction upstream from the foil might affect the solution.

A much larger discrepancy is noted for the 3D foil and reference literature. Some of it might be explained by the possibilities outlined previously. The simulation were simplified as a stationary case, to save computational cost. The lift loss of 18.18 % is unlikely to be caused by this, since at this Reynolds number the flow past the rudder should not vary much with time. A likely cause for the lift loss is the small aspect ratio of $Asp=2$. At the end of the span the fluid will circulate,, resulting in a tip vortex. The effect of this are increased drag and loss of lift. By linear foil theory the loss of a foil with elliptical circulation distribution due to aspect ratio are given by the following relation [Steen, 2012]:

$$C_L = \frac{C_L^{2D}}{1 + \frac{2}{Asp}} \quad (6.1.1)$$

By this definition the loss of lift should be as much as 50 %. However, equation 6.1.1 are not accurate for low aspect ratio foils. The lift loss of low aspect ratio foils have been reasearched more in recent times due to the need of micro reconnaissance air vehicles. At $Re=8 \times 10^4$ the loss of lift from a flate plate wing with $Asp=1$ and $Asp=3$ when compared to 2D lift were approximately 25 % [Pelletier and Mueller, 2000]. This loss of lift will also induce a larger drag on the foil, which the increased drag coefficient when compared to 2D reflects. So a loss of lift of 18.18% due to downwash at the end of the span at this Reynolds number is not unreasonable.

6.2 Effect of unsymmetrical rudder design

The results presented in table 6.2 and 6.3 are the same as in chapter 5. But as the drag and lift coefficient were calculated for a limited number of angles of at $Re=2.4 \times 10^6$, it were deemed advantageous to present it in tabular forms as well.

Rudder rake angle β [deg.]	Angle of attack α [deg.]					
	-10	-5	0	5	10	
Re=250	20	0.1560	0.1391	0.1319	0.1344	0.1465
	25	0.1516	0.1354	0.1284	0.1309	0.1425
	30	0.1464	0.1309	0.1243	0.1267	0.1380
Re=1000	20	0.0921	0.0713	0.0638	0.0665	0.0786
	25	0.0868	0.0690	0.0618	0.0643	0.0760
	30	0.0835	0.0664	0.0595	0.0620	0.0733
Re= 2.4×10^6	20	0.0821				0.0705
	25	0.0733				0.0586
	30	0.0781				0.0523

Table 6.2: Mean drag coefficient at different Reynolds numbers.

The drag will decrease with increasing Reynolds number. This was to be expected when compared to forces acting on the rudder, and published data regarding the flow past a flat plate [Sabersky et al., 1998]. The resistance from turning the rudder to port (positive α) is lower than when turning it to starboard. The difference from $\alpha = -10$ to $\alpha = 10$ is an increase in resistance by 5.9% on average at $Re=250$. At higher Reynolds number this further increases to 13.1% and 22.4 % For $Re=1000$ and $Re= 2.4 \times 10^6$, respectively.

At zero angle of attack the lift is not zero, but working in the negative y-axis. As the rudder is mounted on the side of the hull, this lift force should be working in the opposite direction, to prevent drift due to the additional resistance of the rudder. The lift coefficient is quite small, so it will not cause a very large off-drift. But as the rudder design is unsymmetrical largely due to being mounted on the starboard side of the vessel, it would indicate that it is not working as intended. The general trend between $Re=250$ and $Re=1000$ indicates that this lift force will be similar at $Re= 2.4 \times 10^6$ as well. The larger cross section towards the free surface is the probable cause for this lift forc. It should be noted however that the proximity to the hull would affect these results substantially, so the combined system might actually work as it should. Additional analysis with a hll

model would confirm this.

The lift force behaves inverted at low Reynolds number, grating a larger lift at $\alpha = -10$ than 10 degrees. This difference is substantially larger than the increase in drag, as the lift is increased 16.7% and 18.8% on average at $Re=250$ and $Re=2.4 \times 10^6$. However due to periodic vortex shedding at $Re=100$, the trend reverses, as $\alpha=10$ generates 3.2% more lift than at $\alpha=-10$. But this is only at $Re=1000$, as in general the mean lift increases at negative angles of attack. This indicates that vortex shedding in itself is not the culprit as to loss of steering when the Vikingship turned to starboard. The effect of the unsymmetrical rudder design indicates that the rudder should have better steering power to starboard than port, contrary to what is experienced during saling.

Rudder rake angle β [deg.]		Angle of attack α [deg.]				
		-10	-5	0	5	10
Re=250	20	-0.2425	-0.1454	-0.0277	0.0926	0.2024
	25	-0.2352	-0.1406	-0.0268	0.0895	0.1959
	30	-0.2264	-0.1351	-0.0256	0.0860	0.1882
Re=1000	20	-0.2142	-0.1618	-0.0294	0.1063	0.2170
	25	-0.1999	-0.1566	-0.0280	0.1028	0.2099
	30	-0.1936	-0.1507	-0.0270	0.0986	0.2001
Re= 2.4×10^6	20	-0.3539				0.2499
	25	-0.2655				0.2570
	30	-0.3319				0.2531

Table 6.3: Mean lift coefficient at different Reynolds numbers.

6.3 Vorticity

The largest values of vorticity happens at the leading edge, due to the stagnation point and sudden transition from the front to the sides of the rudder. The next largest value are at the trailing edge, where the abrupt end of the rudder will give rise to a rotation of the fluid element, and thus vorticity. The vorticity generated from negative angles of attack is larger and more pronounced when comparing $\alpha = \pm 10$. This trend is continuous for the three flow regimes tested. Figure 6.1 displays the comparison for $\beta = 20$ degr. at $Re = 1000$.

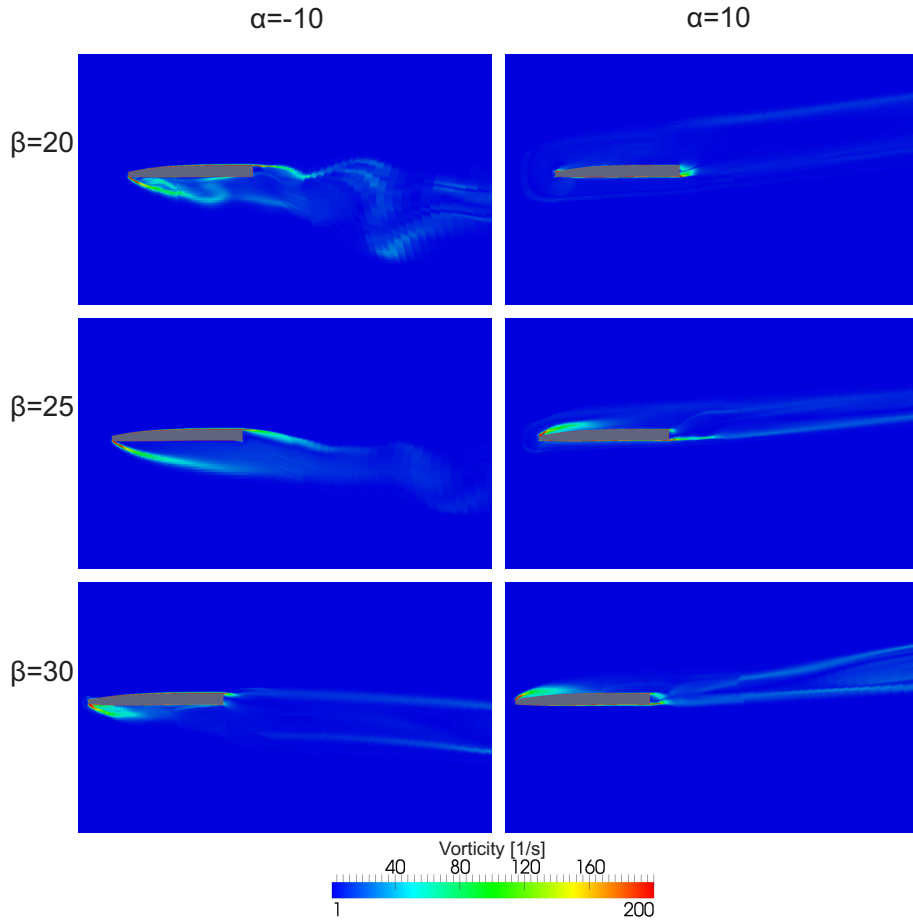


Figure 6.1: Vorticity at leading and trailing edge at $\beta=20$, $Re=1000$ and $|z/d|=0.6$.

Due to the unsymmetric design, the angular difference between the leading edge and the side are in general larger at the starboard side of the rudder than the port. This will induce more backflow, and consequently increasing the flow separation. Hence the vorticity is larger as well.

The largest values exist only locally. Smaller magnitudes of vorticity will exist far away from the body, and interact with the incident fluid field. This is the case behind the rudder, where rudder tip vortices happens as a consequence of vorticity and circulation. At the tip of the rudder there will be a fluid flow across starboard side to port, and vice versa depending on angle of attack. This happens because the flow past the rudder will have a larger velocity on one side relative to the other. This difference in velocity give rise to a pressure difference between the sides. Since the rudder tip is relative thin, fluid particles will be able to move from the high pressure zone to the low pressure zone. This circulation result in a vortex being continuously shed into the fluid. At low Reynolds number and positive angles of attack this system is stable, with small variations over time. For $\alpha=-10$, the wake is more disorganised. The tip vortex is generated, but encounters

another vortex with an opposite direction. This vortex is caused by flow separation, and will increase the drag experienced by the rudder.

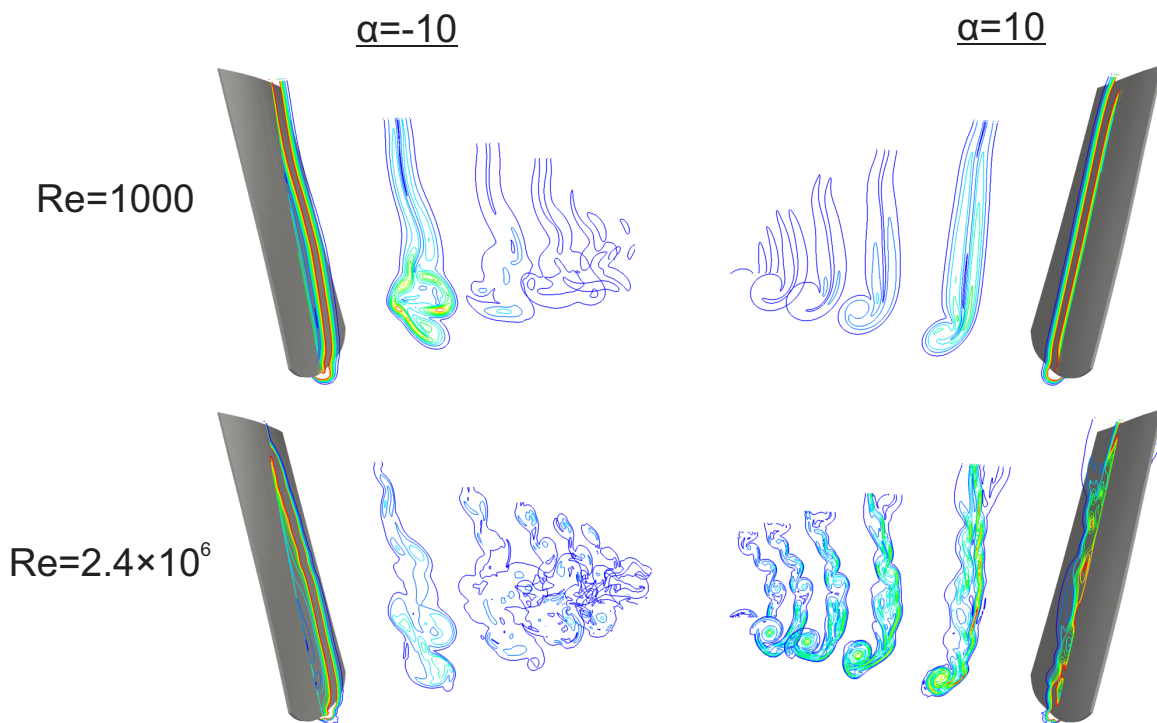


Figure 6.2: Vorticity around the rudder and into the wake for $\alpha=\pm 10$, $\beta=25$ for $Re=1000$ and $Re=2.4 \times 10^6$

The turbulent vorticity are more disorganised than at low Reynolds number. But the general trend is still the same. At positive angles of attack the tip vortex are generated at the end of the rudder and shed into the fluid. At negative *alpha* the vortex generated by flow separation are interacting with the tip vortex, causing the wake to be more turbulent. Figure 6.2 a display the vortex field around the rudder and downstream for $\alpha=\pm 10$ and $\beta=20$. Additional figures are attached in appendix 8.

6.4 Vortex shedding

The total lift coefficient are lower at angle of attack $\alpha= -10$ degrees than at $\alpha= 10$ degrees at $Re=1000$. The drag coefficient is also higher when the rudder is turning to starboard. Both of these incidents are due to vortex shedding due to unsymmetrical rudder design. These vortex shedding appear only at $\alpha= -10$ degrees. At positive angles of attack the flow past the rudder behaves in an orderly fashion, with a small vortex field just downstream from the trailing edge. A stable tip-vortex is generated at the end of the

span due to circulation over the tip of the rudder. These vortices and fluid flow past the rudder are stable, so the generated lift is stationary. At $\alpha = -10$ degrees the flow past the rudder behaves very differently. The flow is no longer stable, and the rudder experiences a varying lift and drag force due to vortices shed from the rudder. These vortices are periodically shed from the leading and trailing edge due to flow separation and backflow along the span. A complete time-series over a vortex shedding cycle are presented in figure 6.3.

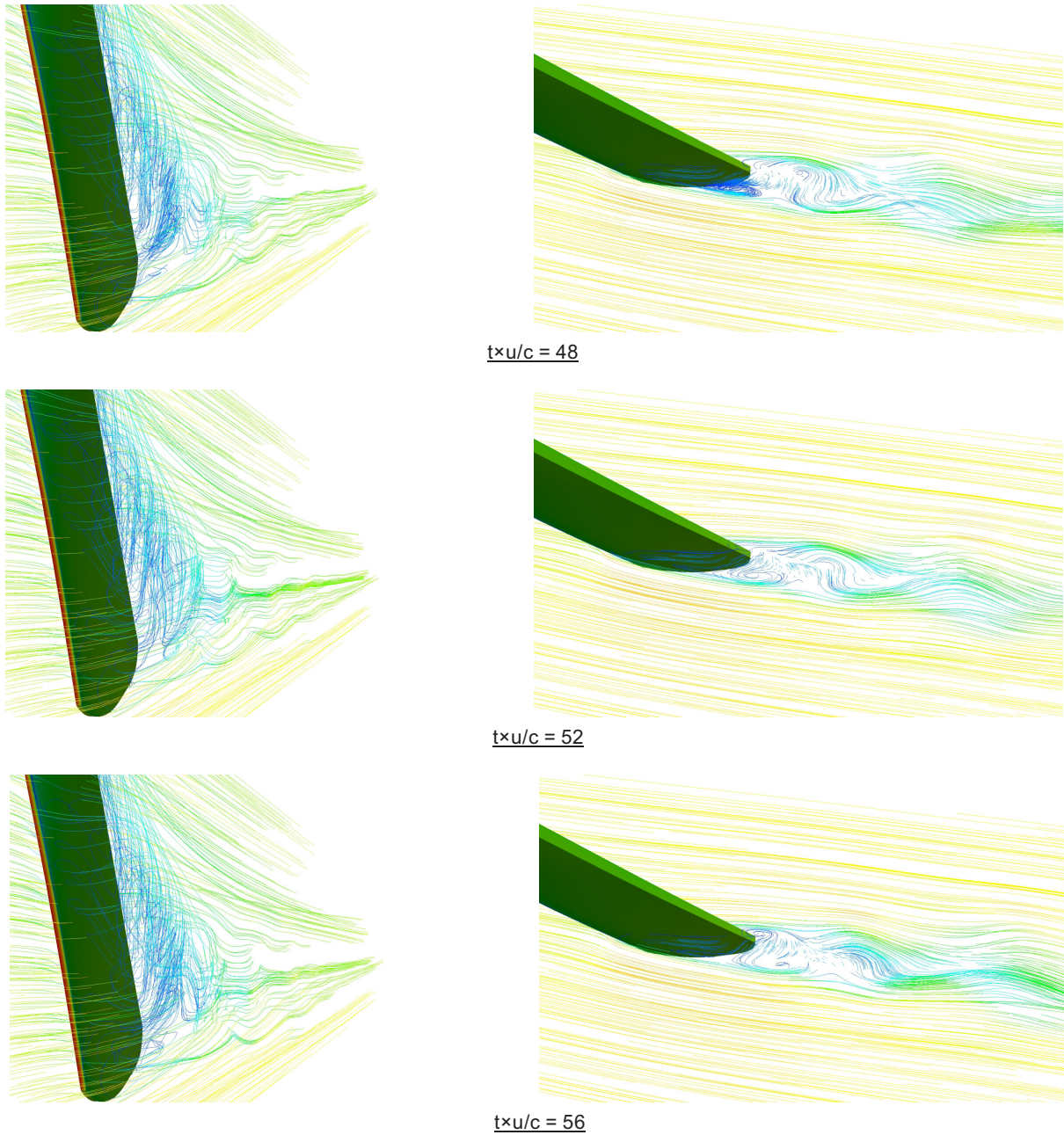


Figure is continued on next page.

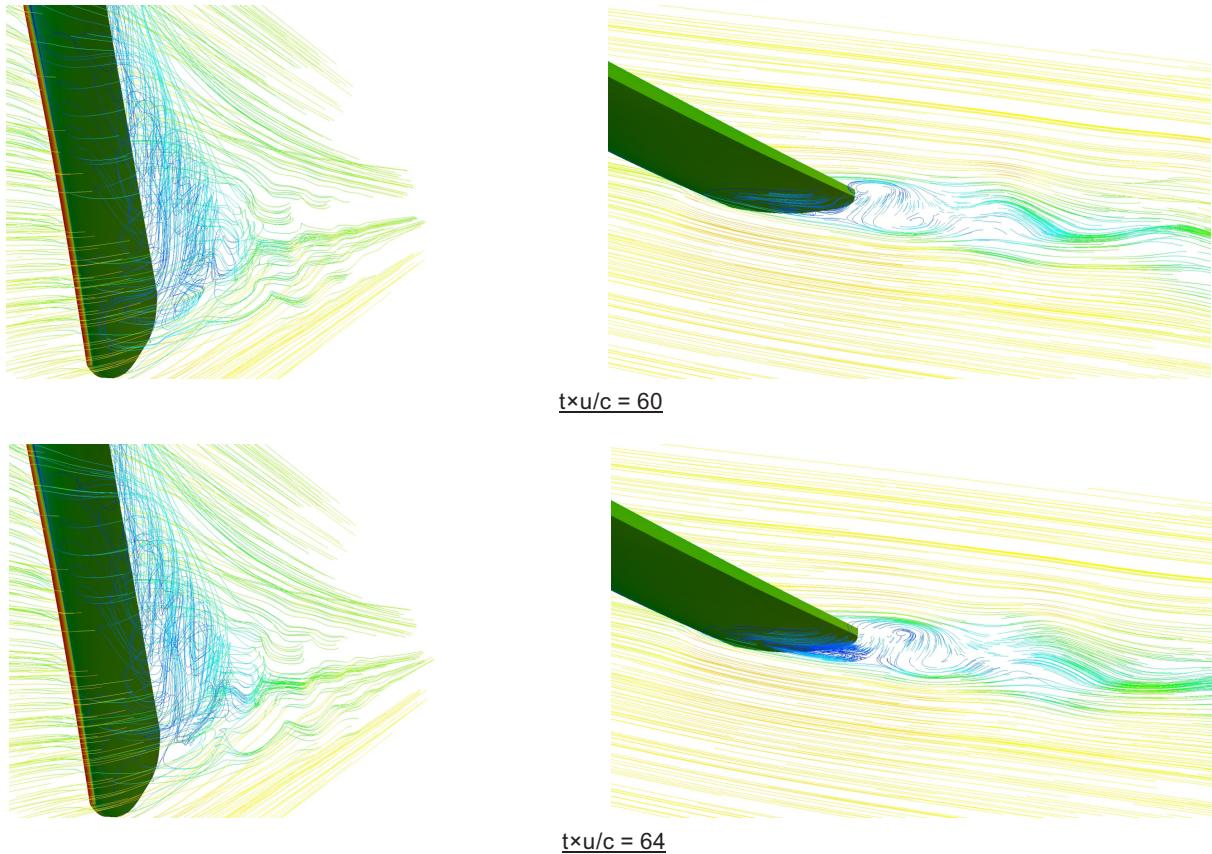


Figure 6.3: Streamlines at $Re= 1000$, $\beta= 25$ degrees and angle of attack $\alpha= -10$ degrees.

The main reason for this behaviour is the chamber of the cross-sections. On both sides of the rudder the curvature is positive relative to the y-axis. This means a gradually increasing thickness relative to the cord on the starboard side of the rudder, whereas on the port side the thickness is decreasing relative to the cord. When the flow is approaching with a positive angle of attack, it will not separate greatly on the transition from leading edge to the rudder surface. It will separate along the cord, due to the increasing curvature. This flow separation will re-attach itself on the trailing edge, as indicated in figure 6.4. When the incoming flow is approaching with a negative angle of attack, the flow will separate on the port side of the rudder. The positive curvature means that the angular transition of the geometry is much steeper on the port side of the cross-section than on the starboard side at the bottom third of the rudder. Combine this with the curvature, and flow separation will happen at large enough angles of attack.

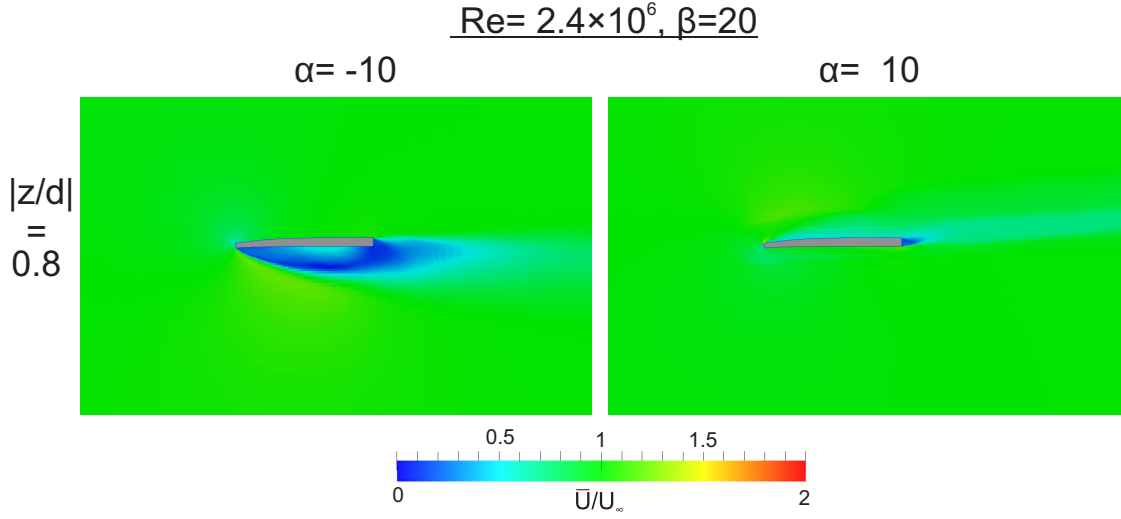


Figure 6.4: Velocity field for $\alpha=\pm 10$ at $Re=2.4\times 10^6$, $\beta=20$.

Due to the thickness reduction on the port side of the rudder, the flow will separate from the leading edge and generate a backflow along the surface. This backflow will cause a periodically vortex shedding from the leading and trailing edge. However, as the rudder rake angle is increased, the vortex shedding period is decreased. This can be seen from the Strouhal number. The frequencies of the oscillating lift coefficient have been found using discrete Fourier transformation. After filtering away the noise, the frequency with the highest occurrence were chosen.

Re	α	β	Strouhal number	C_{LSD}	C_{DSD}
1000	-10	20	0.5866	0.0034	4.8×10^{-4}
		25	0.5460	5.5×10^{-4}	9.8×10^{-5}
		30	0.1327	3.1×10^{-4}	6.1×10^{-5}
2.4×10^6	-10	20	0.5934	0.0074	8.2×10^{-4}
		25	0.7984	0.0059	7.7×10^{-4}
		30	0.2318	0.0016	9.2×10^{-5}
	10	20	0.0670	0.0013	1.5×10^{-4}
		25	0.1904	4.3×10^{-5}	8.1×10^{-6}
		30	0.1429	0.0012	1.5×10^{-4}

Table 6.4: Strouhal number and standard deviations for the Oseberg rudder

In general, the vortex shedding frequency is lower at higher rudder rake angles. This can be explained due to the change in cross-sections at different values of β . The cord

thickness will vary slower as β is increased. This will influence the rate of flow separation, as $\partial u/\partial y$ will be lower. Figure 6.5 illustrates the difference in cross-sections due to larger rudder rake angle. The geometry of the cross-sections at the same z/h will not be identical, due to the total wetted surface of the rudder being approximately constant between the three cases.

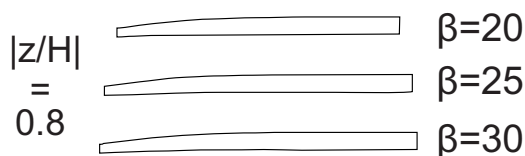


Figure 6.5: Cross-sections at $|z/H| = 0.8$ for the three rake angles.

The vortex shedding period and the relative large standard deviation at lower rake angles indicate that the effects on the foil will be a periodically oscillating lift force that may induce vibrations on the rudder. This strongly indicates that vortex shedding is causing the vibrations reported during sailing. To combat this, the rudder rake angle could be increased. Both the RMS of C_D and C_L are decreasing for larger rudder angles, meaning a reduction in force amplitude for these cases. Combined with increasing shedding period, and larger rudder rake angles lead to a more stable lift and drag force and will effectively prevent vibrations. Figure 6.7 displays the difference in flow characteristics at the trailing edge for $\beta= 20$ and $\beta= 30$ degrees.

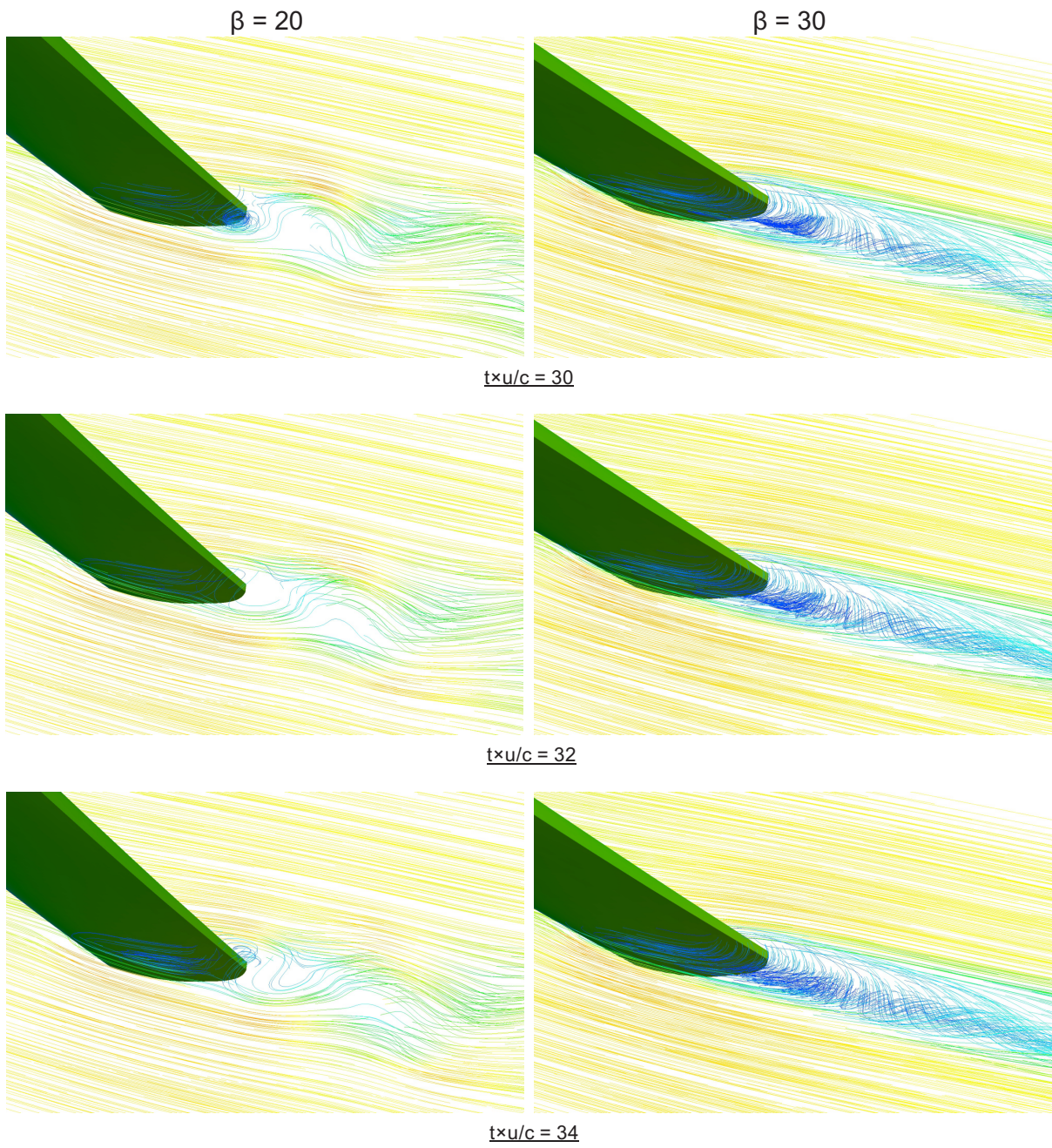


Figure 6.6: Figure is continued on next page.

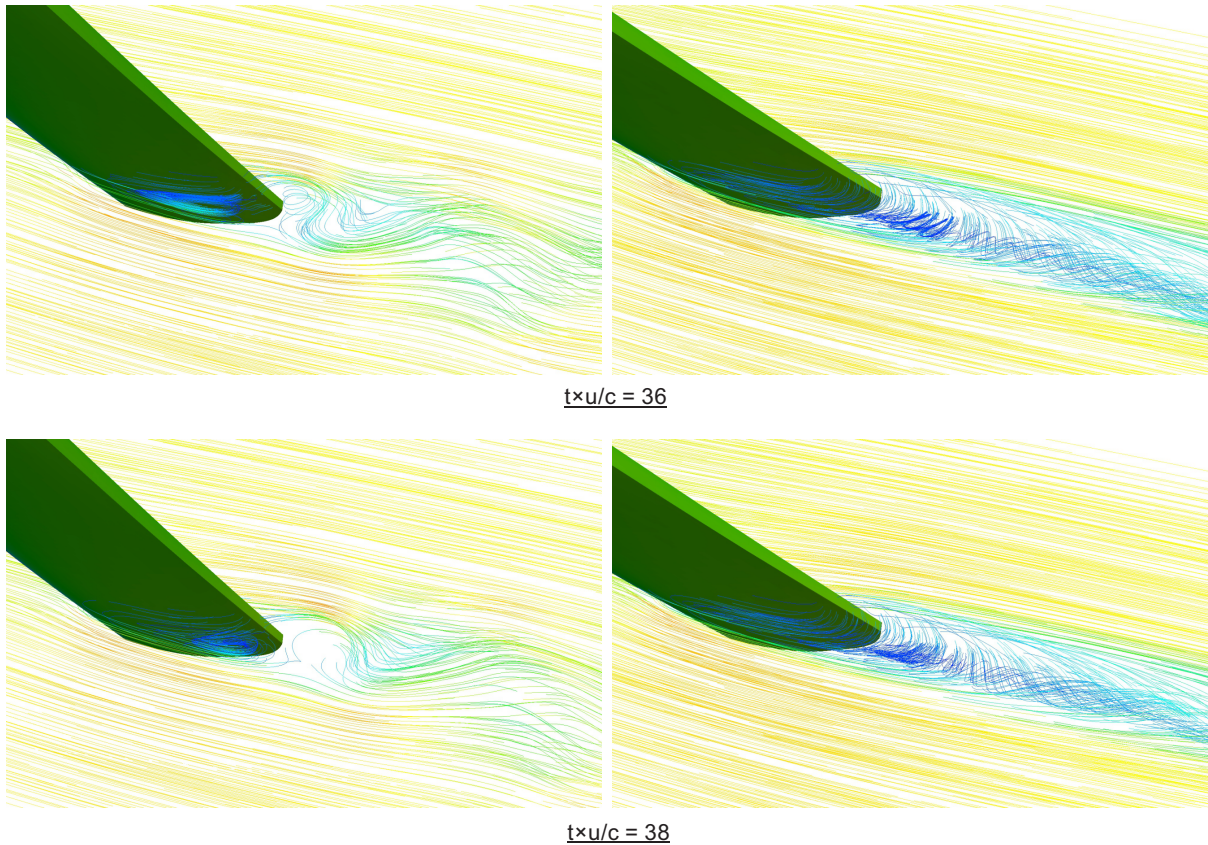


Figure 6.7: Streamlines at $Re= 1000$, angle of attack $\alpha= -10$ degrees, $\beta= 20$ and 30 degrees.

At turbulent Reynolds number the flow will re-attach itself to the rudder more easily than at a lower flow regime, due to a larger suction pressure zone at the leading edge. For $\beta= 20$ and $\alpha= -10$ there are vortices being shed into the fluid at several locations along the foil. For the larger rudder rake angles the flow no longer generates vortices. Instead, the flow separates at the leading edge, and re-attach itself at the trailing edge. The re-attached flow is not stable, and the re-attachment point will vary. For $\alpha= 10$ the flow past the leading edge separates very little or not at all. The re-attachment point is close to the leading edge and does not vary with time.

To illustrate the behaviour of vortex shedding, the Q-criterion are being used. It is a criterion for identifying coherent vortex structures [Jeong and Hussain, 1995]. The values of Q used in the illustration are 5 and 8 for $Re=1000$ and $Re=2.4 \times 10^6$, respectively.

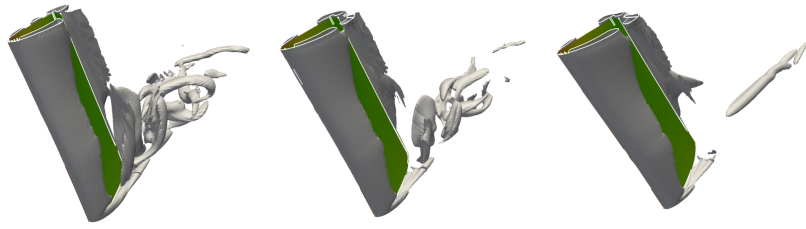


Figure 6.8: Q-criterion for $Re=1000$, $\alpha=-10$.

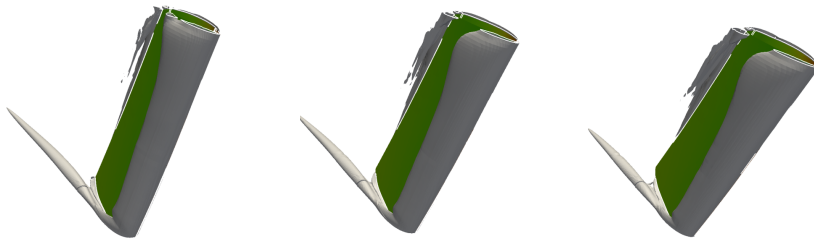


Figure 6.9: Q-criterion for $Re=1000$, $\alpha=10$.

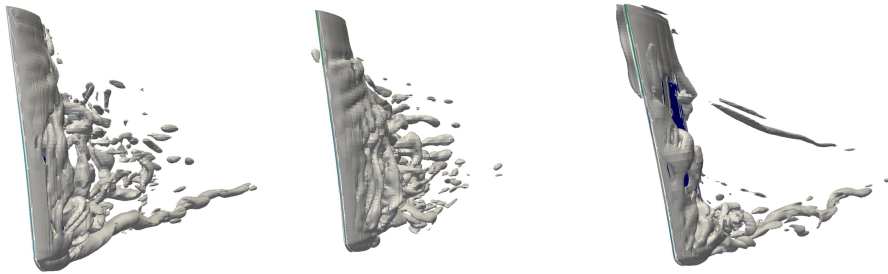


Figure 6.10: Q-criterion for $Re=2.4 \times 10^6$, $\alpha=-10$.

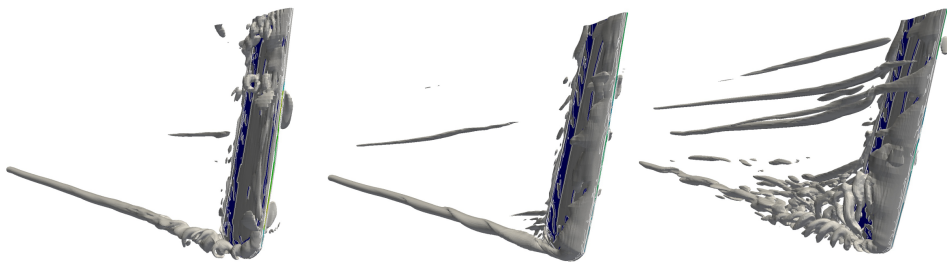


Figure 6.11: Q-criterion for $Re=2.4 \times 10^6$, $\alpha=10$.

6.5 Pressure distribution

The pressure distribution over the rudder is interesting as it indicates how the fluid flow around the rudder behaves. The maximum and minimum pressure is located along the leading edge, due to the presence of stagnation points here. The pressure distribution at $Re = 250$ is largely symmetrical, but negative α in general generates larger lift and drag forces. The pressure distribution for $Re = 250$ is presented in Appendix 1.

For $Re = 1000$ the pressure distributions are fairly similar for zero and intermediate angles of attack. On the port side of the rudder the minimum pressure at the free surface will move towards the trailing edge as α increases. The minimum pressure centre will move closer to the leading edge at higher β , resulting in moving off the port side at $\beta = 30$. The positive pressure will gradually move downward the span at the same interval.

On the starboard side the zero pressure centre moves towards the trailing edge and the tip of the rudder. The negative pressure centre will gradually move from the front of the rudder to the starboard side and further towards the trailing edge.

At zero angle of attack the rudder has a varied transition of pressure on the port face. Due to the smoother transition from front face to port side towards the free surface, a positive pressure centre will exist near the leading edge. Since the flow has to cover a larger distance over the cross-section, a negative pressure exists before the trailing edge. This negative pressure will gradually move forward along the span to the leading edge due to the slight curvature of the rudder. The flow will separate due to this curvature, and re-attach itself along the cord. At the opposite side this curvature gives rise to a positive pressure along the span. The slight camber towards the tip of the rudder results in a larger velocity on the starboard side, thus creating a lower pressure region here. At the port side the same camber creates a positive pressure.

For negative angles of attack the positive pressure near the tip of the rudder will be moved forward as α decreases. This is due to more flow separation, and the resulting vortex shedding. At the same interval the negative pressure near the leading edge will increase, resulting in a smaller positive pressure region near the free surface. On the starboard side the positive pressure continues to grow due to the increasing negative inflow angle.

At all angles of attack there can be seen a pressure zone near the tip of the rudder. The fluid will flow from the area with high pressure to the area with low pressure, resulting

in a zone on both sides due to the circulation from port to starboard side, or opposite.

The development of pressure zones as a function of α and β can be seen in figure 6.12 to 6.14.

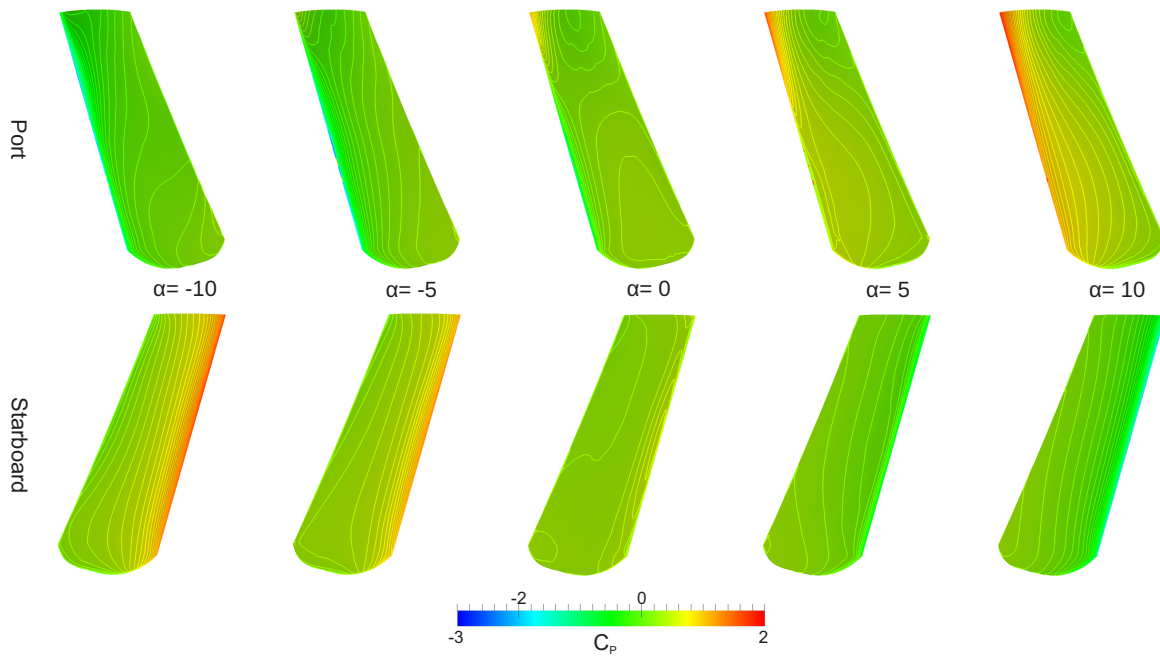


Figure 6.12: Pressure contours on rudder surface for $Re=1000$, $\beta=20$.

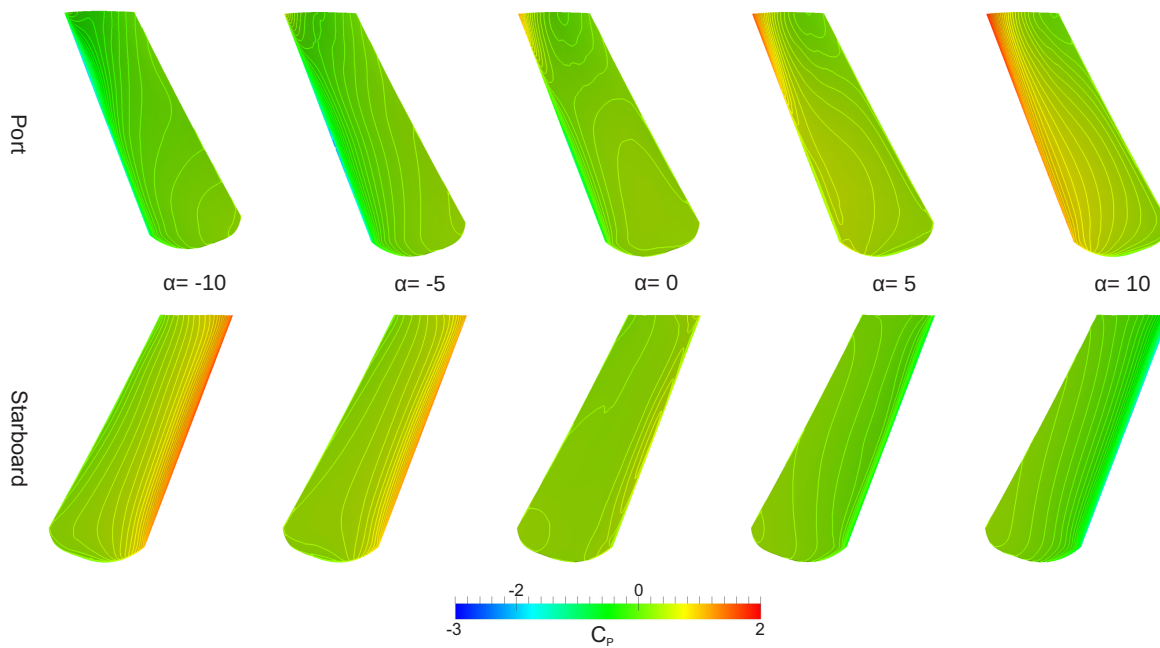


Figure 6.13: Pressure contours on rudder surface for $Re=1000$, $\beta=25$.

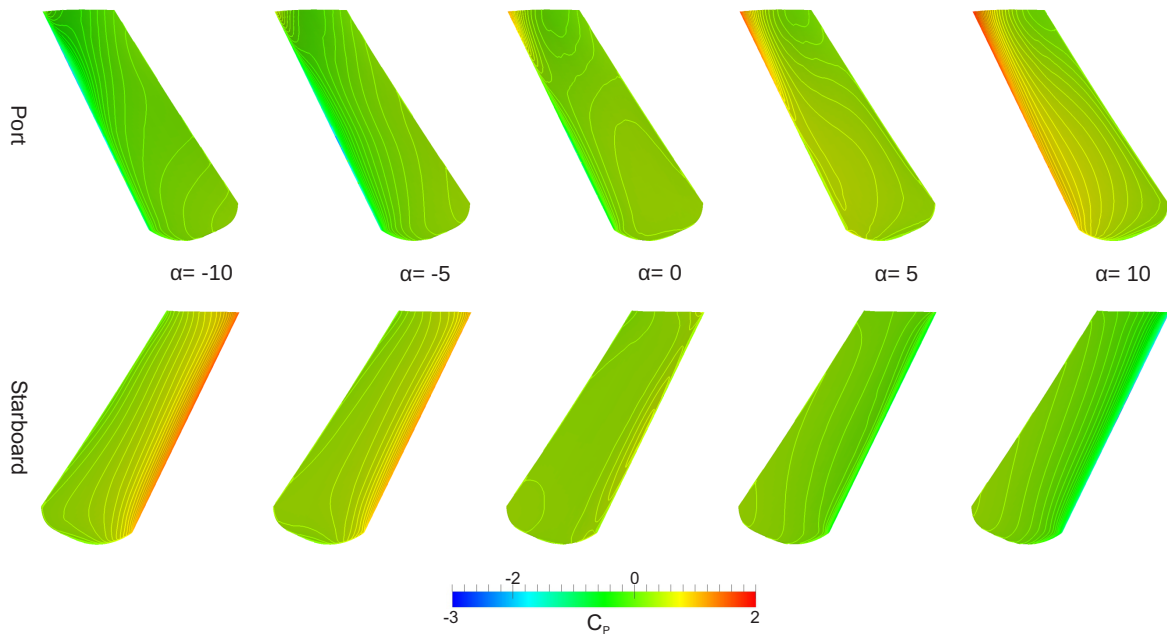


Figure 6.14: Pressure contours on rudder surface for $Re=1000$, $\beta=30$.

The difference between the rudder rake angles are mainly that some pressure fields will be larger or smaller due to the change in geometry caused by changing the rake angle. There are not any huge differences, but enough to create a more stable vortex shedding or more lift.

The pressure distributions at turbulent Reynolds number are fairly similar as far as the positive pressure zones are concerned. As this flow regime is fluctuating more, the mean pressure coefficient have been presented. At the positive zones the same general development with increasing rake angle is observed. The only difference are local high pressure zones as a consequence of smaller vortex formations at the leading edge. For $\alpha=10$ and $\beta=20$ the pressure difference at the tip of the rudder is larger, creating a much earlier tip vortex. As β increases this vortex generation is further from the leading edge. Simultaneously, a negative pressure centre is moving upwards along the foil, resulting in a backflow at $\beta=30$ and consequently flow separation. For $\alpha=-10$ the flow separates immediately at the leading edge. The negative pressure centres confirms this behaviour. The flow re-attaches itself at the trailing edge. As the rake increases, the resulting sloer change in chamber line creates a more stable pressure gradient due to lower $\partial u \partial y$. As such, the pressure zones are more slowly varying across the port side of the rudder. The consequence is that the flow separates very little at $\beta=30$.

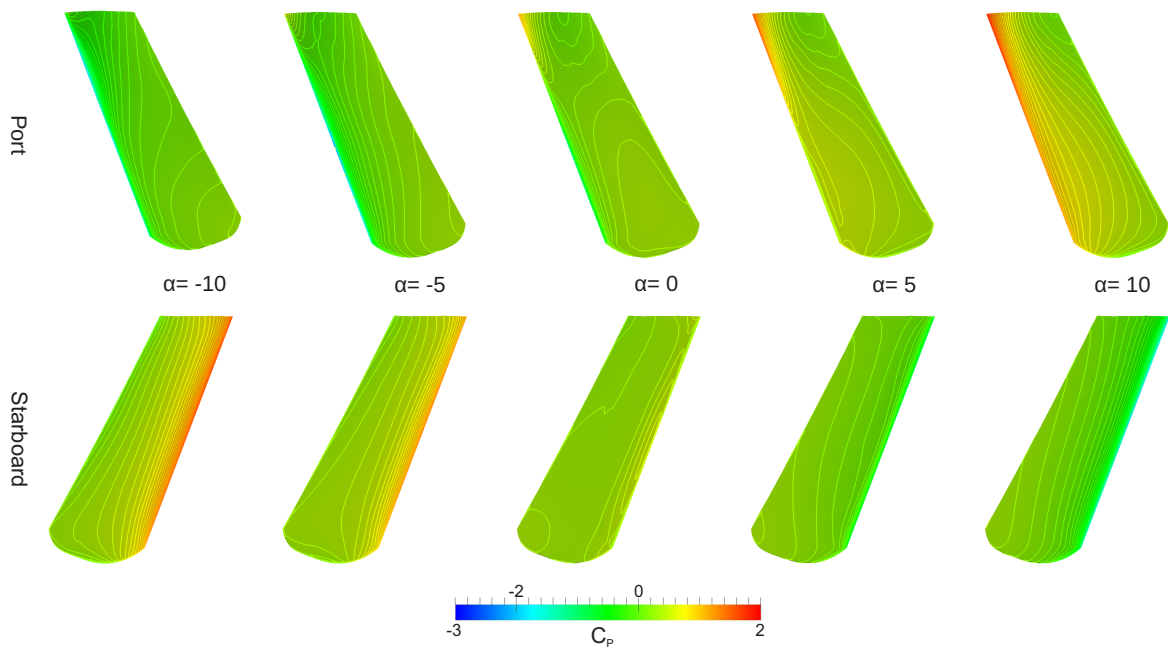


Figure 6.15: Pressure contours on rudder surface for $Re=2.4 \times 10^6$, $\alpha=10$.

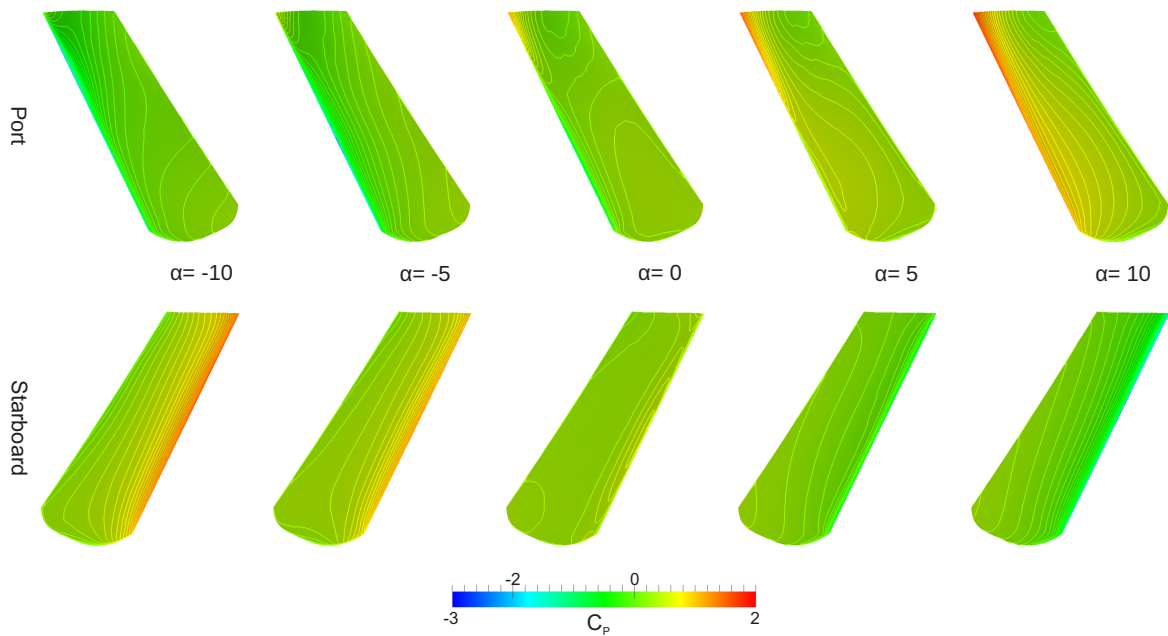


Figure 6.16: Pressure contours on rudder surface for $Re=2.4 \times 10^6$, $\alpha=-10$.

6.6 Ventilation

At low Reynolds number the risk of the rudder ventilation are low, and the effect of ventilation insignificant. The rudder will not generate a pressure low enough as to

ventilate more than a few centimetres at the free surface. As Reynolds number increases, the risk of ventilation and the consequence of it increases. Figure 6.17 display the lowest point where ventilation might occur, as a percentage of the total draft. For negative angles the ventilation length increases with β this indicates that a much larger percentage of the lift is generated by suction pressure than for positive angles.

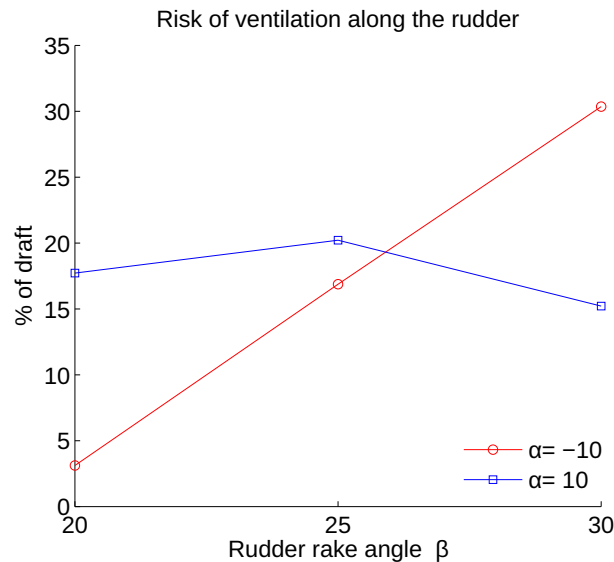


Figure 6.17: Risk of ventilation at $Re=2.4 \times 10^6$.

The maximum consequence of ventilation appears fairly constant for $\alpha=10$ degrees, with an maximum ventilation length of 20.21% of the draft. For $\alpha=-10$ the consequence are more dramatic. As the rudder rake angle increases, the risk of ventilation increases in an almost linear fashion. Although much lower at $\beta=20$ degrees, at higher angles this could indicate one cause of the loss of steering power when turning to starboard.

6.7 Suggested improvements

The most unique characteristic of the Oseberg rudder are the unsymmetrical design. In this study several drawbacks when the rudder is encountering a flow with a negative angle of attack. Studying the vorticity reveals that flow separation are due to the abrupt transition from leading edge to the side. Plots of the shear stress confirms this behaviour. Flow separation happens on both positive and negative maxima of angle of attack. To reduce this effect, the rudder should be more streamlined at the leading edge. As it is difficult to recreate such a sharp transition using traditional tools, the edge are most likely bevelled already. Increasing this further should prove advantageous to prevent flow separation. The trailing edge does not appear to cause any major disturbances, hence leaving it unaltered is not an issue. At zero angle of attack the rudder generated a lift

force that would turn the ship to port, contrary to

Another issue were vortex shedding at $\alpha=-10$ degrees at higher Reynolds number. At $Re=1000$ the vortices are shed near the tip of the rudder. At $Re=2.4\times 10^6$ it happens at more arbitrary locations, due to increased 3D-effects as a consequence of turbulence. In both flow regimes this phenomenon are connected to the chamber of the rudder at port side, as well as the slight curve along the span.

The lift for negative angles of attack are in most cases larger than at positive angles. This is contrary to what was experienced during sailing. The pressure coefficient and flow separation can explain this discrepancy, and might lead to loss of lift when the ship is turning towards starboard. The geometry can be modified to prevent these effects from happening. Firstly, by moving the suction fields towards the tip of the rudder will ensure better ventilation characteristics. By straightening the chamber and making the rudder more symmetric about the x-axis would prevent flow separation from happening.

These suggestions are under the presumption that rudder-hull effect are not the cause of loss of steering power, which is entirely possible.

6.8 Limitations of the model

There are several simplifications and effects that are neglected in this thesis. The most pronounced one are the simplification of the free surface. In this thesis it is imply modelled by the double-body approximation, e.g the flow behaves as if there was a mirrored version of the domain above the free surface. This fulfils the requirement of no flux through the surface and over the top of the rudder. As a consequence, no free surface waves are being generated. However, the rudder is a fairly slender structure, and will not generate a substantial amount of surface waves. The impact of this simplification will not be too drastic. However, ventilation are connected with free surface interaction. In this thesis an estimate of the risk and consequence of ventilation has been performed by examining the pressure on the rudder surface, With a correctly modelled free surface and air domain, the loss of lift due to ventilation can be properly documented.

The effect of hydrostatic pressure and gravity are not included. The effect of static pressure are minimal due to the limited draft by the rudder, and will affect the result uniformly. It is therefore neglected, since it is difficult to implement it properly into OpenFOAM.

For the turbulent results there are certain limitations with the k- ϵ model that might impair the solution. The model are not accurate when predicting boundary layer flow with large adverse pressure gradients, large flow separation and re-attachment [White and Corfield, 1991]. While this is not an issue for positive angles of attack, the negative angles experienced large flow separation and periodically re-attachment. There there is a degree of uncertainty attached to the results obtained at $\alpha=-10$ degrees. Running an analysis at $\alpha=-5$ degrees could indicate the validity of results obtained at larger angles of attack, as the flow will not separate as much.

It wasn't performed a mesh convergence analysis with the turbulent results due to instability problems in the turbulence simulations. Therefore there are some uncertainty to the accuracy of the results. Furthermore, there was some values of y^+ that are outside the alidity of the log-law of the wall. Most of these values were located at the side of the rudder, so they should have little impact on the results. But some were located at the leading and trailing edge. Albeit a very limited number of faces had values outside the range, it might impair the solution to a certain degree. The values were corrected as far as time allowed it, but the geometry of the rudder made it difficult to do so.

6.8.1 Issues encountered during this thesis

There were some problems encountered during the work with the Oseberg rudder. This section is dedicated to the explanation of these, the cause of them and what might be done to avoid them in the future. It is the intention of the author that the documentation of these issues might be of service to others with similar work in the future.

6.8.1.1 Turbulence simulations and stability

There were stability problems when performing turbulent simulations. The instabilities occurred for all angles of attack, so a critical flow separation was not the problem. Although a rigorous troubleshooting were performed, a clear cause for the simulation crashes were not found.

The crashes happened in conjunction with the k- ϵ turbulence model. Running the same simulations without enabling turbulence resulted in a stable simulation, with convergence of forces and reasonable results. Starting the same simulation with turbulence enabled caused the residuals to converge at first, then to suddenly rise sharply. This resulted in a high Courant number and consequently simulation termination. In some cases

the simulation continued after the initial spike in residuals, but growing periodically instabilities caused the simulation to be increasingly unstable, causing it to crash. The direct cause of the instability are large positive and negative values of ϵ and a corresponding rise in the residual.

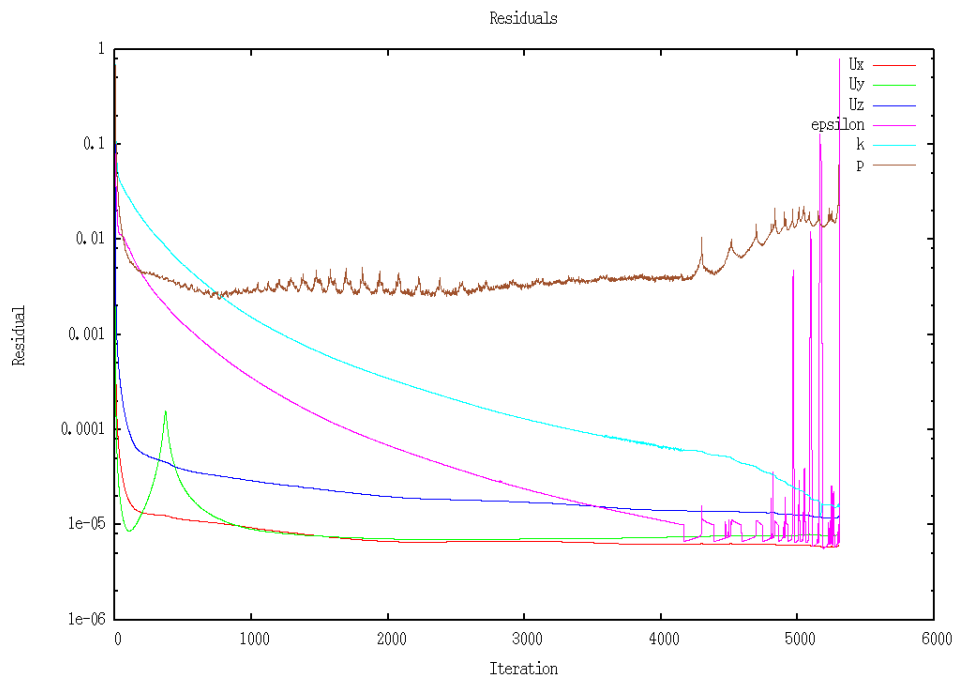


Figure 6.18: Plot over residuals until critical instability

Reducing the maximum Courant number to 0.1 did not increase stability, as Δt were only approaching zero instead, resulting in so small time that the simulation accuracy could not monitor such small difference in time steps. The result were that OpenFOAM crashed due to insufficient accuracy. This indicated that it were not an issue with the Courant number in itself that caused the instability, but something else.

Investigating where the instabilities occurred revealed that the high values of Co were located along the leading edge, just before the transition into the tip of the rudder. This is also the area where the cells with the highest value of non-orthogonal faces are located, due to the rapid transition in geometry. The value of the non-orthogonality was 69 degrees, within openFOAM's criteria for an OK mesh. A working theory was then that these faces caused the instability. The faces in this area were corrected as much as the geometry and grid shape allowed, reducing the maximum value to 62 degrees. The instability still occurred. Another mesh of polyhedra were generated in STAR-CCSM+. The first mesh had a maximum value of 64 degrees, and ran without problems. The resulting y^+ values were too high, so a finer mesh was made. This mesh had a lower value of non-orthogonality, of 62 degrees. However, the turbulent simulation became

unstable and crashed. A structured mesh from Mega was then used anew, with additional correction for non-orthogonality. The following values were modified in the *"fvSchemes"* directory:

- `laplacianSchemes`: Gauss linear corrected to Gauss linear limited 0.333.
- `snGradSchemes`: Corrected to limited 0.333.

The limited scheme of 0.333 applies a non-orthogonal correction that is less or equal to half the degree of non-orthogonality. The laminar results converged smoothly with these schemes, so it were applied to those simulations as well to get comparable results. The effect of using a different scheme were documented by performing the same simulation on a NACA0012 airfoil at $Re=500$.

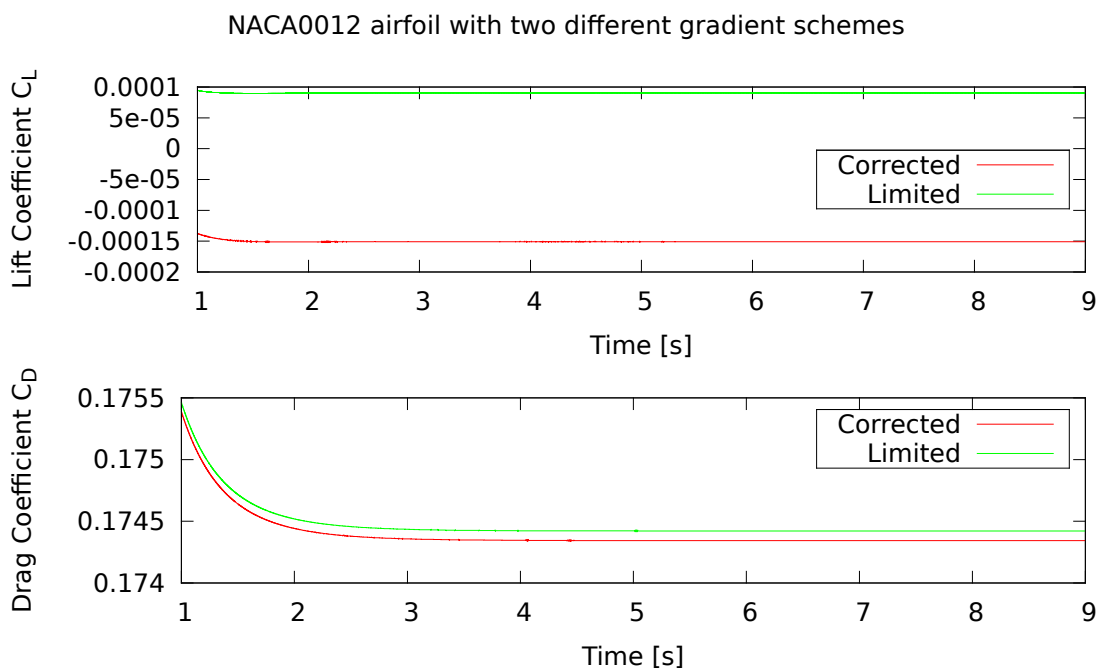


Figure 6.19: NACA0012 airfoil at $Re=500$, $\alpha=0$ with a corrected and limited solution scheme.

The drag coefficient are almost identical, 0.174421 for the limited scheme and 0.174343 for the corrected one. The lift coefficients diverge more, but both are practically zero. In terms of results in the 3D simulation this would have little influence on the resulting forces. The turbulent simulations were still unstable using this scheme, but it were stable for a longer period than with the *corrected* scheme.

Another possibility was that the $k-\epsilon$ model itself were unsuited for the flow regime. The

model is sensitive to flows that are not fully turbulent. As the Reynolds number was sufficiently high, at $Re=2.4 \times 10^6$, this was not the case. The next possibility was that the initial conditions for both k and ϵ were too low. The turbulent intensity was increased, with no tangible improvement in stability.

A stable initial solution were found by running the turbulent simulation without using the $k-\epsilon$ model initially. There were no problems with stability at this configuration. When the residuals had started to converge, the turbulent model were enabled. This approach led to a stable simulation, indicating that the problem lies in the start-up phase with the $k-\epsilon$ model.

6.8.1.2 Mesh

The mesh was created using Mega. This would prove later one to be an ineffective meshing software later in the semester. Mega supports .STL-files and can import them and export them successfully. To create a line on the surface of the object of interest one has to specify two points on the geometry and create a line between them. Mega has the option to fit this line to the surface. However, after successfully creating a complete mesh, the shortcomings in Mega revealed itself. The source cod for line generation is configured as to search for a point on the STL-surface for each incrementation along a line. When this is found, Mega will continue to the next line increment. This process repeats itself until a fit has been found for the line. If the last increment becomes too short or too long, Mega will start the iteration again. This process works well for a smooth geometry, but for this thesis's geometry it proved unsuitable. The nodes Mega searches for line generation is the centroid of the triangular elements in a STL surface. The Oseberg rudder has sharp edges on every transition between the sides. Mega will then be confused by two possible nodes when generating lines along these edges. This in turn resulted in a difficult fit, one which got worse as smaller increments were specified along these lines. This problem didn't impede with the mesh configuring until quite late in the semester, which meant that there was not time to learn and generate a new mesh in a different software. If this thesis was to be performed again, or a similar study, Mega would not be recommended as a mesh generator.

There were several potential issues regarding the geometry itself other than sharp edges. The trailing edge is thinner than the trailing edge, and the difference substantially increases as the draft decreases, as illustrated in figure 6.20.

Using a structured mesh forces the number of elements along a line to be the same regardless of line length. The difference in thickness close to the surface and the end of

the span resulted in a compromise. The mesh was deemed fine enough at the bottom and not too coarse at the surface. The same principle also affected the leading edge and trailing edge, as the front thickness always are smaller than in the rear of the rudder. A structured mesh is easier to work with in terms of user input and the logical nature of this method, but in this case the flexibility of an unstructured mesh might be better suited, both in terms of representing an uniform boundary layer around the rudder and less computational cost since the required cells for a complete mesh will generally be smaller. A structured mesh will generally give better results than an unstructured one however [Moraes et al., 2013]

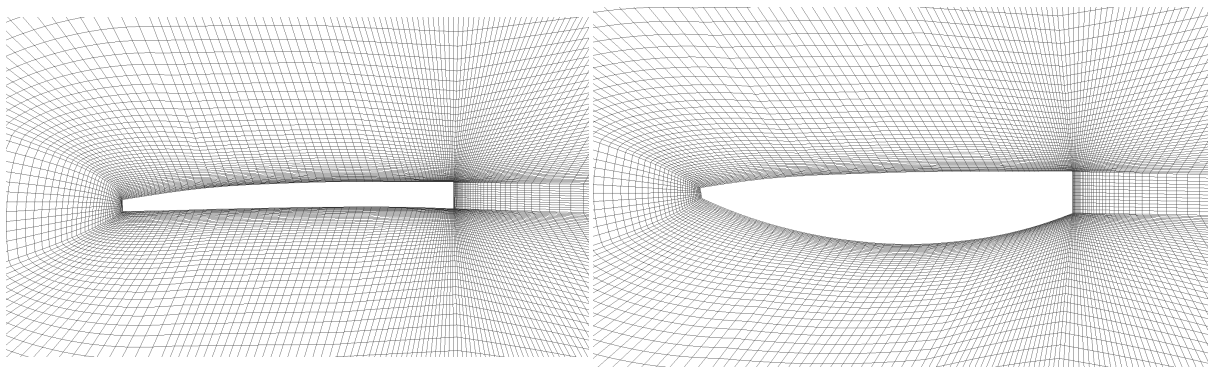


Figure 6.20: Different thickness ratio along the rudder proved a challenge when using structured mesh.

Chapter 7

Conclusion

An modified version of the rudder found at the excavation site of the Oseberg ship has been studied in multiple conditions. The rudder rake angle β has been studied at 20, 25 and 30 degrees and the angle of attack α has been varied from -10 to 10 degrees. Three Reynolds numbers were chosen, 250, 1000 and 2.4×10^6 . The first two ran with a laminar simulation. The latter was sufficiently turbulent to be implemented with the k- ϵ turbulence model.

For Reynolds number 250 the flow past the rudder were stable. Due to the unsymmetrical rudder design, there was a small lift generated at zero angle of attack. At positive and negative maxima of α the total lift and drag generated were not identical. At this Reynolds number it is attributed to the rudder design. As the Reynolds number is increased to 1000, the viscous forces are less important relative to the pressure forces. In this flow regime the flow past the leading edge will separate at $\alpha = -10$ degrees. The increasingly negative chamber along the span of the foil will create an adverse pressure gradient at the leading edge, resulting in a backflow and critical flow separation. There will be an gradually vortex build-up along the side of the rudder and at the trailing edge. These vortices are periodically shed into the fluid, generating a varying lift force. The same effect are observed at $Re = 2.4 \times 10^6$ as well, but with more 3D effects. For positive angles of attack limited flow separation is occurring at the leading edge, resulting in a stable lift force. This flow separation is causing the vibrations experienced during sailing. It was found that increasing the rudder rake angle proved advantageous to prevent vibrations. The standard deviation of C_L decreased and the vortex shedding period increased, resulting in a more stable lift force, as β increased.

The vortex shedding does not explain the loss of steering force at negative angles of attack, which happened during sailing of the replica [Godal, 2014]. The mean lift coefficient

for negative angles are in general higher than for positive, directly opposite of what is experienced in reality. The most likely culprit for the loss of lift are ventilation and/or proximity to the hull. The free surface is approximated in this thesis, so the real effect of ventilation can not be studied. However, there are indications that the risk of ventilation at $\alpha=-10$ degrees is increasing with rudder rake angles. For $\alpha=10$ the risk is fairly constant. Moreover, as the rudder is turning, the effective angle of attack will increase. Combined with the possibility of an increased turbulent flow due to the hull crossing over into the incident velocity, and the lift generated by the rudder at negative α might decrease substantially.

Chapter 8

Recommendations for further work

As an CFD simulation on a Viking ship rudder has not been performed before, there are several concepts that might be interesting to investigate further.

The Oseberg rudder have been investigated under multiple conditions, but not all were completed. At $Re=2.4 \times 10^6$ only the largest angle of attack were examined. Intermediate angles would reveal if the flow separates earlier than at $Re=1000$. The current model could also be expanded with a more realistic treatment of the free surface, to investigate the effect of ventilation on the rudder

The Oseberg rudder is not a complete system, but an integral part of a Viking ship. The presence of a hull might impose additional effects of the rudder. A simplified model could be developed to check the hull-rudder interaction. This could be done by moving the right side of the fluid domain closer to the rudder and implement the rear part of the Oseberg hip hull where appropriate. Selecting the hull behaviour as a solid wall would impose an approximately correct flow past the rudder. Both the proximity to a hull and air-water interaction might explain the loss of steering force when the ship turned to starboard.

An unconventional proposal is to use the results obtained in this thesis to design a better rudder. The end result may or may not explain why the rudders were formed as they are, or the limitations by this design philosophy that eventually caused the centre-mounted rudder to be adopted.

In this thesis the $k-\epsilon$ turbulence model has been used. This model is sensitive to large adverse pressure gradients and flow separation, both of which happened at large negative angles of attack. Performing the analysis with a different turbulence model could give

more accurate results.

Bibliography

- [Bakker, 2006] Bakker, A. (2006). Lecture 10 - Turbulence Models: Applied Computational Fluid Dynamics. <http://www.bakker.org/dartmouth06/engs150/10-rans.pdf>, accessed 06 May 2015.
- [Bogucki and Crabtree, 2004] Bogucki, P. and Crabtree, P. J. (2004). *Ancient Europe, 8000 B.C. to A.D. 1000: An Encyclopedia of the Barbarian World*. Gale Group, Inc.
- [Edmund, 2012] Edmund, D. O. (2012). A velocity decomposition method for efficient numerical computation of steady external flows. *The University of Michigan*
- [Godal, 2014] Godal, J. B. (2014). Prøvesegling med Saga Oseberg.
- [*Gåten Oseberg*, 2015] [*Gåten Oseberg* (2015)]. Television documentary. Norwegian Broadcasting Corporation, May 2015.
- [Heggem, 2014] Heggem, T. (2014). Simulation of flow around a rudder.
- [Jeong and Hussain, 1995] Jeong, J. and Hussain, F. (1995). On the identification of a vortex. *Journal of Fluid Mechanics*, 285:69–94.
- [Kulturhistorisk museum, 2015] Kulturhistorisk museum, (2015). Kvinnene i Oseberggraven. <http://www.khm.uio.no/besok-oss/vikingskipshuset/utstillinger/oseberg/3-oseberggraven> accessed 28 May 2015.
- [Lockard et al., 2002] Lockard, D. P., Luo, L.-S., Milder, S. D., and Singer, B. A. (2002). Evaluation of powerflow for aerodynamic applications. *Journal of Statistical Physics*, 107(1-2):423–478.
- [Mavriplis and Jameson, 1990] Mavriplis, D. J. and Jameson, A. (1990). Multigrid solution of the navier-stokes equations on triangular meshes. *AIAA journal*, 28(8):pages 1415–1425.
- [Moraes et al., 2013] Moraes, A. D. O. S., da Cunha Lage, P. L., Cunha, G. C., and da Silva, L. F. L. R. (2013). Analysis of the Non-orthogonality Correction of Finite Volume Discretization on Unstructured Meshes.

- [Ong, 2012] Ong, M. C. (2012). Unsteady RANS Simulation of Flow Around a 5:1 Rectangular Cylinder at High Reynolds Numbers *ASME: Ocean Engineering; CFD and VIV*, Vol 5:pages 841–846.
- [OpenFOAM, 2014] OpenFOAM Foundation (2014). Chapter 1 Introduction. <http://cfd.direct/openfoam/user-guide/introduction/x3-20001>, accessed 01 June 2015.
- [OpenFOAM, 2015] OpenFOAM Foundation (2015). OpenFOAM User Guide: 4.4 Numerical schemes. <http://cfd.direct/openfoam/user-guide/fvschemes/>, accessed 05 June 2015.
- [Oseberg ship excavation site] Oseberg ship excavation site. Viking Ship Museum, Oslo, Norway
- [OpenFOAM, 2015] OpenFOAM Foundation (2015). OpenFOAM User Guide: 4.5 Solution and algorithm control <http://cfd.direct/openfoam/user-guide/fvSolution/>, accessed 05 June 2015.
- [Pelletier and Mueller, 2000] Pelletier, A. and Mueller, T. J. (2000). *Low Reynolds number aerodynamics of low-aspect-ratio, thin/flat/cambered-plate wings*. In *Journal of Aircraft*, 37(5) pages 825–832.
- [Pope, 2000] Pope, S. (2014). *Turbulent Flows*. Cambridge University Press.
- [Price et al, 2008] Prince, M., Werenskiold, P. and Tvette, M. R. (2008). *2008 Wolfson Unit Report Number 2065. Towing Tank Tests on Two Hull Variations of the Viking Ship Oseberg*. Marintek/Sintef, December 2008 MT53 F08-294, Osebergskip, S. N.
- [Rodi, 1993] Rodi, W. (1993). *Turbulence Models and Their Application in Hydraulics*. A.A. Balkema Publishers.
- [Sabersky et al., 1998] Sabersky, R. H., Acosta, A. J., Hauptmann, E. G. and Gates, E. M. (1998). *Fluid flow, a first course in fluid mechanics (4th edition)*. Macmillian Publishers.
- [Schlichting, 1979] Schlichting, H. (1979). *Boundary-Layer Theory (7th. edition)*. McGraw-Hill.
- [Spalding, 1961] Spalding, D. B. (1961). A Single Formula for the “Law of the Wall”. In *Journal of Applied Mechanics — Volume 28 — Issue 3*, 28(3) pages 455–459.
- [Steen, 2012] Steen, S. (2012). *TMR4220 Naval Hydrodynamics: Foil Theory*. NTNU-trykk.

- [Sumer and Fredsoe, 2006] Sumer, B. M. and Fredsoe, J. (2006). *Hydrodynamics Around Cylindrical Structures, Advanced Series of Ocean Engineering - Volume 12*. World Scientific Pub Co Inc.
- [Teknisk Ukeblad, 2011] Teknisk Ukeblad (2011). Osebergkopi blir virkelig. <http://www.tu.no/bygg/2011/10/05/osebergkopi-blir-virkelig>, accessed 05 May 2015.
- [Verne, 2009] Verne, J. (2007). *Twenty Thousand Leagues Under the Sea*, trans. Butcher, W. Oxford University Press, original work published in 1870.
- [Versteeg and Malalasekera, 2007] Versteeg, H. and Malalasekera, W. (2007). *An Introduction to Computational Fluid Dynamics: The Finite Volume Method (2nd. edition)*. Prentice Hall.
- [Walderhaug, 1972] Walderhaug, H. (1972). *Ship Hydrodynamics, Basic Course*. Tapir Publishers.
- [White, 1999] White, F. M. (1999). *Fluid Mechanics*. McGraw-Hill Boston.
- [White and Corfield, 1991] White, F. M. and Corfield, I. (1991). *Viscous fluid flow*, volume 3. McGraw-Hill New York.

Appendix 1: Oseberg rudder pressure contours

Pressure contours for $Re=250$

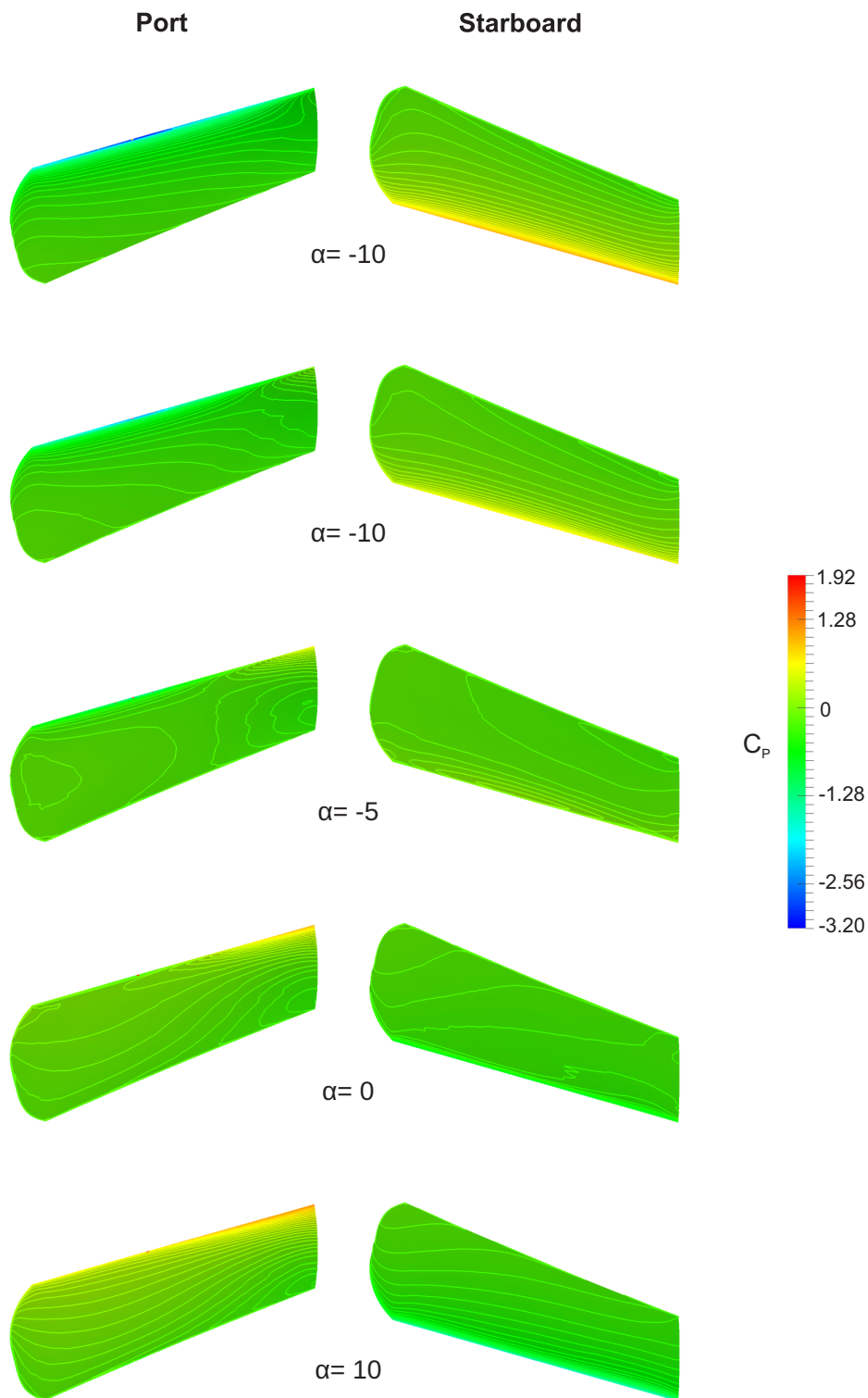


Figure A1.1: Pressure contours on rudder surface for $\beta= 20$.

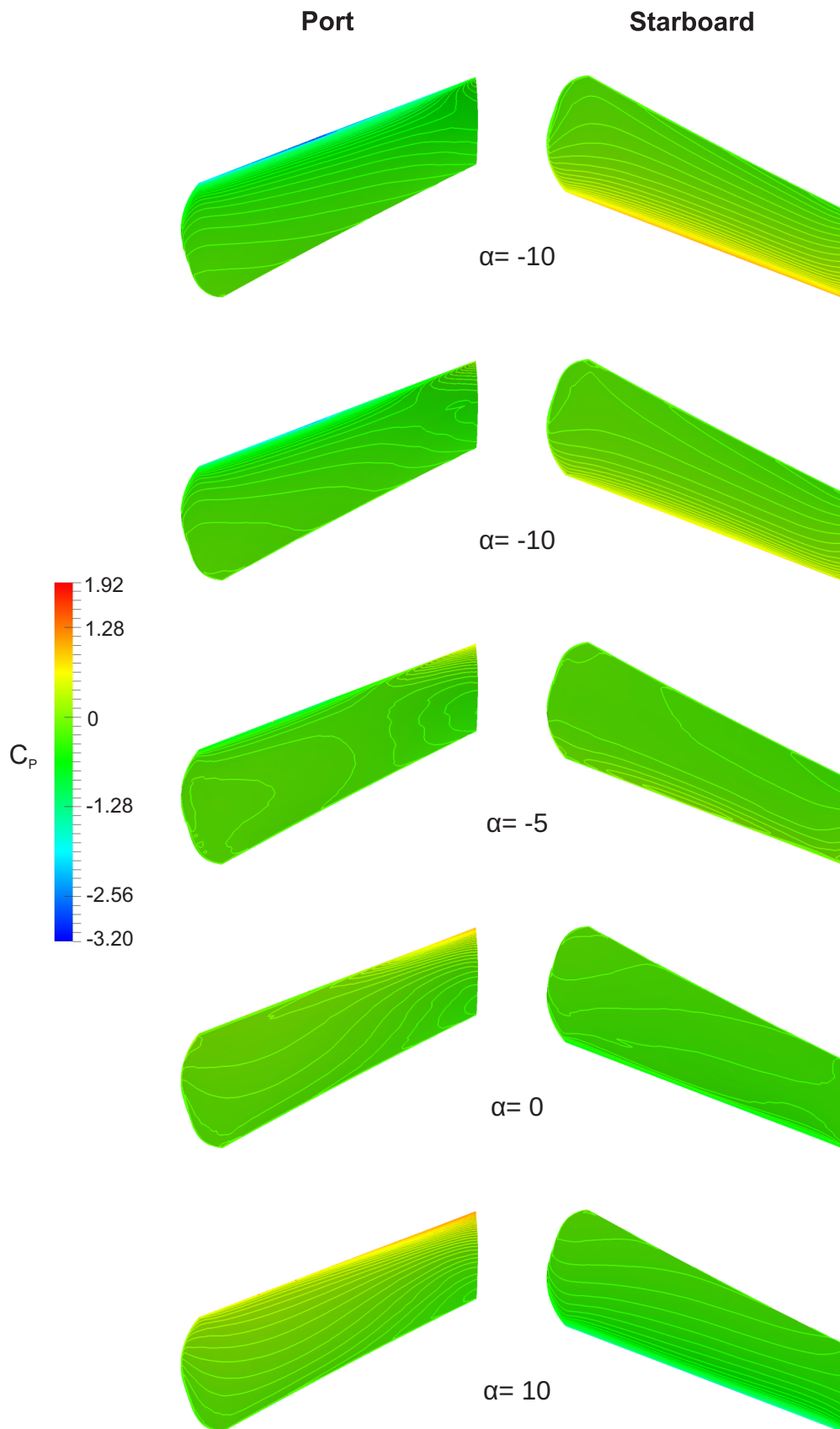


Figure A1.2: Pressure contours on rudder surface for $\beta = 25$.

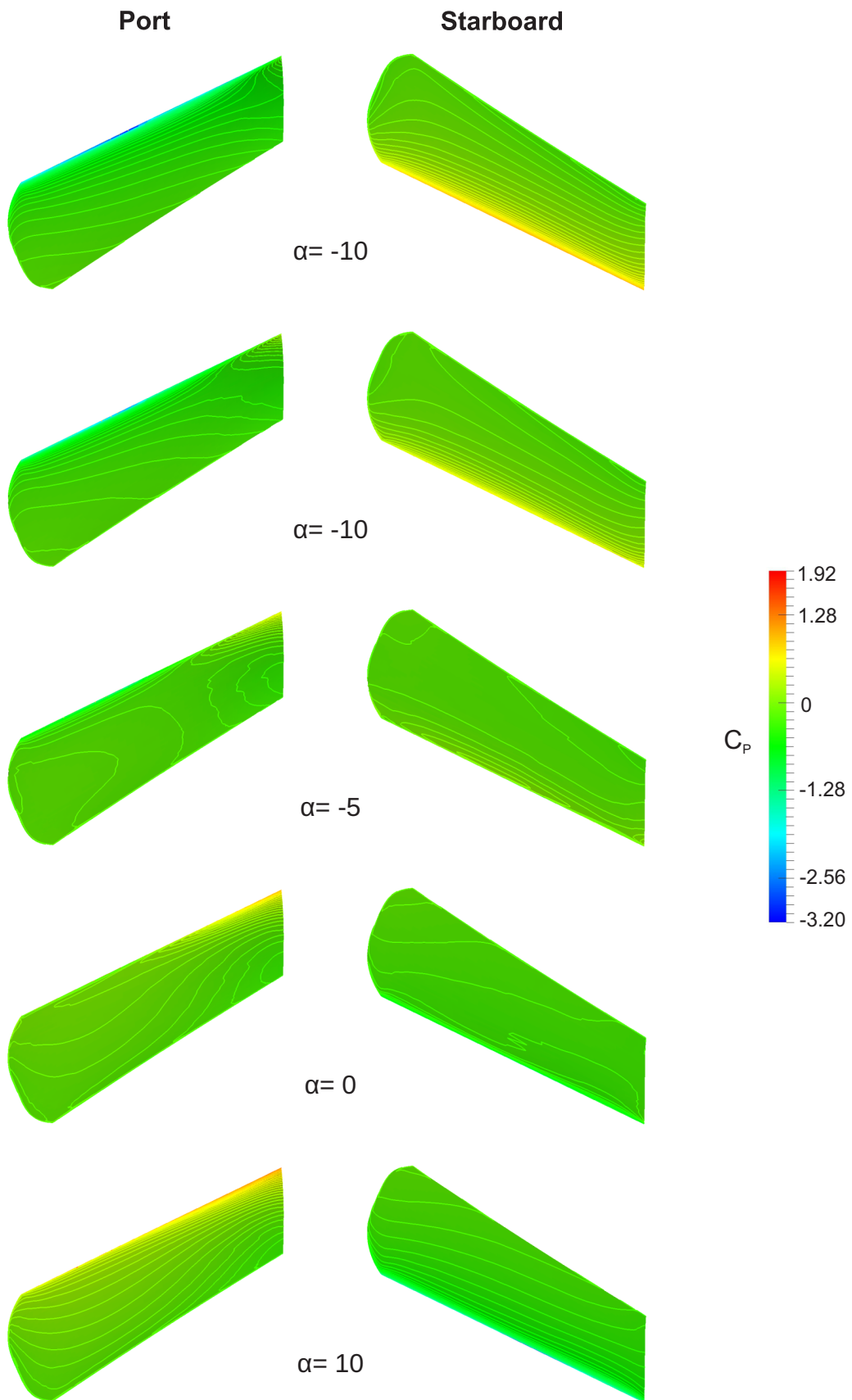


Figure A1.3: Pressure contours on rudder surface for $\beta = 30$.

Pressure contours for $Re=1000$

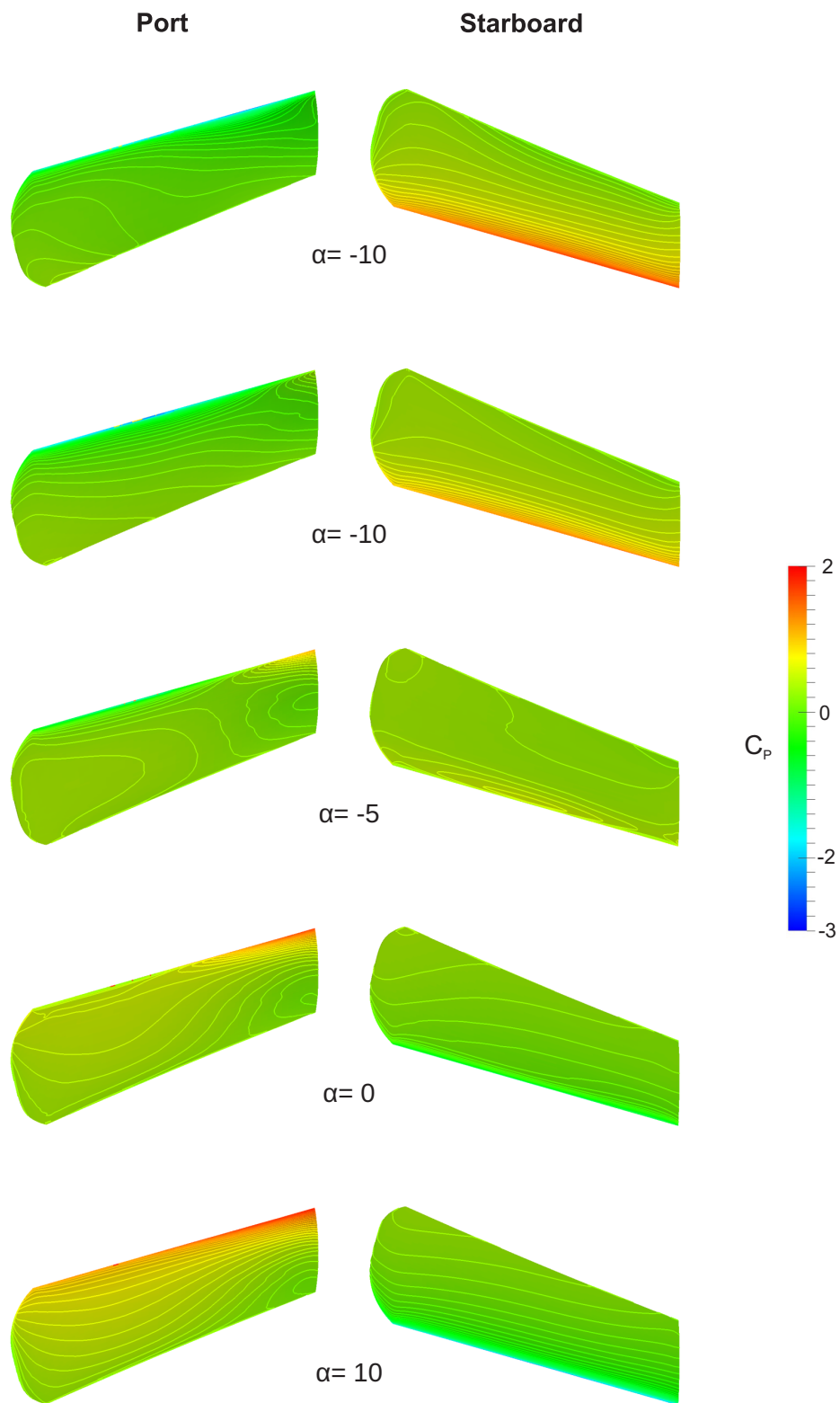


Figure A1.4: Pressure contours on rudder surface for $\beta=20$.

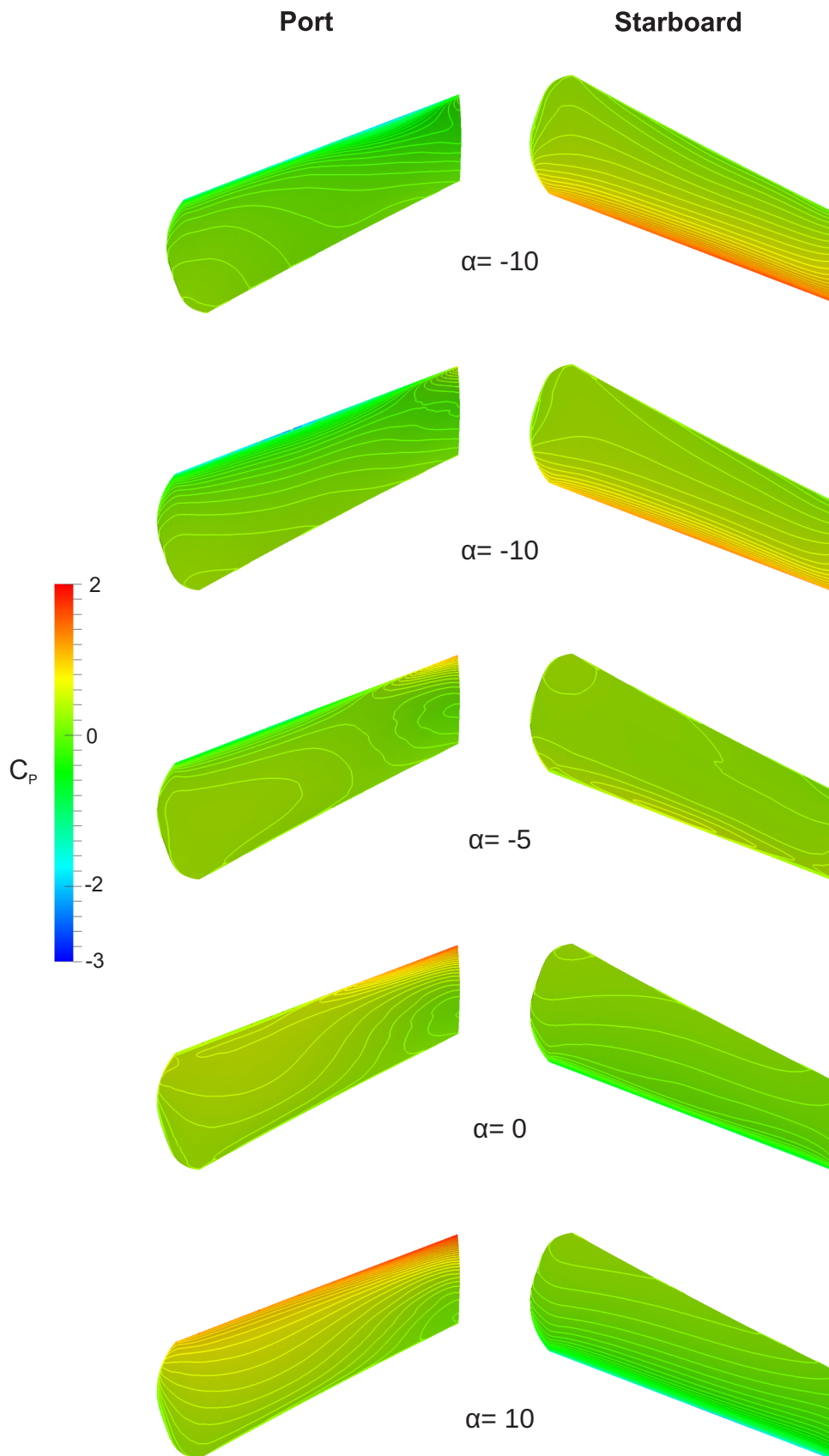


Figure A1.5: Pressure contours on rudder surface for $\beta = 25$.

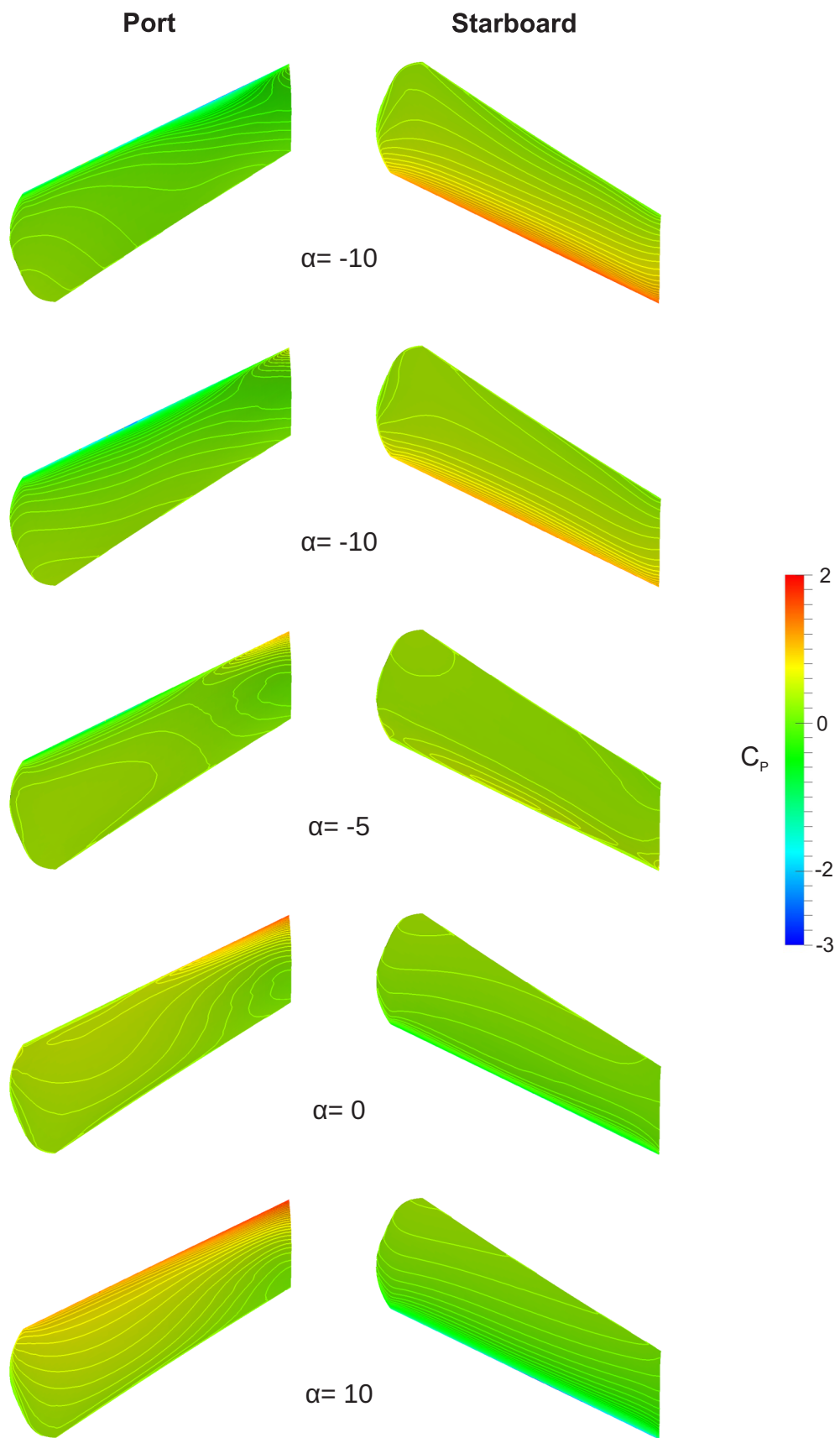


Figure A1.6: Pressure contours on rudder surface for $\beta = 30$.

Pressure contours for $\text{Re}=2.4\times 10^6$

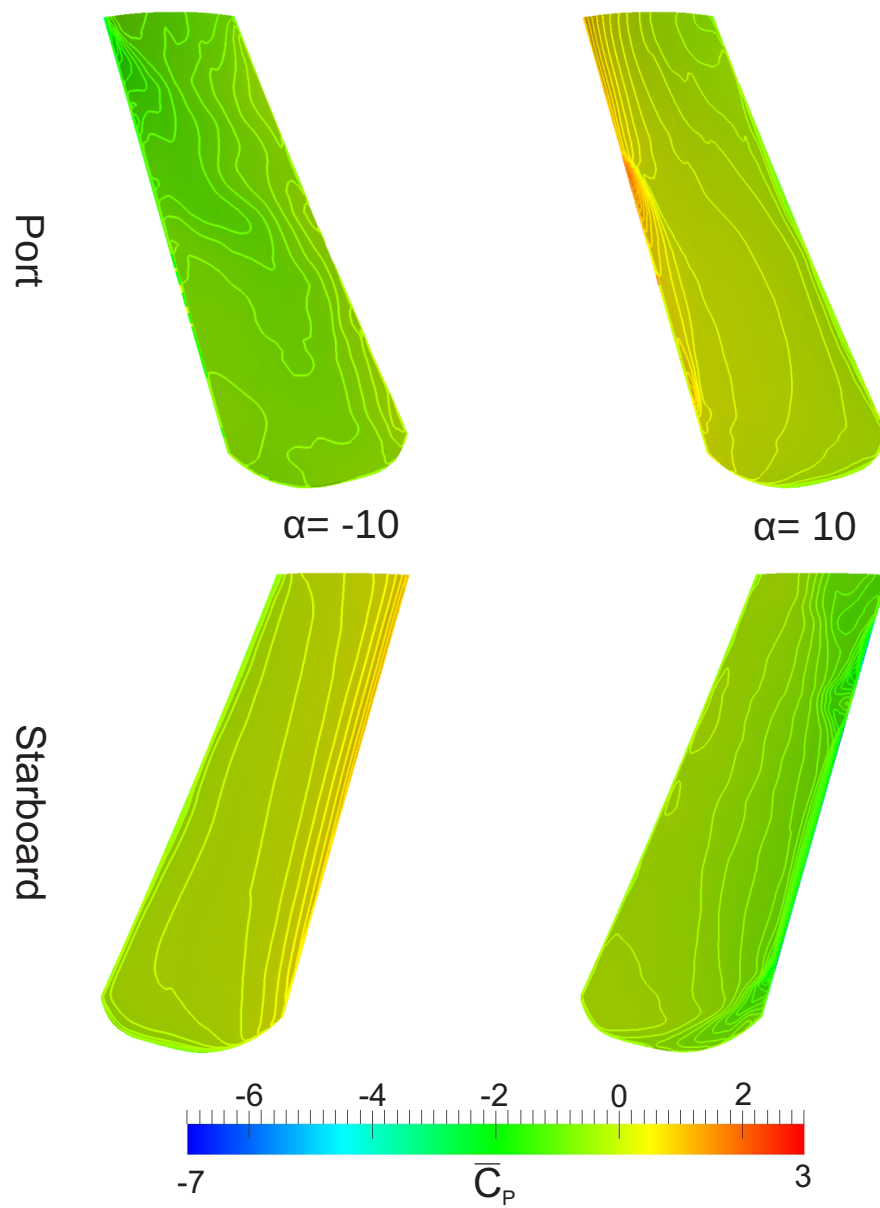


Figure A1.7: Pressure contours on rudder surface for $\beta = 20$.

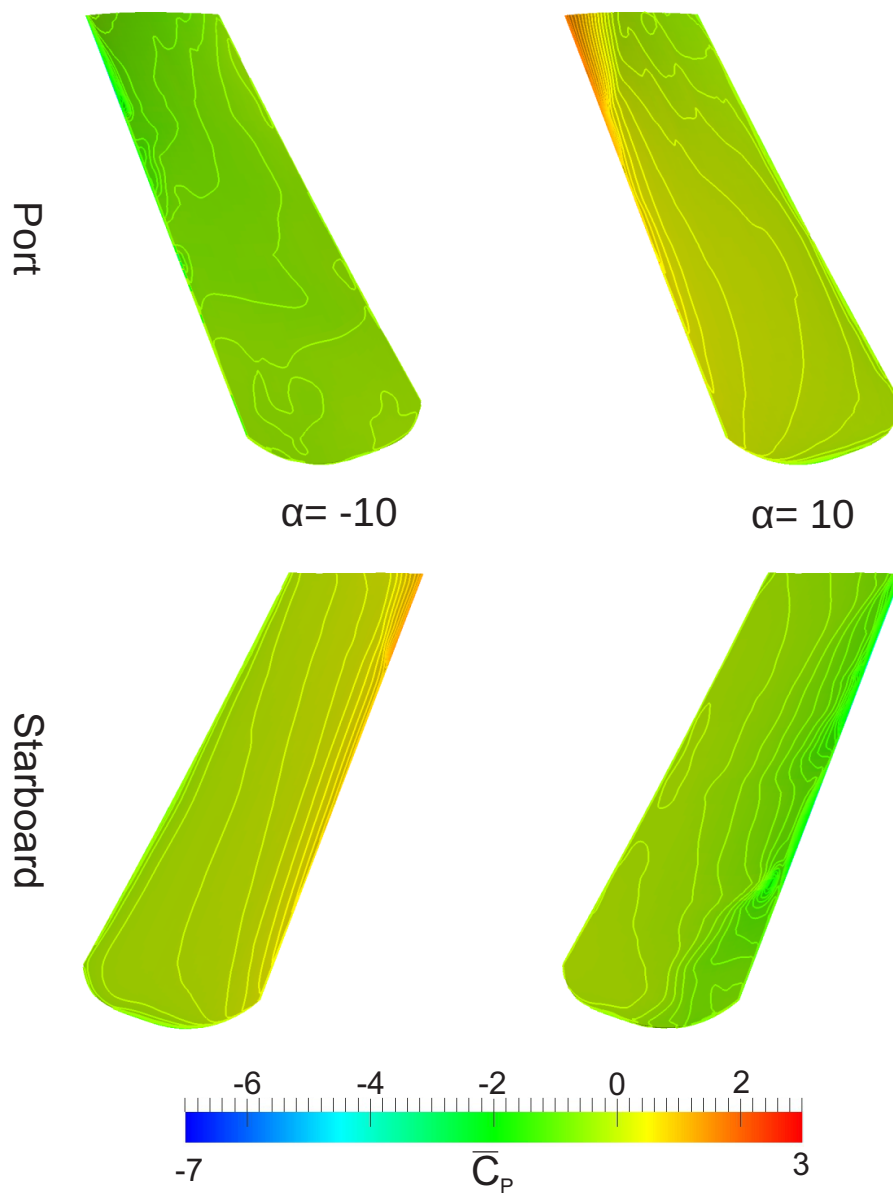


Figure A1.8: Pressure contours on rudder surface for $\beta = 25$.

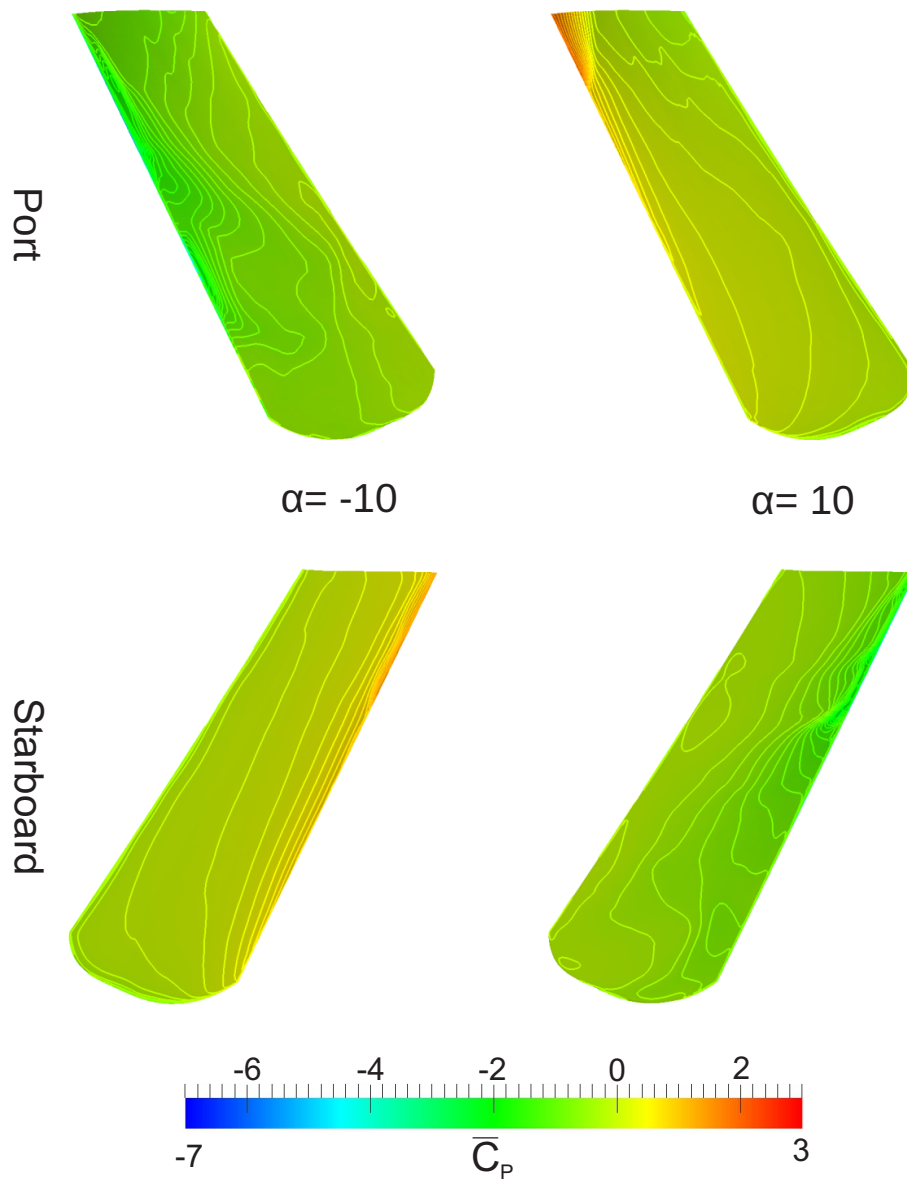


Figure A1.9: Pressure contours on rudder surface for $\beta = 30$.

Appendix 2: Oseberg rudder velocity fields

Velocity field for $Re=250$

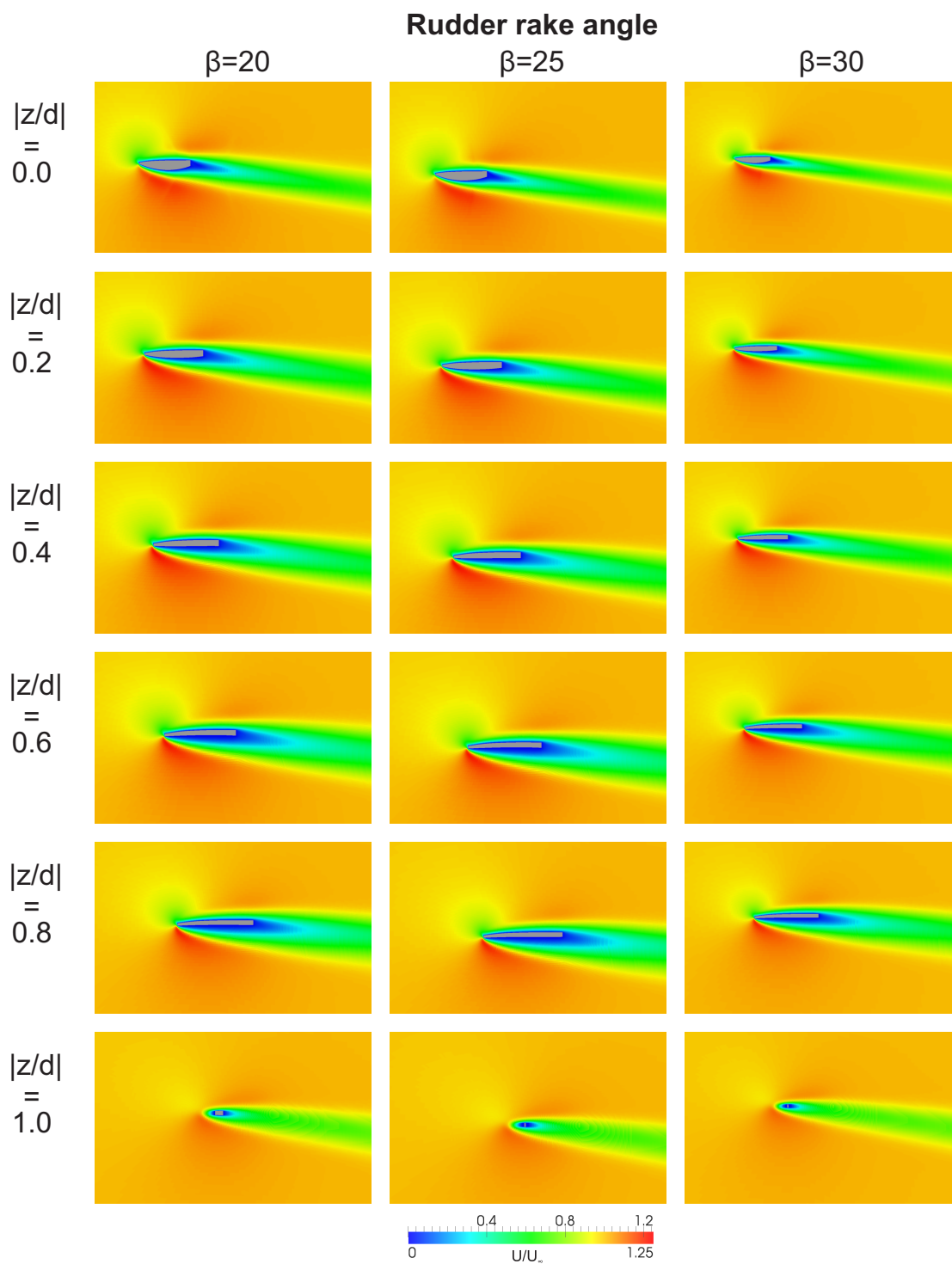


Figure A2.1: Velocity field for angle of attack $\alpha = -10$

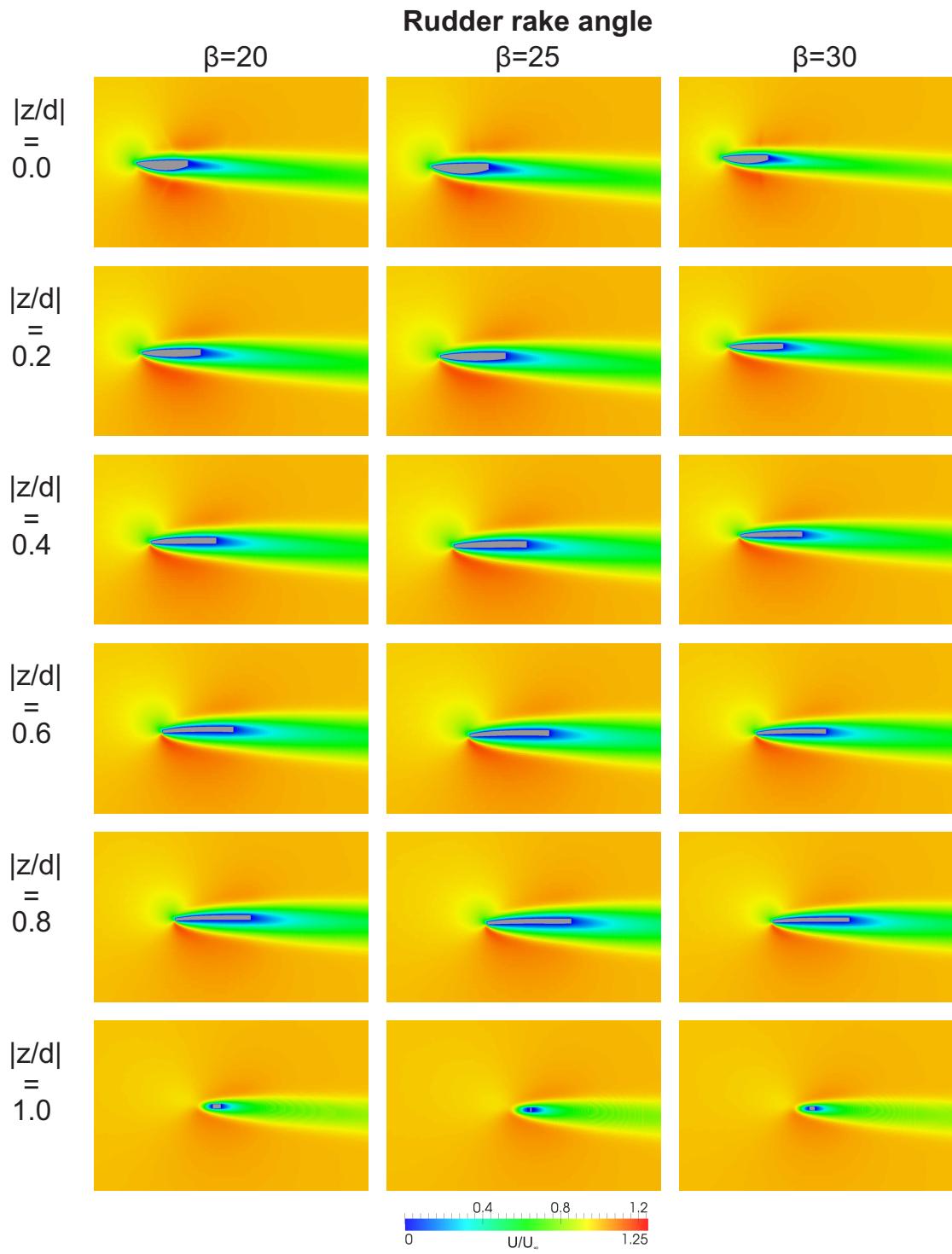


Figure A2.2: Velocity field for angle of attack $\alpha = -5$

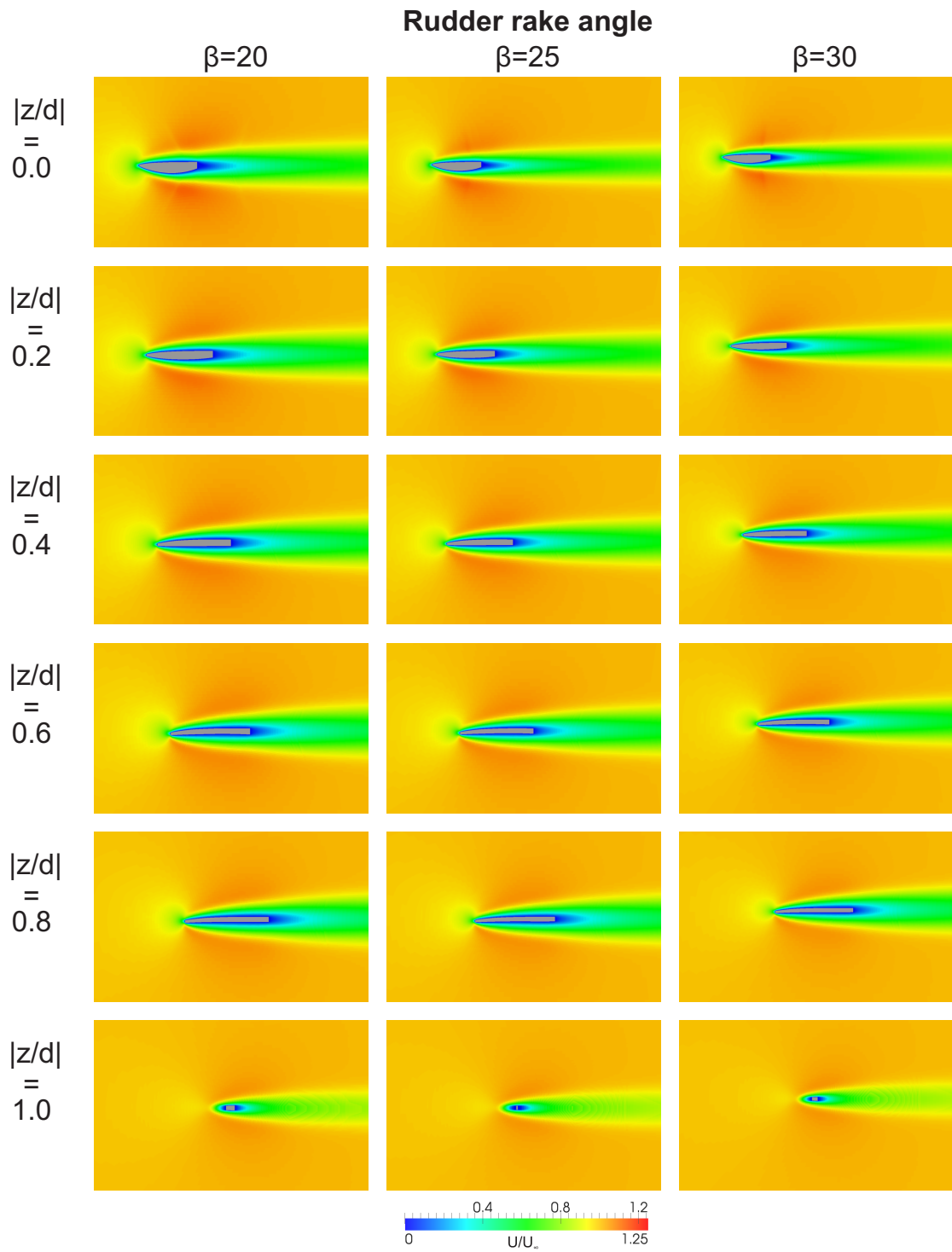


Figure A2.3: Velocity field for angle of attack $\alpha=0$

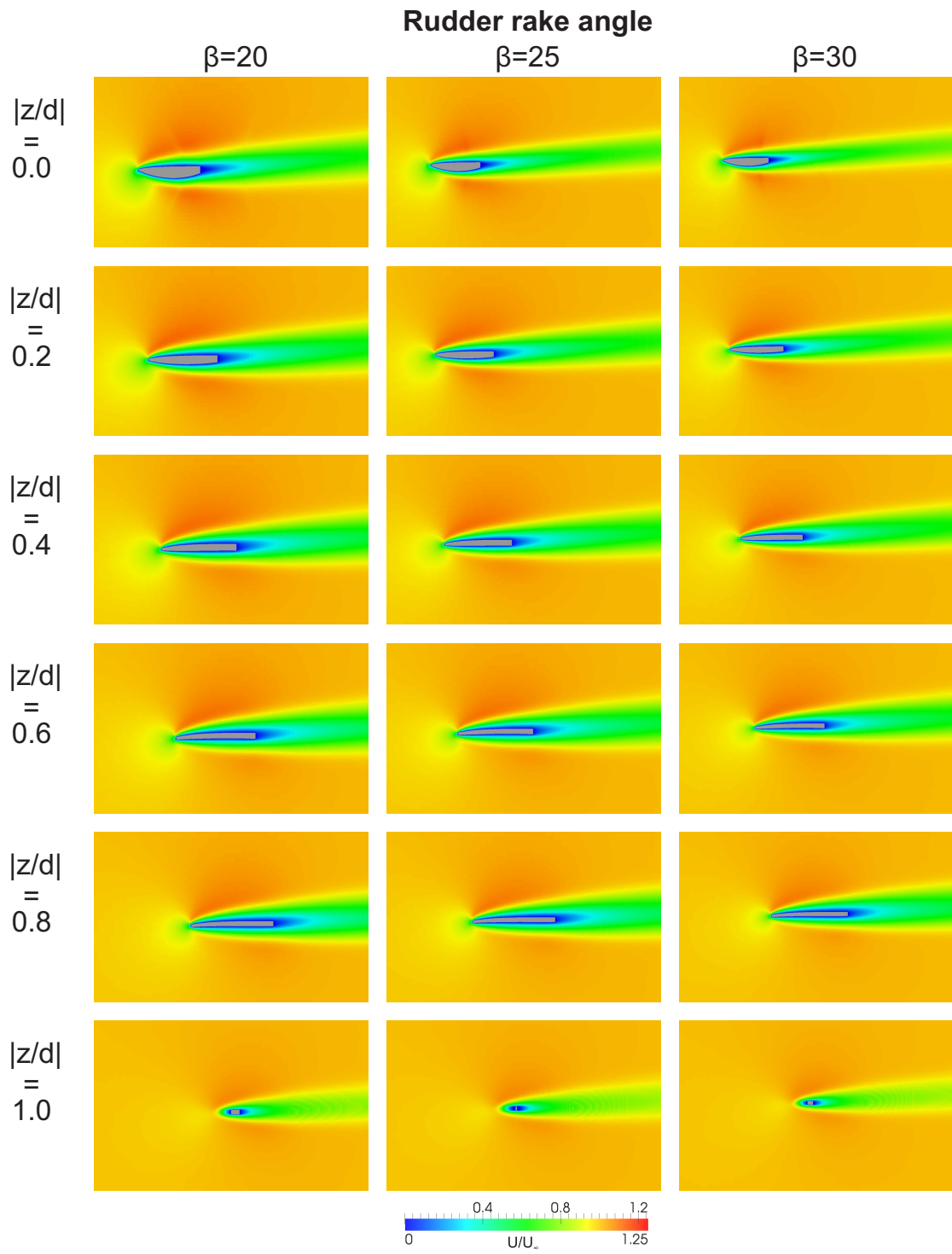


Figure A2.4: Velocity field for angle of attack $\alpha=5$

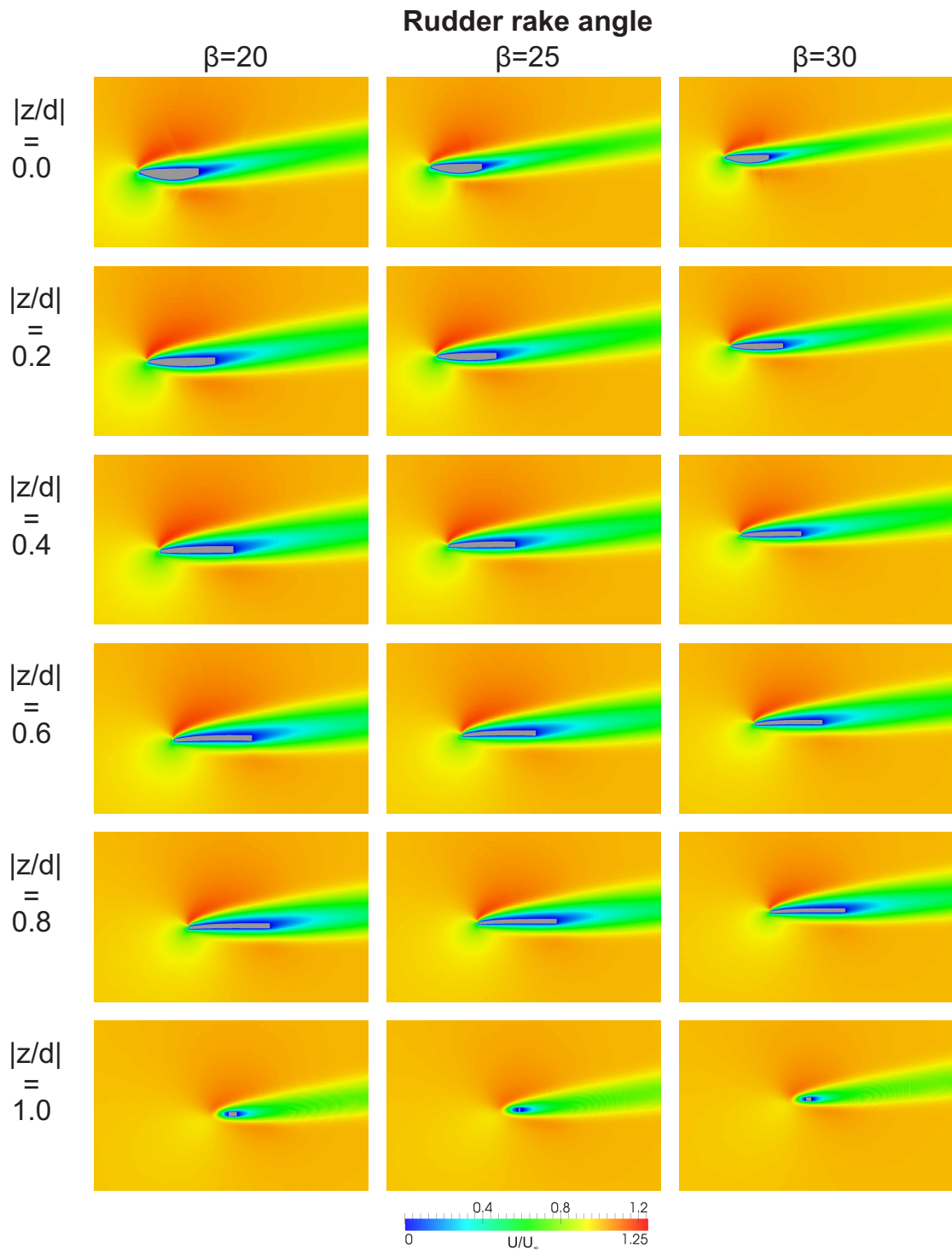


Figure A2.5: Velocity field for angle of attack $\alpha=10$

Velocity field for $Re=1000$

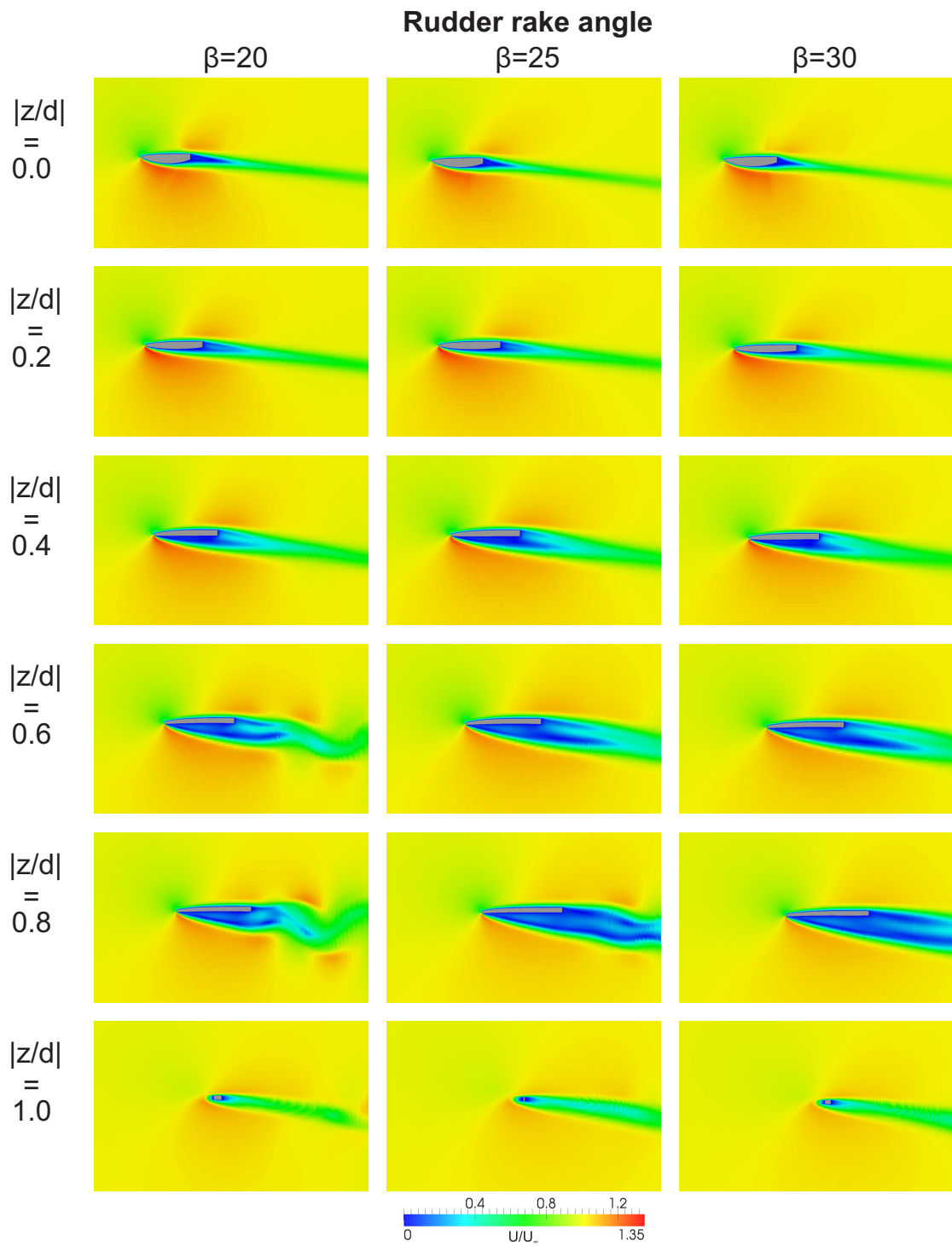


Figure A2.6: Velocity field for angle of attack $\alpha = -10$

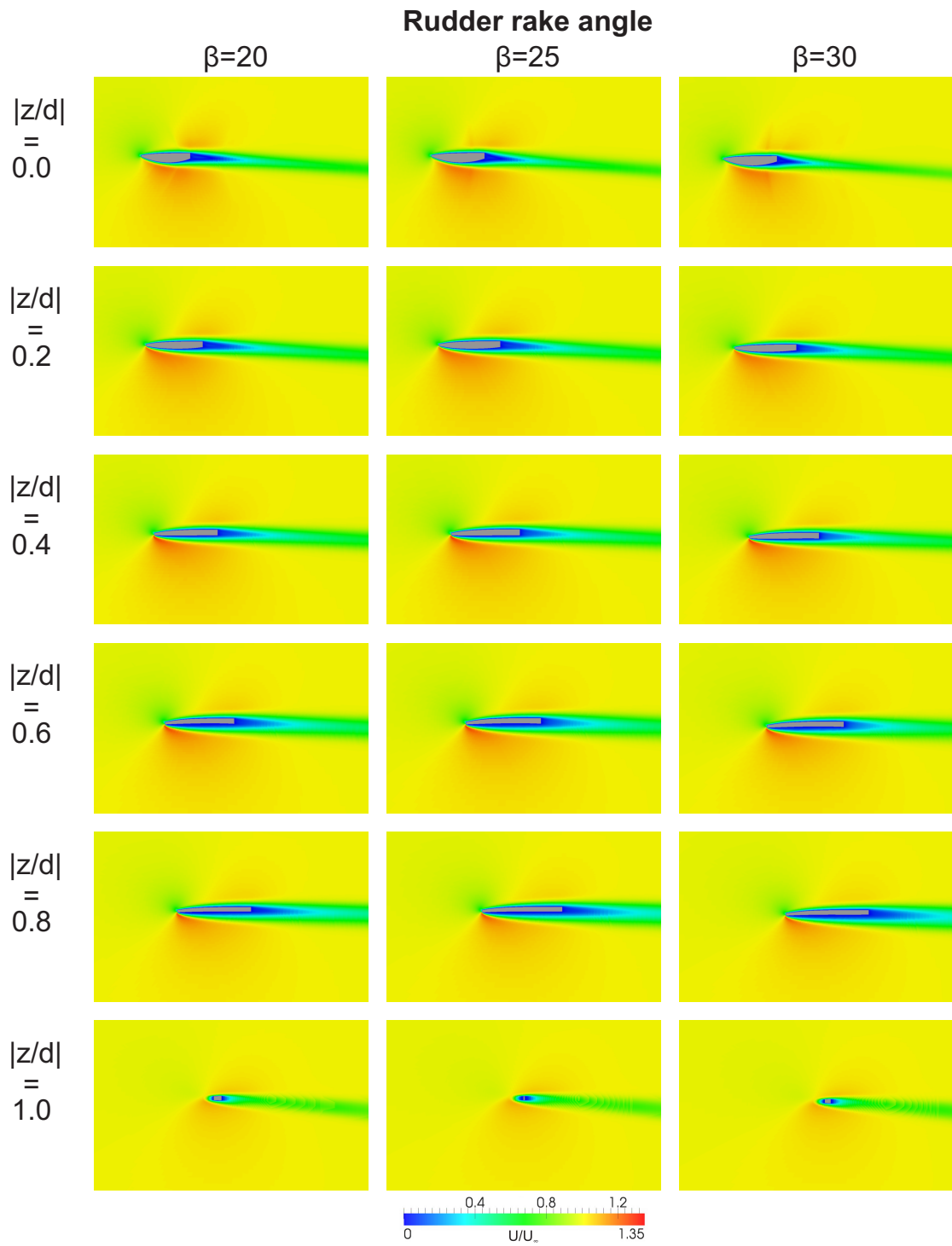


Figure A2.7: Velocity field for angle of attack $\alpha = -5$

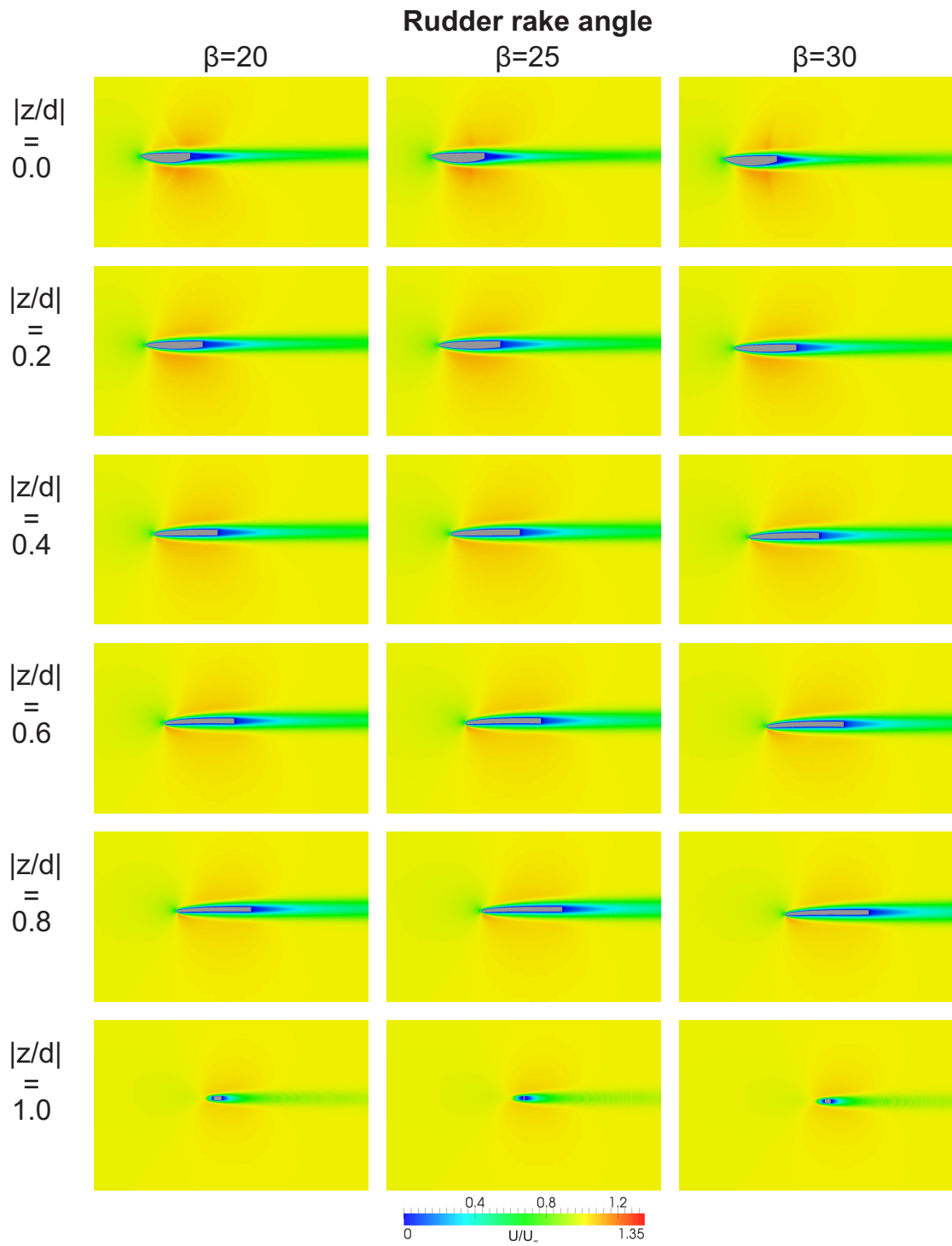


Figure A2.8: Velocity field for angle of attack $\alpha=0$

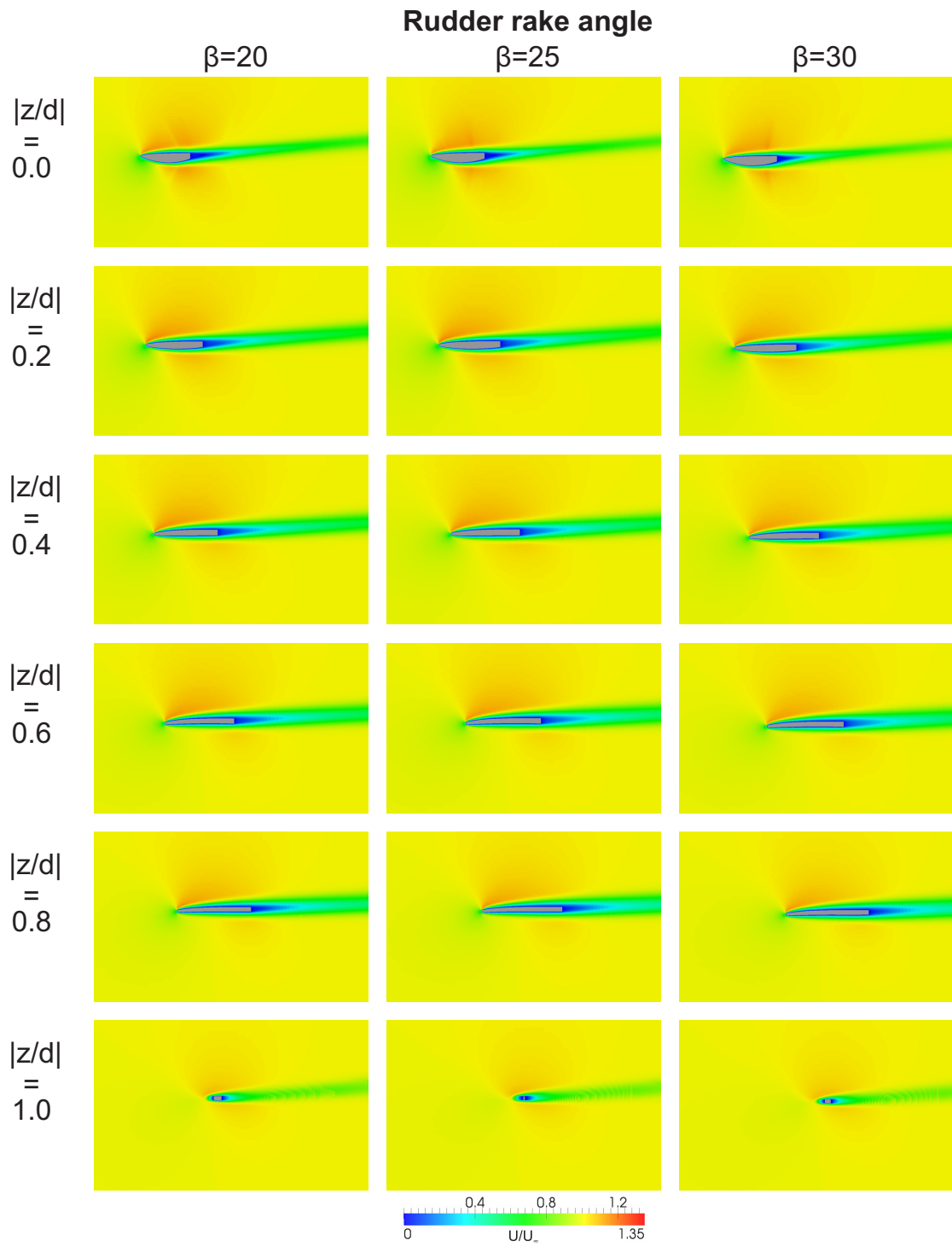


Figure A2.9: Velocity field for angle of attack $\alpha=5$

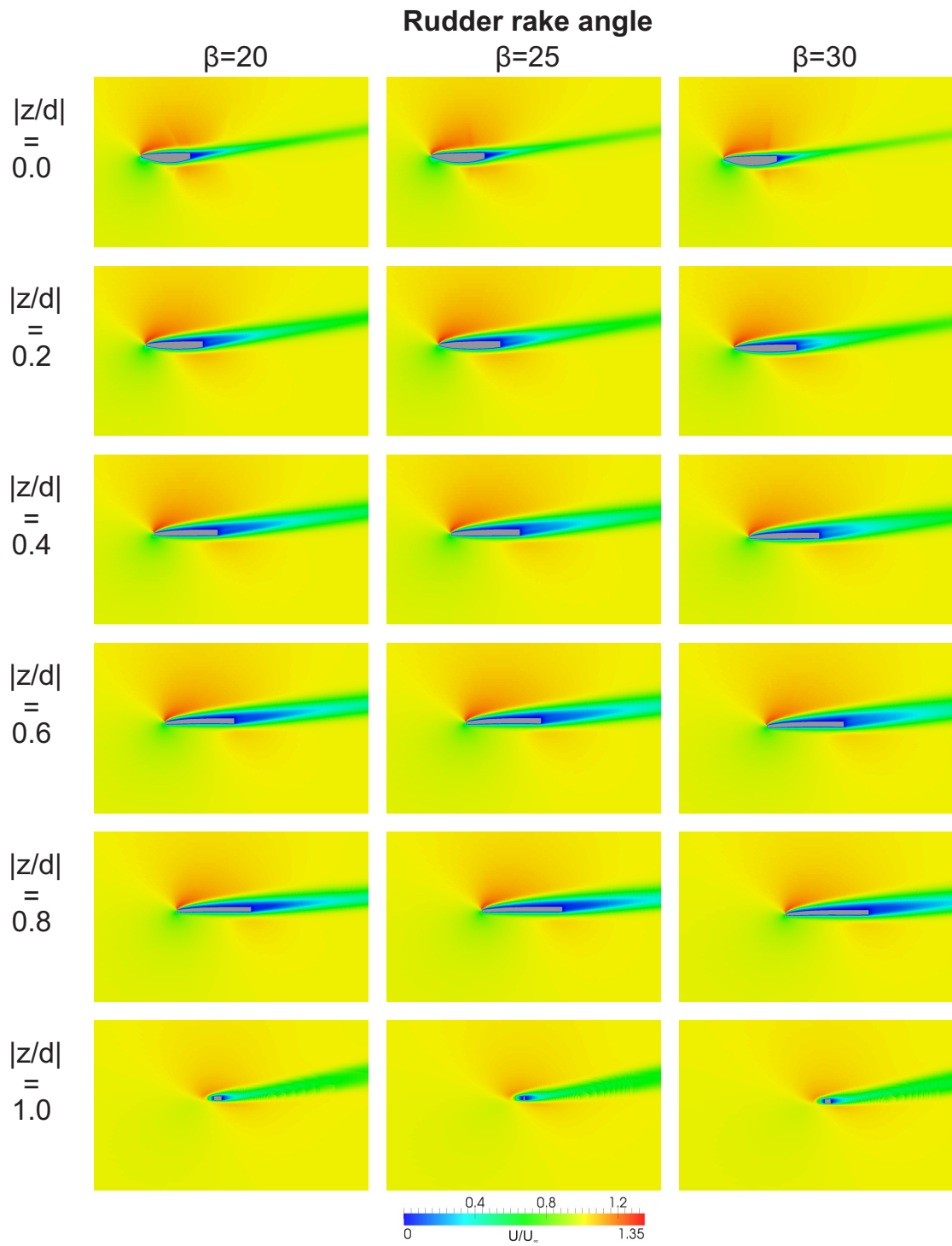


Figure A2.10: Velocity field for angle of attack $\alpha=10$

Velocity field for $Re=2.4 \times 10^6$

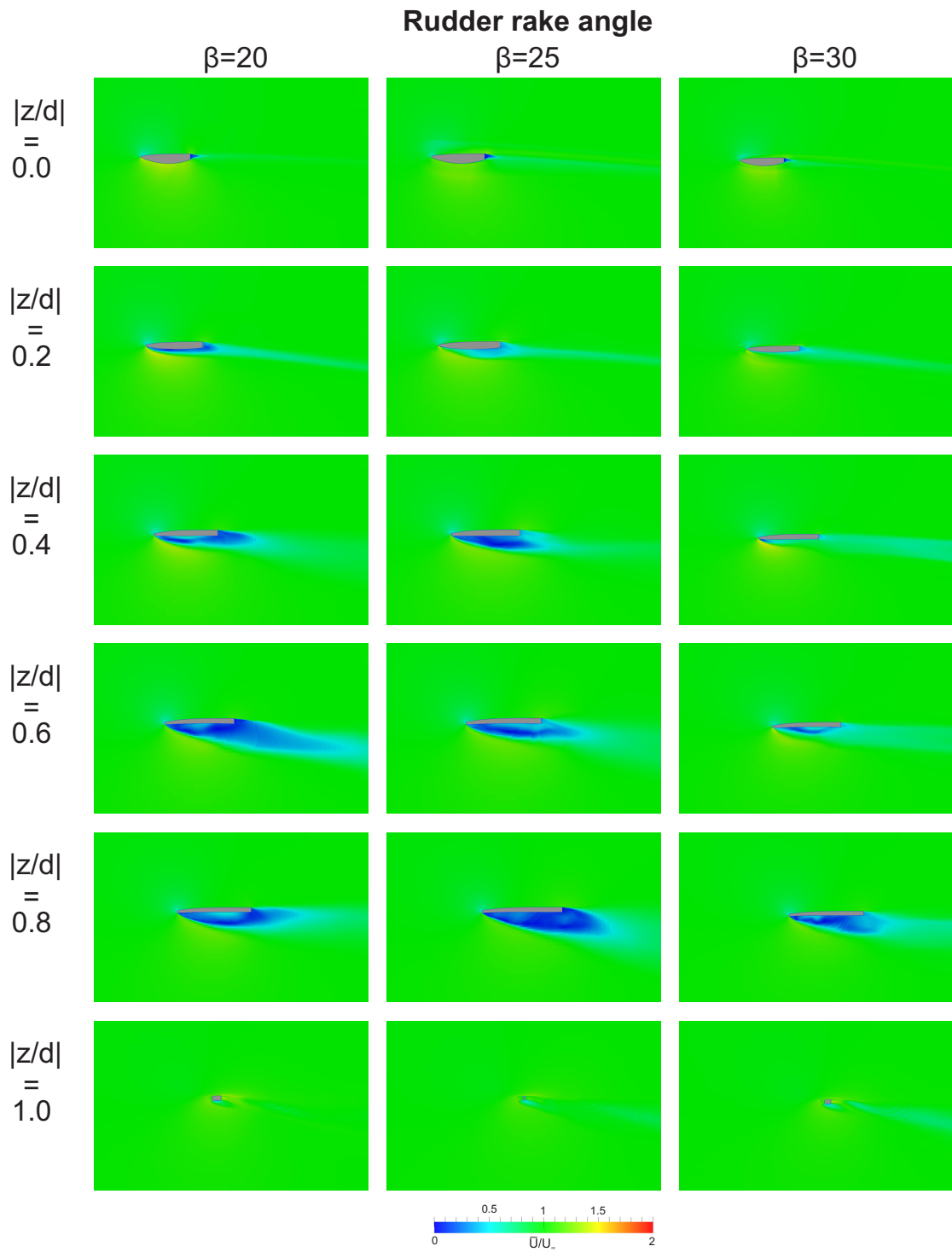


Figure A2.11: Velocity field for angle of attack $\alpha = -10$

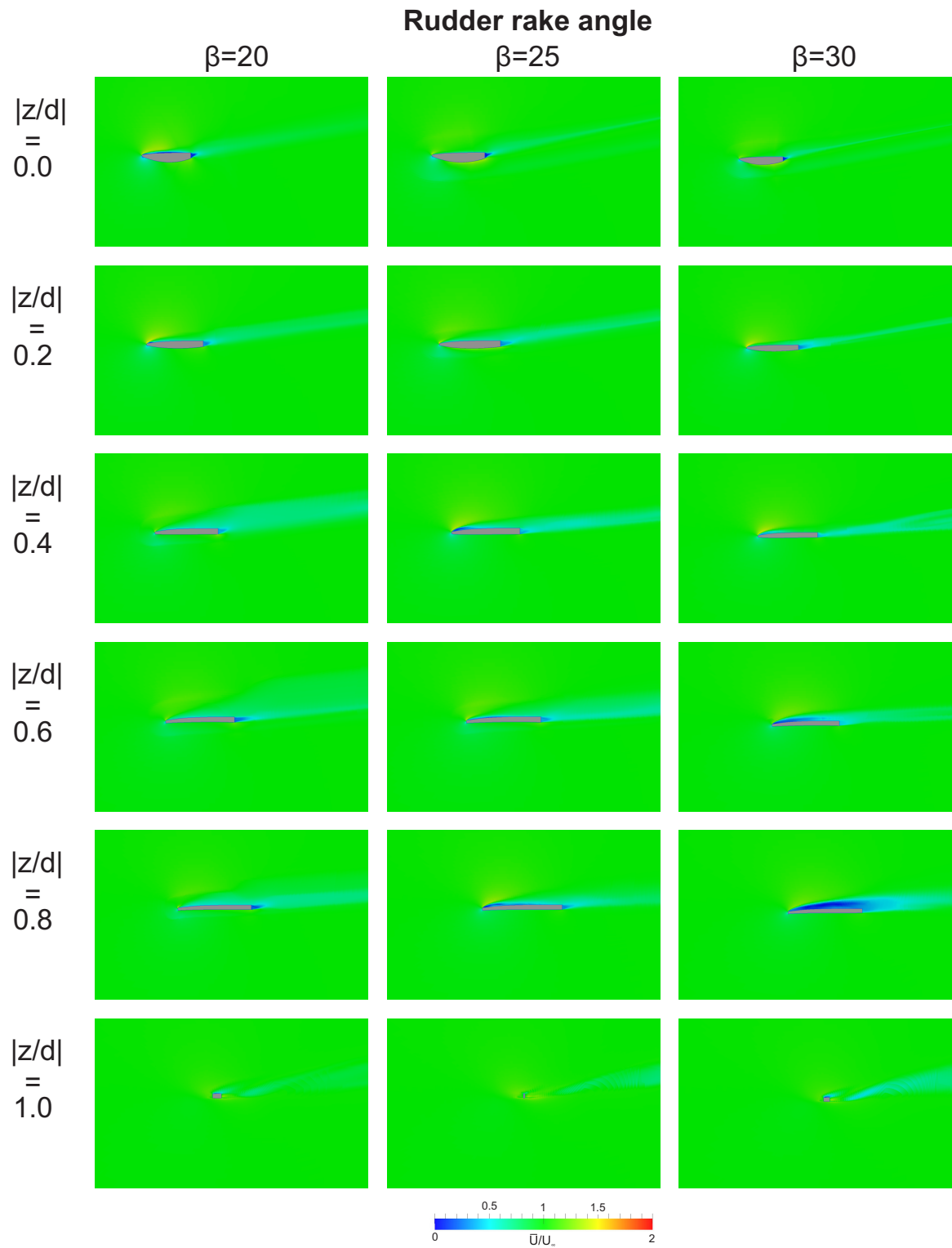


Figure A2.12: Velocity field for angle of attack $\alpha = 10$

Appendix 3: Oseberg rudder turbulent time series

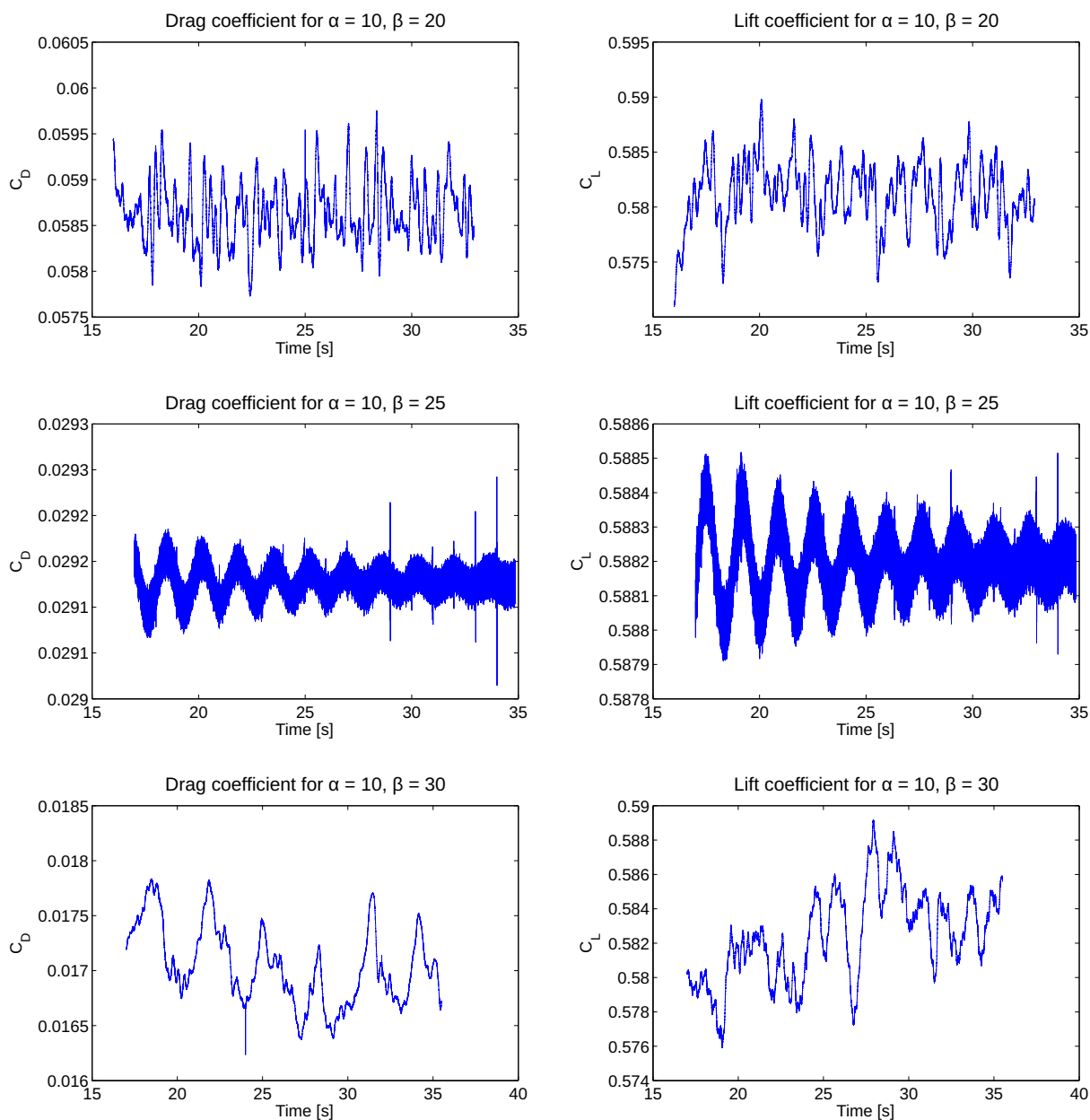


Figure A3.1: Instantaneous values for drag and lift coefficient at $Re=2.4 \times 10^6$ $\alpha=10$

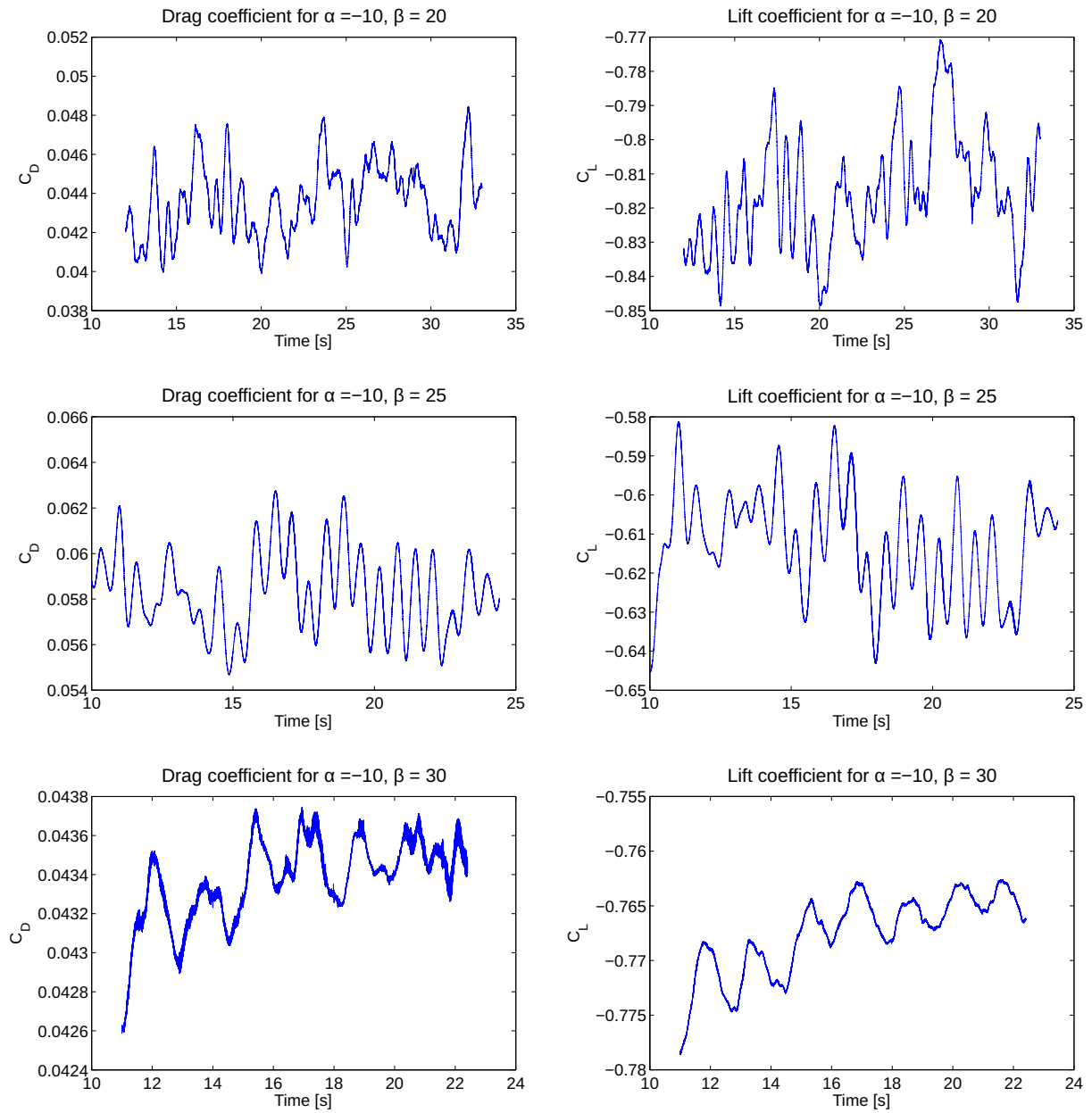


Figure A3.2: Instantaneous values for drag and lift coefficient at $Re=2.4 \times 10^6$ $\alpha=-10$

Appendix 4: Vorticity for $Re=1000$ and $Re=Re=2.4 \times 10^6$

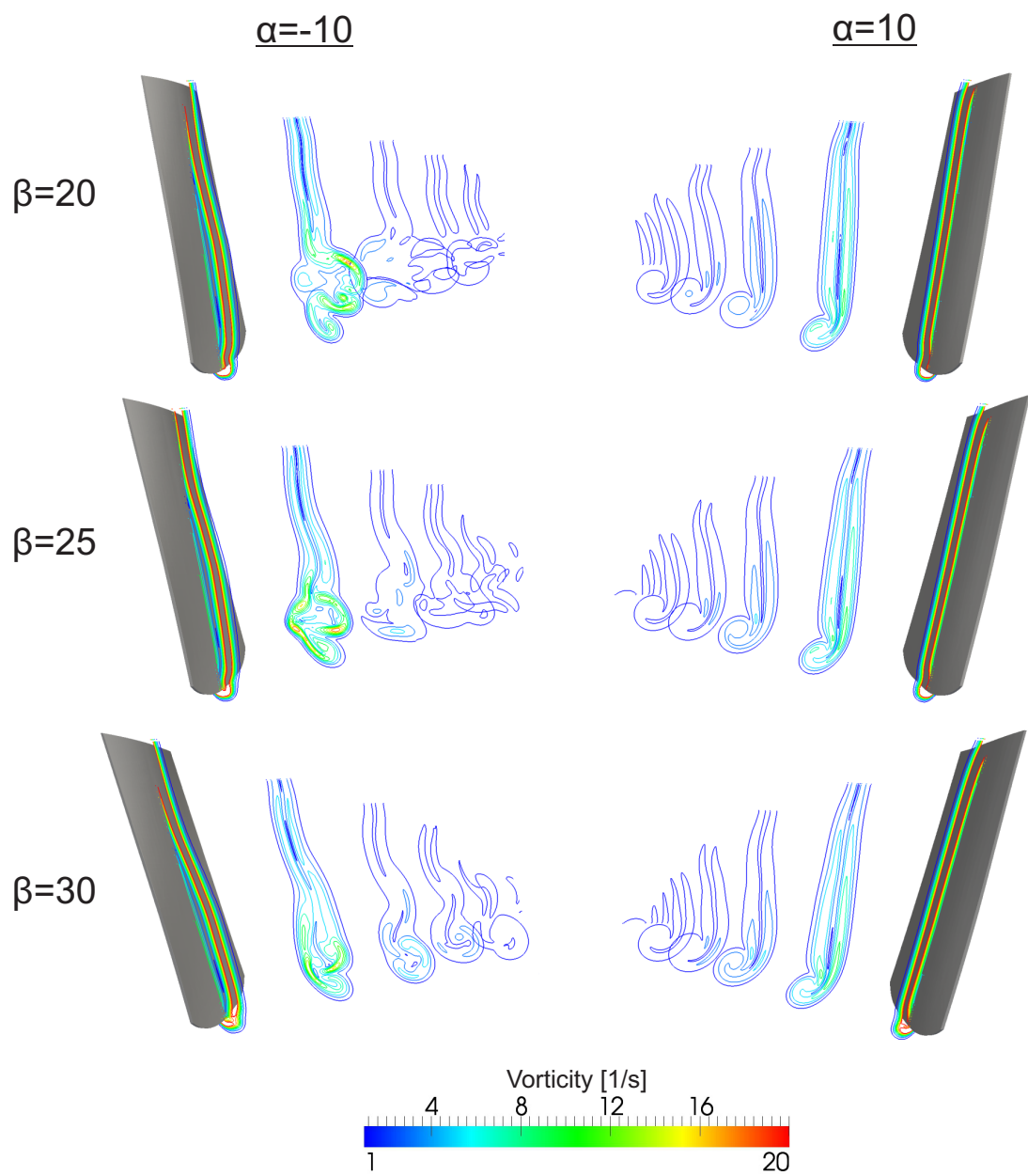


Figure A4.1: Vorticity for $\alpha=\pm 10$ at $Re=1000$ for different rudder rake angles

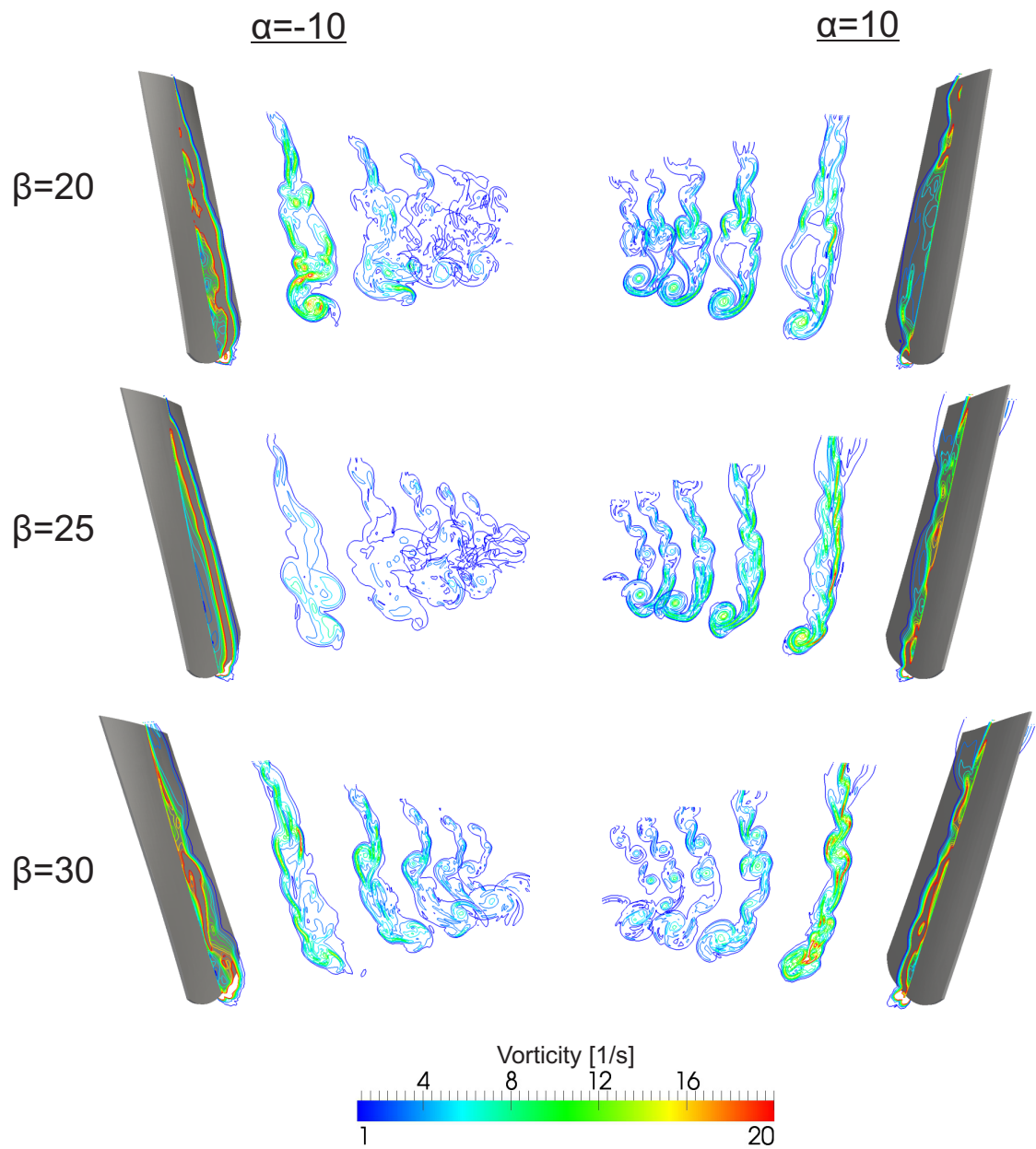


Figure A4.2: Vorticity for $\alpha = \pm 10$ at $Re = 2.4 \times 10^6$ for different rudder rake angles

Appendix 5: OpenFOAM control files

In order of appearance:

Page XXVII: controlDict

Page XXX: fvSchemes

Page XXXI: fvSolution

```

/*-----* C++ *-----*\
|=====|
|  \ \  /  | F i e l d           | OpenFOAM: The Open Source CFD Toolbox
|  \ \  /  | O p e r a t i o n   | Version: 2.2.0
|  \ \  /  | A n d                | Web:      www.OpenFOAM.org
|  \ \  /  | M a n i p u l a t i o n |
\*-----*\
FoamFile
{
    version      2.0;
    format       ascii;
    class        dictionary;
    location     "system";
    object       controlDict;
}
// *****

application    pimpleFoam;

startFrom      startTime;

startTime      24;

stopAt         endTime;

endTime        48;

deltaT         0.00005;

writeControl   adjustableRunTime;

writeInterval  10;

purgeWrite     0;

writeFormat    ascii;

writePrecision 6;

writeCompression off;

timeFormat     general;

timePrecision  6;

runTimeModifiable no;

adjustTimeStep yes;

maxCo         0.7;

functions
{
    forceCoeffs
    {
        type          forceCoeffs;
        functionObjectLibs ( "libforces.so" );
        outputControl  timeStep;
        outputInterval 1;
        patches (Rudder);
        pName         p;
        UName         U;
        rhoName       rhoInf;
        rhoInf        1025;
        magUInf       1;
        log            true;
        liftDir       (0 1 0);
        dragDir       (1 0 0);
        CofR          (-0.303 0.135 8.02);
    }
}

```

```

        pitchAxis      (0 0 1);
        lRef           1;
        Aref           1.11597;
    }
forces
{
    type                forces;
    functionObjectLibs  ("libforces.so");
    outputControl        timeStep;
    outputInterval       1;
    patches              (Rudder);
    pName                p;
    UName                U;
    rhoName              rhoInf;
    log                  true;
    CofR                 (-0.303 0.135 8.02);
    rhoInf               1025;
}

fieldAverage1
{
    type fieldAverage;
    functionObjectLibs ("libfieldFunctionObjects.so");
    enabled true;
    outputControl outputTime;
    fields
    (
        U
        {
            mean on;
            prime2Mean on;
            base time;
        }

        p
        {
            mean on;
            prime2Mean on;
            base time;
        }
    );
}

};

// ***** //

```

```

/*-----* C++ -*-----*/
|=====|
| \ \ \ \ | F i e l d |   OpenFOAM: The Open Source CFD Toolbox
| \ \ \ \ | O p e r a t i o n |   Version: 2.3.0
| \ \ \ \ | A n d |   Web: www.OpenFOAM.org
| \ \ \ \ | M a n i p u l a t i o n |
|-----|
/*-----*/
FoamFile
{
    version      2.0;
    format       ascii;
    class        dictionary;
    location     "system";
    object       fvSchemes;
}
// *****

ddtSchemes
{
    default      backward;
}

gradSchemes
{
    default      Gauss linear;
}

divSchemes
{
    default      none;
    div(phi,U)   Gauss limitedLinearV 1;
    div(phi,k)   bounded Gauss upwind 1;
    div(phi,epsilon) bounded Gauss upwind 1;
    div(phi,R)   Gauss limitedLinear 1;
    div(R)       Gauss linear;
    div(phi,nuTilda) Gauss limitedLinear 1;
    div((nuEff*dev(T(grad(U)))) Gauss linear;
}

laplacianSchemes
{
    default      Gauss linear limited 0.333;
}

interpolationSchemes
{
    default      linear;
}

snGradSchemes
{
    default      limited 0.333;
}

fluxRequired
{
    default      no;
    p            ;
}

// *****

```

```

/*-----* C++ -*-----*/
|=====|
| \ \ \ \ | F i e l d |   OpenFOAM: The Open Source CFD Toolbox
| \ \ \ \ | O p e r a t i o n |   Version: 2.3.0
| \ \ \ \ | A n d |   Web: www.OpenFOAM.org
| \ \ \ \ | M a n i p u l a t i o n |
|-----*-----*/
FoamFile
{
    version      2.0;
    format       ascii;
    class        dictionary;
    location     "system";
    object       fvSolution;
}
// *****

solvers
{
    p
    {
        solver          GAMG;
        tolerance       1e-06;
        relTol          0.05;
        smoother        GaussSeidel;
        nPreSweeps      0;
        nPostSweeps     2;
        cacheAgglomeration on;
        agglomerator    faceAreaPair;
        nCellsInCoarsestLevel 10;
        mergeLevels     1;
    }

    pFinal
    {
        $p;
        tolerance       1e-06;
        relTol          0;
    };
    /* p
    {
        solver          PCG;
        preconditioner  DIC;
        tolerance       1e-06;
        relTol          0.01;
    }

    pFinal
    {
        solver          PCG;
        preconditioner  DIC;
        tolerance       1e-06;
        relTol          0;
    }*/

    "(U|k|epsilon)"
    {
        solver          PBiCG;
        preconditioner  DILU;
        tolerance       1e-05;
        relTol          0;
    }

    "(U|k|epsilon)Final"
    {
        $U;
        tolerance       1e-05;
        relTol          0;
    }
}

```

```

}

R
{
    solver          PBiCG;
    preconditioner  DILU;
    tolerance       1e-05;
    relTol          0;
}

nuTilda
{
    solver          PBiCG;
    preconditioner  DILU;
    tolerance       1e-05;
    relTol          0;
}
}

PIMPLE
{
    nOuterCorrectors 1;
    nCorrectors       2;
    nNonOrthogonalCorrectors 3;
    pRefCell          0;
    pRefValue         0;
}

// ***** //

```